ISSN: 2161-4717 Volume 8, Number 4, December 2018

Scientific Research Publishing

International Journal of Astronomy and Astrophysics

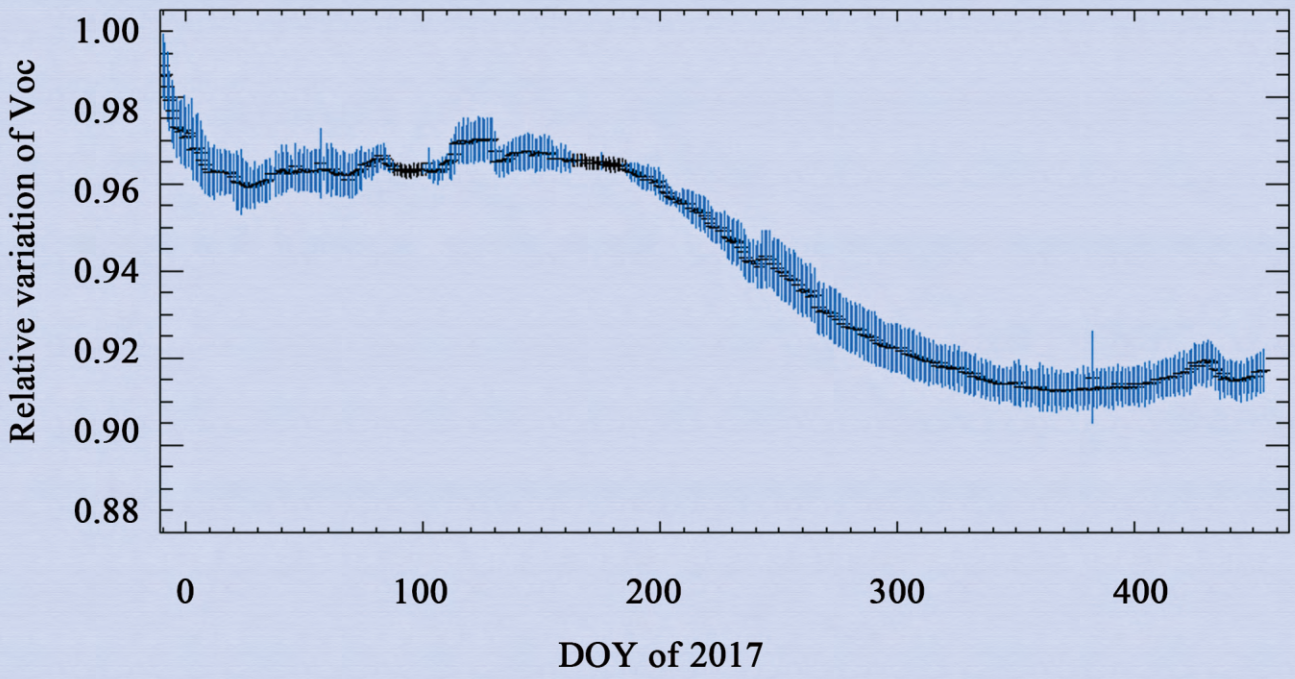

ISSN: 2161-4717
9 772161 471005 04

www.scirp.org/journal/ijaa

Journal Editorial Board

ISSN 2161-4717 (Print) ISSN 2161-4725 (Online)
http://www.scirp.org/journal/ijaa

Editor-in-Chief

Editorial Board

Scientific Research Publishing

International Journal of Astronomy and Astrophysics, 2018, 8, 299-424
http://www.scirp.org/journal/ijaa
ISSN Online: 2161-4725
ISSN Print: 2161-4717

Table of Contents

Volume 8 Number 4 December 2018

The figure on the front cover is from the article published in International Journal of Astronomy and Astrophysics, 2018, Vol. 8, No. 4, pp. 306-322 by Honoka Toda, *et al.*

International Journal of Astronomy and Astrophysics (IJAA)
Journal Information

SUBSCRIPTIONS

The *International Journal of Astronomy and Astrophysics* (Online at Scientific Research Publishing, www.SciRP.org) is published quarterly by Scientific Research Publishing, Inc., USA.

Subscription rates:
Print: $79 per issue.
To subscribe, please contact Journals Subscriptions Department, E-mail: sub@scirp.org

SERVICES

Advertisements
Advertisement Sales Department, E-mail: service@scirp.org

Reprints (minimum quantity 100 copies)
Reprints Co-ordinator, Scientific Research Publishing, Inc., USA.
E-mail: sub@scirp.org

COPYRIGHT

PRODUCTION INFORMATION

For manuscripts that have been accepted for publication, please contact:
E-mail: ijaa@scirp.org

International Journal of Astronomy and Astrophysics, 2018, 8, 299-305
http://www.scirp.org/journal/ijaa
ISSN Online: 2161-4725
ISSN Print: 2161-4717

New Find of Six-Spoke Sun Wheels from the Bronze Age in Scandinavia

Nils-Axel Mörner[1*], Bob G. Lind[2]

[1]Paleogeophysics & Geodynamics, Stockholm, Sweden
[2]Archaeoastronomy, Malmö, Sweden
Email: *morner@pog.nu

How to cite this paper: Mörner, N.-A. and Lind, B.G. (2018) New Find of Six-Spoke Sun Wheels from the Bronze Age in Scandinavia. *International Journal of Astronomy and Astrophysics*, **8**, 299-305.
https://doi.org/10.4236/ijaa.2018.84021

Received: October 6, 2018
Accepted: November 4, 2018
Published: November 7, 2018

Abstract

Six-spoke Sun wheels have previously been described by us from Mesopotamia, rock-carvings in Sweden and a golden sky dome from Sweden. The division of the Sun wheel into six segments refers to the six double-months of 60 days, and a full annual cycle of 360 days. In this paper we report the findings of a stone carving with 9 six-spoke Sun wheels and two solar eclipses found and depicted in 1840 in Denmark. The spokes in the nine Sun wheels are in N-S, E-W and NW-SE direction. The NW-SE line co-insides with the sunset at summer solstice and sunrise at winter solstice, which is in full agreement with the alignment of the famous stone-ship of Ales Stones in southernmost Sweden. The new stone carving in Denmark provides a confirmation of the deep knowledge in astronomy existing among the Bronze Age people, all from Mesopotamia up the Scandinavia.

Keywords

Sun Wheel, Stone Carving, Archaeoastronomy, Ales Stones, Scandinavia

1. Introduction

We have published a number of papers on astronomical monuments and object from the Bronze Age in Sweden [1]-[11], out of those papers the last two [10] and [11] referred to the six-spoke Sun wheel found on "the Golden Sky Dome from Mjövik" in SE Sweden, the rock-carving at Stora Backa at Brastad in SW Sweden and on a stone tablet from the ancient Sun-temple at Sippar in Mesopotamia. All these three objects are from the Bronze Age.

The six-spoke Sun wheel symbols record the course of a year in six segments all representing 60 days per segment and 360 days in total for the whole year (as further discussed in papers [10] and [11]). It was a novel finding calling for ex-

tended research.

Therefore, one of us (B.G.L) stated an investigation of Scandinavian rock-carvings and ornaments on Bronze Age objects in Scandinavia. And, lo and behold, he soon found what he was searching for. In the National Museum in Copenhagen, there was an old drawing from the 1840s showing 9 six-spoke Sun wheels [12] [13]. In this paper, we will for the first time describe this object, its origin, history and implication for our understanding of Bronze Age astronomy.

2. A Bronze Age Mound at Høbbehøjen in Denmark

The Bronze Age mound at Høbbehøjen was in today's Vestre Sæby on Sjælland (**Figure 1**). The mound included two burial chambers. In the southern chamber, there were human bones, not burned, a large number of flint object and numerous pieces of yellow amber. In the northern chamber, there was a lot of soot from cremation, and remains of a horse, which might have followed his master in death. The image stone here described was found in the southern grave.

The grave was found in 1840 and excavated by the nearby estate owner Count J. Raben in his hunting for gold. An image stone was found, but ignored by the gold hunting count.

2.1. A Stone with Rock Carvings

The rumor of the image stone reached Copenhagen in a few days, however. The Danish war councilor S. Schiøtz heard about it and immediately travelled to the site, where he made a careful drawing of the stone and its rock carvings. In 1842, he gave the drawing to the National Museum in Copenhagen (on October 6, 1842), where it has been lying since then with little recognition [12] [13] up to this paper.

Figure 1. Location of Høbbehøjen at today's Vestre Sæby on Sjælland in Denmark.

2.2. A Remarkable Bronze Age Image

The rock carvings on the Høbbehøjen image stone are quite remarkable (Figure 2). A group of 9 six-spoke Sun wheels are shown together with two semilunar arcs. The 9 Sun wheels are obvious analogues to the ones described on "the Golden Sky Dom of Mjövik", the rock carving at Stora Backa in Brastad and from the Sun-temple at Sippar in Mesopotamia as discussed in [10] and [11].

All the 9 Sun wheels consist of a circle, which is crossed by three lines; one in N-S direction, one in E-W direction and one in NW-SE direction. The one in NW-SE is of special interest as it co-insides with the direction of sunset at summer solstice in NW and of sunrise at winter solstice in SE (whilst this is the case in sun wheals 1, 4, 5, 7 and 8, the diagonal line is somewhat steeper in sun wheels 2, 3, 6 and 9, a variation which probably belongs to the drawing).

The two semilunar arcs are likely to represent solar eclipses.

Eight of the nine Sun wheels are well ordered in rows. The 9th position is taken by a symbol of an eclipse and the ninth Sun wheel is pushed aside. This cannot have been done without a reason.

2.3. A Sad Vandalizing

The farmer owning the ground of the Høbbehøjen mound destroyed the mound with its graves and image stones. He is said to have blown it up with gunpowder. Therefore, the only image left is the one made by Schiøtz in 1840 and handed in to the National Museum in 1842 (plus the drawing by geologist Steenstrup made of another image stone and handed in to the National Museum in 1887).

3. Interpretations

The six-spoke Sun wheels we interpret in terms of annual solar calendars composed of six 60 days segments making a full annual cycle of 360 days, like we did with the other six-spoke objects [10] [11]. It is a manifestation of the sexagesimal

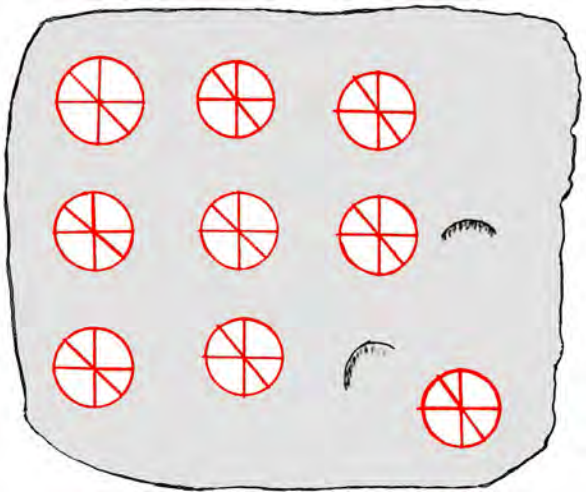

Figure 2. The 9 six-spoke Sun wheels and 2 solar eclipses on the image stone in the Bronze Age mound at Høbbehøjen as drawn by Schiøtz in 1840.

mathematical system originating in Mesopotamia [14]. The two semilunar arcs, we interpret in terms of solar eclipses. So far the interpretations agree well with previously described objects [10] [11].

The arrangements of the 9 solar symbols and the 2 eclipse symbols on the image stone (**Figure 2**) call for additional interpretation.

One six-spoke Sun wheel represents an annual calendar of one year. Therefore, it seems highly likely that the 9 Sun wheels represent 9 years.

On the Høbbehøjen image stone (**Figure 2**), there are 8 very well ordered Sun wheels, and then a 9th one dislocated to the side by the appearance of one of the semilunar arc symbols. Therefore, it seems that something unusual happened every 9th year.

According to Henriksson [15], Sjælland experienced 3 total solar eclipses in the Bronze Age, viz. at 858, 1521 and 1596 BC, implying that an interpretation in terms of solar eclipses may well be correct, though still unconfirmed.

3.1. Magic of Number 9

Obviously, number 9 had some special implications in ancient belief and handling. Zeus and Mnemosyne had 9 daughters, the Nine Muses, all goddesses of music, poetry, art and science. In the Asa Cred, nine was a very important number. In order to obtain all earthly and spiritual knowledge, the God Odin had to hang in the world-tree Yggdrasil for 9 sun-days and 9 moon-nights. His son Heimdall, the Sun-god, was born by 9 virgin mothers at the sun rise at the horizon of the sea.

Adam of Brehmen [16] mentioned that, at the holy place at Leire on Sjælland in Denmark, extensive feasts were performed every 9th year at winter solstice. The feast went on for 9 days and every day one person and 7 animals were sacrificed. He also describes sacrifice rite at Uppsala in Sweden. At winter solstice, 9 humans and animals of masculine gender were sacrificed, and then hanged up in trees close to the temple [16].

Therefore, we believe that there was something special and magic with number 9 from the Bronze Age and into the Late Iron Age. It seems that this is some sort of background to the carving of 9 Sun wheels on the Høbbehøjen image stone (**Figure 2**).

3.2. Solar Alignment

Ales Stones is a remarkable monument of clear astronomical dimensions in Southern Sweden [2] [9] [11]. The form is a stone ship of 69 meter's length, and it is strictly aligned in NW-SE direction: *i.e.* in the straight line of sunrise at winter solstice in the SE and of sunset at summer solstice in the NW. The arrangements of the side-stones give 11 months of 30 days and 1 month (July) of 35 days, giving a full year of 365 days.

The NW-SE line in the Sun wheels of Høbbehøjen has exactly the angle with respect to N-S and E-W as the symmetry axis of Ales Stones (**Figure 3**).

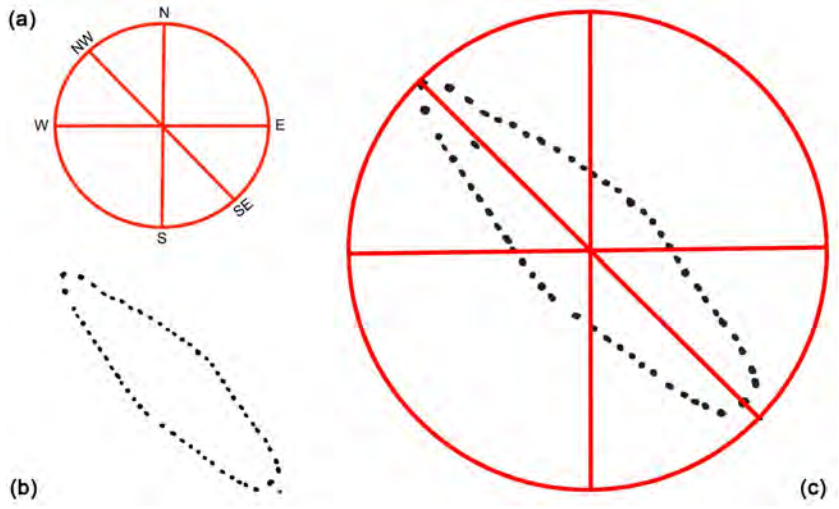

Figure 3. The NW-SE line in the 9 Sun wheels of (a) has the same angle as the long-axis of Ales Stones (b); and when superposed there is a perfect agreement (c). This lends strong support to a cultural connection. The Høbbehøjen symbol has a diameter of 10 - 20 cm, whist the Ale Stones are 69 m long and 19 m wide.

3.3. Geographical Impact

Six-spoke Sun wheel are now found in the Sun temple in Sippar in Mesopotamia, on the Golden Sky Dome of Mjövik in SE Sweden, on the rock carving at StoraBacka (Brastad) in SW Sweden, and the stone carving at Høbbehøjen in Denmark (**Figure 4**). Ales Stones are closely related because of its deep astronomical principles.

This implies that the astronomical knowledge was well established in the Bronze Age all from Mesopotamia to Scandinavia.

There is still another six-spoke Sun wheel: the Golden Sun-disk from Glüsing in Schleswig-Holstein [17], but the original is so fragmentary [18] that the reconstruction remains hypothetical.

4. Conclusions

A new astronomical image from the Bronze Age is presented. The image (a drawing from 1840) was found in the archive of the Natural Museum in Copenhagen [12] [13], where it has been lying for 174 years without any deeper analysis.

It shows 9 six-spoke Sun wheels and two semilunar arcs. The Sun symbols agree well with our previous described objects with six-spoke Sun wheels [10] [11].

The spokes are not equally distributed in the wheel. Besides a vertical and a horizontal line, there is a diagonal line in NW-SE. This line co-insides with the symmetry line of Ales Stones, and the straight line between sunrise at winter solstice in the SE and the sunset at summer solstice in the NW: *i.e.* the solar motion over the sky during a year, backing up the interpretation that we are dealing with Sun wheels.

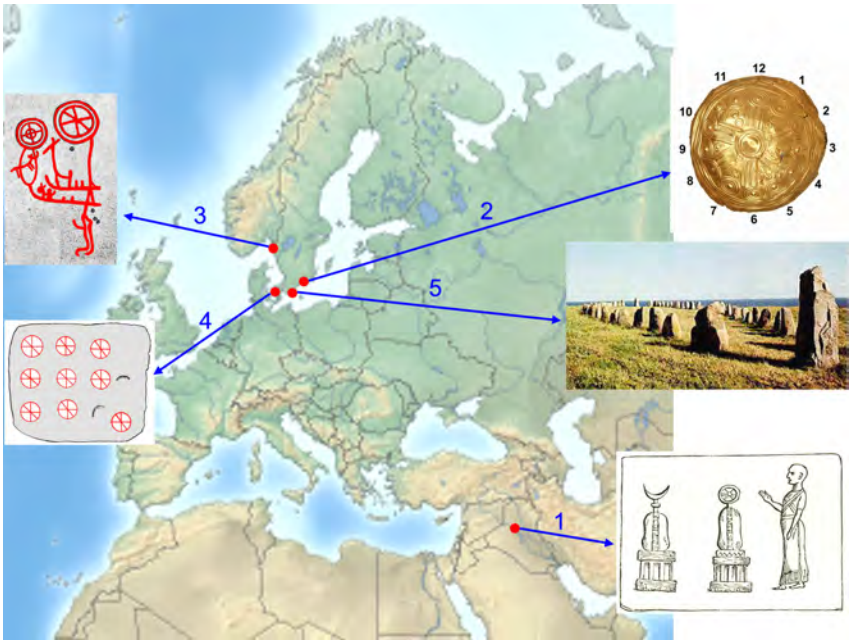

Figure 4. Geographical location of the five objects discussed, indicating that the Bronze Age people had a deep knowledge in astronomy all from Mesolotamia (1) to Scandinavia (2 - 5).

The geographical distribution of six-spoke Sun wheels (**Figure 4**) indicates the wide spread in the Bronze Age of this symbol of Sun cult [11] all from Mesopotamia to Scandinavia in the northwest.

Conflicts of Interest

The authors declare no conflicts of interest regarding the publication of this paper.

References

[1] Henriksson, G. (1999) Prehistoric Constellation on Swedish Rock-Carvings. *Actes Vème Conference*, Gdansk, 5-8 September 1997, 155-173.

[2] Lind, B.G. (2005) Alesstenar som solkalendarium. *Ale*, **4**, 21-24.

[3] Mörner, N.-A., Lind, B.G. and Possnert, G. (2009) Heimdall's Stonesat Vitemölla in SE Sweden and the Chronology and Stratigraphy of the Surroundings. *GeografiskaAnnaler*, **91A**, 205-213. https://doi.org/10.1111/j.1468-0459.2009.00364.x

[4] Mörner, N.-A. and Lind, B.G. (2010) A Mediterranean Trading Centre in Southeast Sweden. In: Paraminopoulos, S.P., Ed., *The Atlantis Hypothesis—Commentary*, Heliotopos Publication, Athens, 685-699.

[5] Mörner, N.-A. (2012) Strict Solar Alignment of Bronze Age Rock Carvings in SE Sweden. *Journal of Archaeological Science*, **39**, 3301-3305. https://doi.org/10.1016/j.jas.2012.05.027

[6] Mörner, N.-A. and Lind, B.G. (2012) Stonehenge Has Got a Younger Sister. Ales Stones Decoded. *International Journal of Astronomy and Astrophysics*, **2**, 23-27. https://doi.org/10.4236/ijaa.2012.21004

[7] Mörner, N.-A. and Lind, B.G. (2013) The Bronze Age in SE Sweden—Evidence of

Long-Distance Travel and Advanced Sun Cult. *Journal of Geography and Geology*, **5**, 78-91. https://doi.org/10.5539/jgg.v5n1p78

[8] Mörner, N.-A. and Lind, B.G. (2015) Long-Distance Travel and Trading in the Bronze Age: The East Mediterranean-Scandinavian Case. *Archaeological Discovery*, **3**, 129-139. https://doi.org/10.4236/ad.2015.34012

[9] Mörner, N.-A. (2015) Ales Stones in SE Sweden: A Solar Calendar from the Late Bronze Age. *Journal of Archaeological Sciences: Reports*, **2**, 437-448. https://doi.org/10.1016/j.jasrep.2015.04.002

[10] Mörner, N.-A., Lind, B.G. and Henriksson, G. (2018) A Golden Calendar from the Bronze Age. *Archaeological Discovery*, **6**, 53-61. https://doi.org/10.4236/ad.2018.62004

[11] Mörner, N.-A. and Lind, B.G. (2018) Astronomy and Sun Cult in the Swedish Bronze Age. *International Journal of Astronomy and Astrophysics*, **8**, 143-162. https://doi.org/10.4236/ijaa.2018.82010

[12] Petersen, H. (1875) Om Hellristninger i Denmark. Aabøger for nordisk Oldkyndighed og Historie.

[13] Glob, P.V. (1969) Hellristninger i Danmark. Gyldendals.

[14] Ifrah, G. (1994) Histoire Universelle des Chiffes. Robert Laffont, Bouquins.

[15] Henriksson, G. (2018) Personal Communications, September 25, 2018, Applying His Model Presented in *Advances in Astrophysics*, **2**, 184-196 (2017).

[16] Adam of Brehmen (1075/76) Gesta Hammaburgensis Ecclesiae Pontificum.

[17] Struve, K.V. (1957) Die Kultur der Bronzezeit in Schleswig-Holstein. Schleswig-Holstein Landesmuseum, Hefte 8, Karl Wachholtz Verlag, Neumünster.

[18] Goldscheibe Glüsing. http://www.museum-albersdorf.de/poster/goldscheibe.htm

International Journal of Astronomy and Astrophysics, 2018, 8, 306-322
http://www.scirp.org/journal/ijaa
ISSN Online: 2161-4725
ISSN Print: 2161-4717

Spatial Distribution of Radiation Belt Protons Deduced from Solar Cell Degradation of the Arase Satellite

Honoka Toda[1*], Wataru Miyake[1], Yoshizumi Miyoshi[2], Hiroyuki Toyota[3], Yu Miyazawa[3], Iku Shinohara[3], Ayako Matsuoka[3]

[1]Department of Aeronautics and Astronautics, Tokai University, Kanagawa, Japan
[2]Institute for Space-Earth Environmental Research, Nagoya University, Nagoya, Japan
[3]Institute of Space and Astronautical Science, JAXA, Kanagawa, Japan
Email: *8bemm060@mail.u-tokai.ac.jp

How to cite this paper: Toda, H., Miyake, W., Miyoshi, Y., Toyota, H., Miyazawa, Y., Shinohara, I. and Matsuoka, A. (2018) Spatial Distribution of Radiation Belt Protons Deduced from Solar Cell Degradation of the Arase Satellite. *International Journal of Astronomy and Astrophysics*, **8**, 306-322.
https://doi.org/10.4236/ijaa.2018.84022

Received: October 3, 2018
Accepted: November 11, 2018
Published: November 14, 2018

Abstract

Analysis of solar-cell array panel (SAP) data from the Arase satellite orbiting in the inner magnetosphere showed a clear degradation of solar cells that could be attributed to trapped protons with energies greater than 6 MeV. Proton fluence was determined based on variations in the open-circuit voltage (Voc) of the solar cells, which we compared with that expected based on various distribution models (AP8MAX, AP9 mean and CRRESPRO quiet) of trapped protons. We found a general agreement, confirming the major contribution of trapped protons to the degradation, as well as a slight difference in the fluence expected based on the model calculations. To minimize this difference, we slightly modified the models, and found that concentrating the energetic protons on the magnetic equator provided a better agreement. Our results indicate that >6 MeV protons also has the equatorial concentration as reported for >18 MeV protons from the Van Allen Probes observation, and are interpreted as two components of the trapped protons, *i.e.*, those of solar energetic particle (SEP) origin have an anisotropic pitch-angle distribution and are confined near the magnetic equator.

Keywords

Arase Satellite, Proton Radiation Belt, Solar Cell Degradation

1. Introduction

The inner radiation belts are mainly populated by energetic protons. Recent observations with the Van Allen Probe [1] have clearly demonstrated that the

energetic protons consist of two components, *i.e*., protons of solar energetic particle (SEP) origin and those of cosmic ray albedo neutron decay (CRAND) origin [2]. Trapped protons of SEP origin have rather lower energies, and a great concentration near the magnetic equator at larger L-shells. These properties are quite important for understanding proton injection, transport, and loss processes in the inner magnetosphere. They are revealed for protons with energies greater than 18 MeV. Since proton measurement with the Van Allen Probes has a gap of proton energies between 1 and 17 MeV [3], properties of several to ten MeV protons have not been studied.

Cumulative damage from space radiation generally decreases the output power of solar cells used in space. Ishikawa *et al.* [4] reported the decrease in output current of silicon solar cells of the Akebono satellite orbiting in the inner magnetosphere, and carried out a correlation study to identify possible causes of the degradation. They found that the trapped component of energetic (>10 MeV) protons in the radiation belt is mainly responsible for the decrease in output current. Miyake *et al.* [5] [6] further analyzed the variation in output current of the Akebono solar cells between 1989 and 1996, and pointed out that the proton radiation belt was more sharply confined than that given by the AP8 model. We realized from these earlier studies that by analyzing the degradation of solar cells, we can indirectly study the proton radiation belt.

The Arase (formerly known as the Exploration of energization and Radiation in Geospace, ERG) satellite was successfully launched on December 20, 2016, from the Uchinoura Space Center. The spacecraft has apogee and perigee altitudes of ~32,000 and ~440 km, respectively, and an inclination of 32˚, allowing the spacecraft to spend the majority of its time in the radiation belts. The spacecraft has an orbital period of 570 min and is spin-stabilized with a spin period of ~8 s. The primary objective of the Arase mission is to reveal the generation mechanisms of relativistic electrons in the radiation belts [7].

The Arase satellite measures electrons within a wide energy range, whereas the measurement of ions is carried out only below 180 keV, mainly for ring current particles [8]. Its solar array panel (SAP) data clearly shows the degradation of solar cells by space radiation, probably by energetic protons in the inner radiation belt. The cover glass of the solar cells has a thickness of 0.3 mm, which means that protons with energies greater than 6 MeV can penetrate into the solar cells [9]. In this paper, we present the results of analyzing the degradation of solar cells on the Arase satellite and deduce the spatial distribution of >6 MeV protons which are never measured by particle instruments on the Van Allen Probes and the Arase satellite. We first assume that the degradation of solar cells of the Arase satellite is caused only by trapped protons. Generally, solar energetic protons and trapped energetic electrons are both responsible for the degradation of the satellite's solar cells depending on the orbit and solar activity. We discuss the possible contribution of other causes for the degradation later.

Cumulative damage from energetic particles causes the solar cell degradation, so our analysis presents only the integration along satellite orbit over a long time

and needs a given state of particle distribution. Our approach is solving an inverse problem, in which a model distribution is estimated from the integration of proton flux, and generally the solutions are not unique. We therefore start with a model distribution which is close to the solution, and then slightly modify the model for seeking a better agreement with the degradation of solar cells.

For the first step, we used three empirical models of trapped MeV protons: AP8MAX, AP9 mean (ver. 0.0), and CRRESPRO quiet. The standard space environment specifications used for spacecraft design have been provided by NASA's AE8 and AP8 models for decades. They were developed from measurements accumulated by numerous satellites in the 1960s and 1970s. There are well-known limitations on their performance, and the need for a new trapped radiation and plasma model was recognized by the engineering community some time ago. To address this challenge, a new set of models, denoted AE9/AP9/SPM, for energetic electrons, energetic protons and space plasma was recently developed [10]. The CRRES satellite provided observation of energetic particles from July 1990 to October 1991 in the inner magnetosphere [11]. An intense solar proton event and subsequent geomagnetic storm drastically changed the trapped particle environment in March 1991. The CRRESPRO quiet model was developed based on proton data obtained before the event.

We have organized the rest of the paper as follows. The data used and method to deduce variation of proton fluence from the degradation of solar cells are described in the next two sections. Our approach is not based on direct particle measurement, and we need some analysis on performance of solar cells to deduce the proton fluence. We then compare the temporal variation of proton fluence with that expected from various model distributions. Finally we discuss probable interpretation of our results on proton fluence and spatial distribution of >6 MeV protons.

2. Data

The open-circuit voltage Voc, short-circuit current Isc, and voltage and current at maximum power, Vmp and Imp, are generally used for describing the I - V characteristics of solar cells [12]. The output current is almost identical to Isc for a wide range of operating voltages as long as the solar cells are operated at a voltage lower than the Vmp. The output current begins to decrease near the Vmp. When the operating voltage exceeds the Vmp and comes close to the Voc, the output current drastically decreases towards zero. The solar cell system of the Arase satellite is operated between the Vmp and Voc, so that the voltage decreases slightly and the current increases significantly when more electric power is consumed by the satellite's systems.

When energetic particles collide with solar cells, they penetrate into the cells and damage the inside with scratches, causing a reduction in electric power. For this reason, the efficiency of solar cells decreases as the radiation exposure increases. This effect accumulates year by year, and its influence is greater in the early stage of operation. Accumulated radiation damage causes a decrease in all

four solar cell parameters: Voc, Isc, Vmp and Imp. As the damage accumulates, the output voltage of the Arase satellite decreases towards Vmp and the current increases towards Imp if the satellite needs constant electric power.

Figure 1 shows the output voltage (upper panel) and the current (lower) from the solar cells of the Arase satellite from its launch through to March 31, 2018, which is all the data used in this study. The satellite has four SAPs and the total output current from the four panels is presented. The SAPs are covered by InGaP/InGaAs/Ge ZTJ solar cells from SolAero Technologies Corporation. Corrections for incident solar light are already made for variations in the SAP's orientation and for seasonal variations in the radial distance from the sun. The cover glass of the solar cells has a thickness of 0.3 mm, which means that protons with energies greater than 6 MeV can penetrate into the solar cells [9].

The overall trend of the voltage and current variation shown in Figure 1 is consistent with that expected from the degradation of solar cells due to accumulated damage from space radiation. The voltage decreased and the current increased. However, particle fluence is not the only factor affecting the output of solar cells. The output voltage and current are also affected by the temperature of solar cells, which ranges widely from low to high values for an Earth-orbiting satellite. Voc decreases under high temperature conditions, although Isc is only slightly affected. To precisely deduce the radiation effect, it is necessary to carefully evaluate and remove the effect of temperature variation.

Since the SAPs are well thermally isolated from the satellite, there are two sources of temperature variation. One is due to the effects of the Earth. To avoid these effects, we sorted the data based on two orbit conditions. We selected data taken at more than 4.0 Re from the Earth's shadow. The SAPs are cooled down in the shadow and it takes a certain amount of time to reach thermal equilibrium again in sun-lit conditions. We also selected data taken at a radial distance of more than 5.0 Re from the Earth for the purpose of minimizing the effect of the Earth's albedo and heat radiation.

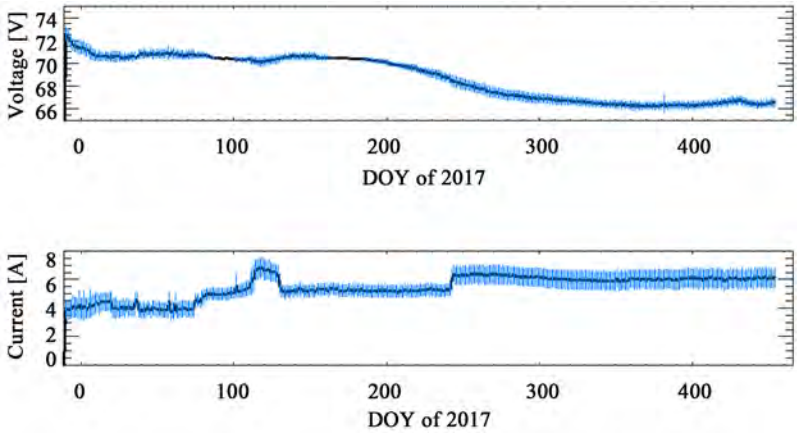

Figure 1. Variation of solar cell output voltage (upper panel) and current (lower panel) of the Arase satellite from its launch to March 2018. Blue vertical lines indicate the standard deviation.

The sun is another source affecting the SAP's temperature. Heat input from the sun varies between the aphelion (early July) and the perihelion (early January) of the Earth. We needed to model the temperature variation, since heat input from the sun is unavoidable and there are no temperature sensors on the SAPs. The method is described later.

3. Analysis

To deduce the proton fluence, we first drew a curve of the I - V characteristics passing through the daily average voltage and current of the SAPs, as presented in Figure 1. The I - V curve is expressed by an exponential function. Then we determined Voc for the day at the point of I = 0 in the I - V plane. Figure 2 shows the relative variation of the daily Voc from that at the beginning of life (BOL). Vertical bars represent the standard deviation for the daily average. We used the Voc variation in this study, since Voc is the most sensitive to particle fluence among the parameters describing I - V characteristics. The data sheet for the ZTJ cells gives a 5% decrease in Voc, but a 2% decrease in Isc from the BOL for fluence of 1014 e/cm^2.

Fast decrease and rather stable periods are alternately repeated for the Voc variation in Figure 2. Fast decrease periods may correspond to large fluence and stable periods to small fluence. Figure 3 shows an example of Arase's orbits on DOY 76 (black lines) and DOY 151 (red lines) in geomagnetic coordinates. Orbits in the southern hemisphere are folded up to the northern hemisphere. The Arase satellite entered the heart of the proton radiation belt (*i.e.*, around L = 1.5 on the Equator) on DOY 151, but did not do so on DOY 76. The same variation in orbit is repeated with a period of about 8 months due to orbit precession. Faster decrease of Voc was expected on DOY 151, but the fact is that Voc was just as stable as it was on DOY 76.

The deviation from the expected fast decrease and stable periods demonstrates that particle fluence is not the only factor controlling Voc. The temperature of the SAPs should be highest around early January and lowest around early July due to the eccentricity of the Earth's orbit around the sun. The lower temperature

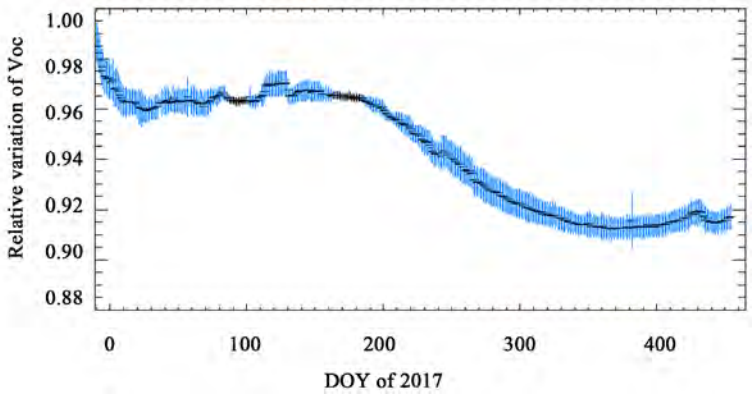

Figure 2. Daily averaged Voc from the satellite's launch to March 2018. Blue vertical bars indicate the standard deviation.

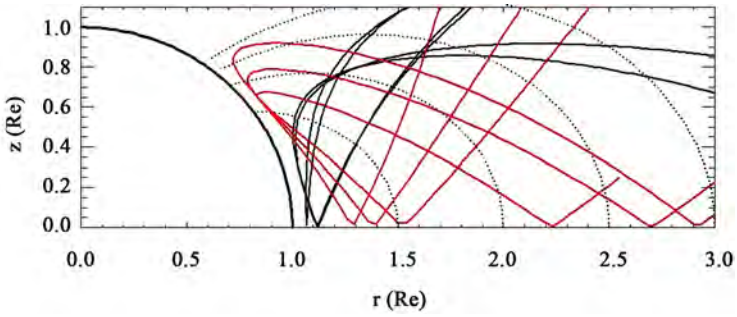

Figure 3. Orbits of the Arase satellite on DOY 76 (black line) and DOY 151 (red line) in geomagnetic coordinates. Orbits in the southern hemisphere are folded up to the northern hemisphere.

on DOY 151 compared to that on DOY 76 has the effect of increasing Voc, which may compensate for the decrease by large particle fluence around DOY 151. The data sheet for the ZTJ cell used for the Arase satellite shows a 0.23% - 0.25% decrease in Voc for a temperature increase of 1˚C during the early stage of degradation. Engineers estimated a variation of ~10˚C between the aphelion (early July) and the perihelion (early January) through thermal analysis of the satellite before its launch. Therefore, Voc variation of several percent can be attributed to temperature variation.

Since there are no temperature sensors on the SAPs, we introduced a simple model of SAP temperature based on thermal equilibrium. The SAPs are well isolated from the satellite body and heat conductance is negligible. The only heat input is from solar radiation, which varies proportionally with 1/R2, the inverse of the squared radial distance from the sun. Loss is caused only by heat radiation toward space, which is proportional to σT^4, where σ is Stefan's constant and T is the Kelvin temperature of the SAPs. If we give the amplitude of the annual temperature variation, *i.e.*, the difference between the aphelion and perihelion, then we can deduce the relative fluence from the Voc variation in **Figure 2**.

Figure 4 shows the monthly average relative fluence deduced for three cases of amplitude of the annual temperature variation. Fluence is normalized with respect to the fluence of the last month, March 2018. The relative fluence for 0˚ variation decreases from DOY 30 to DOY 130, and around the last DOY interval. Any decrease in fluence cannot be real, so some annual variation of temperature should inevitably be included in our model calculations. A case of 5˚ variation seems better, but still has a small decrease of fluence around the last DOY interval. On the other hand, the fluence increases continuously for a 10˚ variation, which is most reasonable among the three cases. Variation in the speed of increasing fluence is caused by the orbit precession, as shown in **Figure 3**, and is key to investigating the best-fitting models for the spatial distribution of energetic protons.

In this study, we first tried three empirical models for the spatial distribution of energetic protons: CRRESPRO quiet, AP8MAX, and AP9 mean (ver. 0.0). Then, we modified these models seeking better agreement with the SAP data.

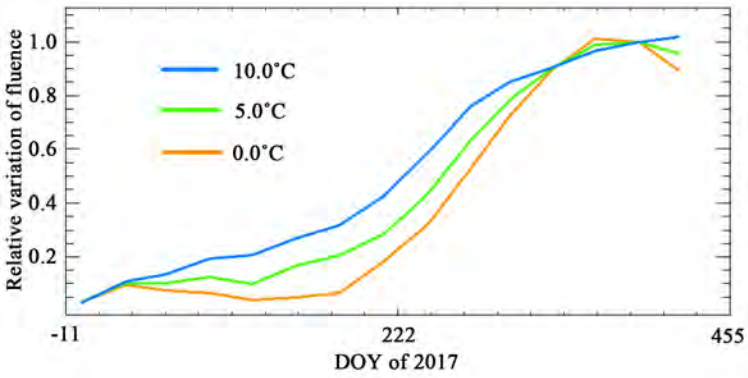

Figure 4. Relative fluence deduced from monthly averaged Voc by assuming the amplitude of annual variation of temperature as indicated in the figure. Each relative fluence is normalized by its maximum value.

The amplitude of the annual temperature variation is a free parameter in our model calculations. We changed it in 0.1˚ steps to find the amplitude that provided the best fit with the fluence variation for the given model of spatial distribution.

4. Comparison with Various Models of Proton Distribution

Figure 5 shows a comparison between the relative fluence deduced from the SAP data (blue line) and the calculated fluence from integration along the satellite orbit under the spatial distribution of energetic protons of each model (red line). The fluence is normalized by that of the last month. The fluence for CRRESPRO quiet, AP8MAX, and AP9 mean of the last month is 5.0e+11/cm^2, 1.6e+12/cm^2, and 8.1e+11/cm^2, respectively. The radiation damage coefficient (RDC) method is often used for evaluating the degradation of solar cells [13]. We are unable to use detailed figures of the solar cells in this study due to a contract with the manufacturer. Accordingly, we focus on temporal variation of the relative fluence, not the absolute values. If the RDC method were fully used, the difference among the three proton models would be quite clear. The AP8MAX has the highest fluence among the three models and would certainly give the fastest degradation.

We used the amplitude of annual temperature variation (ΔT) that provides the minimum root mean squared error (RMSE) for each model. The RMSE is largest for AP8MAX, and smallest for AP9 mean. The amplitude of annual temperature variation spreads slightly among the models, and is around 9˚. The three models differ in proton distribution (see bottom panel (C) in **Figures 6-8**), but we still obtained an overall coincidence with the fluence deduced from the SAP data, indicating that trapped protons are mainly responsible for degradation of the solar cells of the Arase satellite.

Although the RMSE differs among the three models, the deviation of the red line from the blue line is found almost at the same intervals. The first deviation is around DOY 50. The second and third deviations are around DOY 155 and

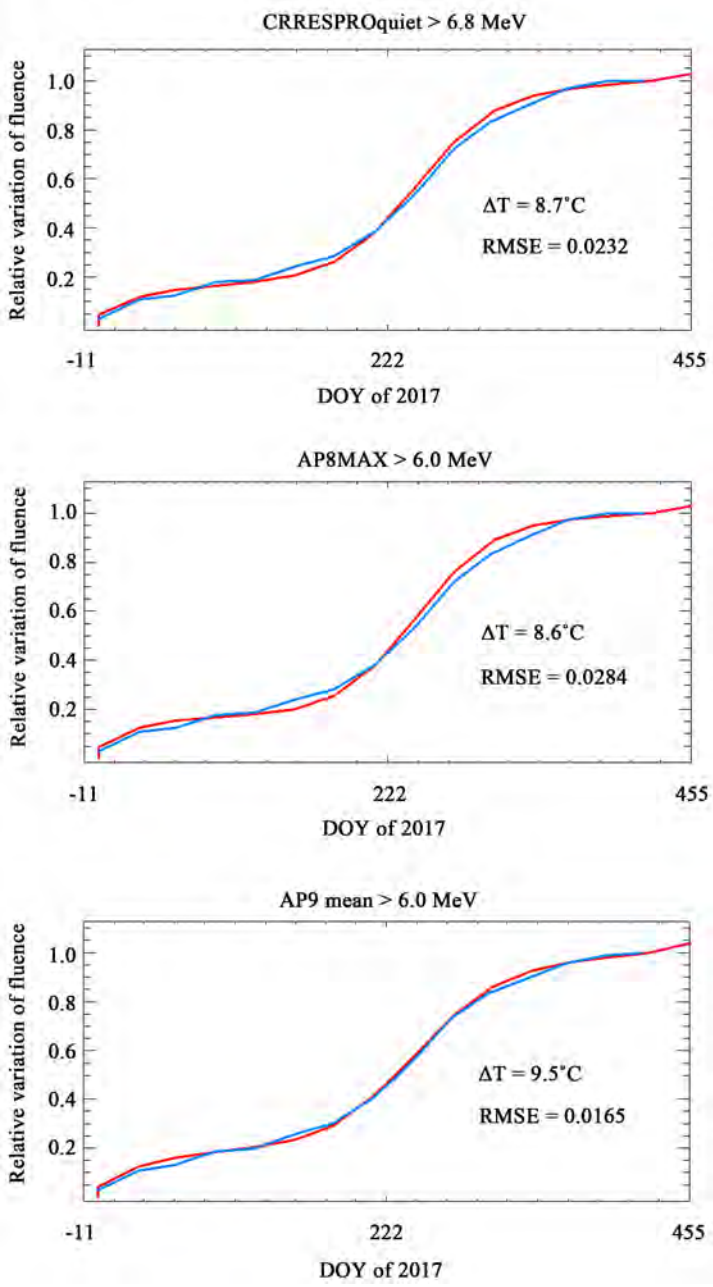

Figure 5. Comparison between the relative fluence deduced from the SAP data (blue line) and the calculated fluence from integration along the satellite orbit under the spatial distribution of energetic protons of the three models (red line). The fluence is normalized by that of the last month. We used the amplitude of annual temperature variation (ΔT) that gives the minimum RMSE (root mean squared error) for each model.

DOY 315, respectively. The relative fluence deduced from the SAP data (blue line) is larger for the deviation around DOY 155, and smaller for the other two cases. The similar pattern of deviation throughout the different models suggests a common cause. There are several possibilities, which we discuss later, but here we look at the possibility of slightly modified models for the trapped proton distribution.

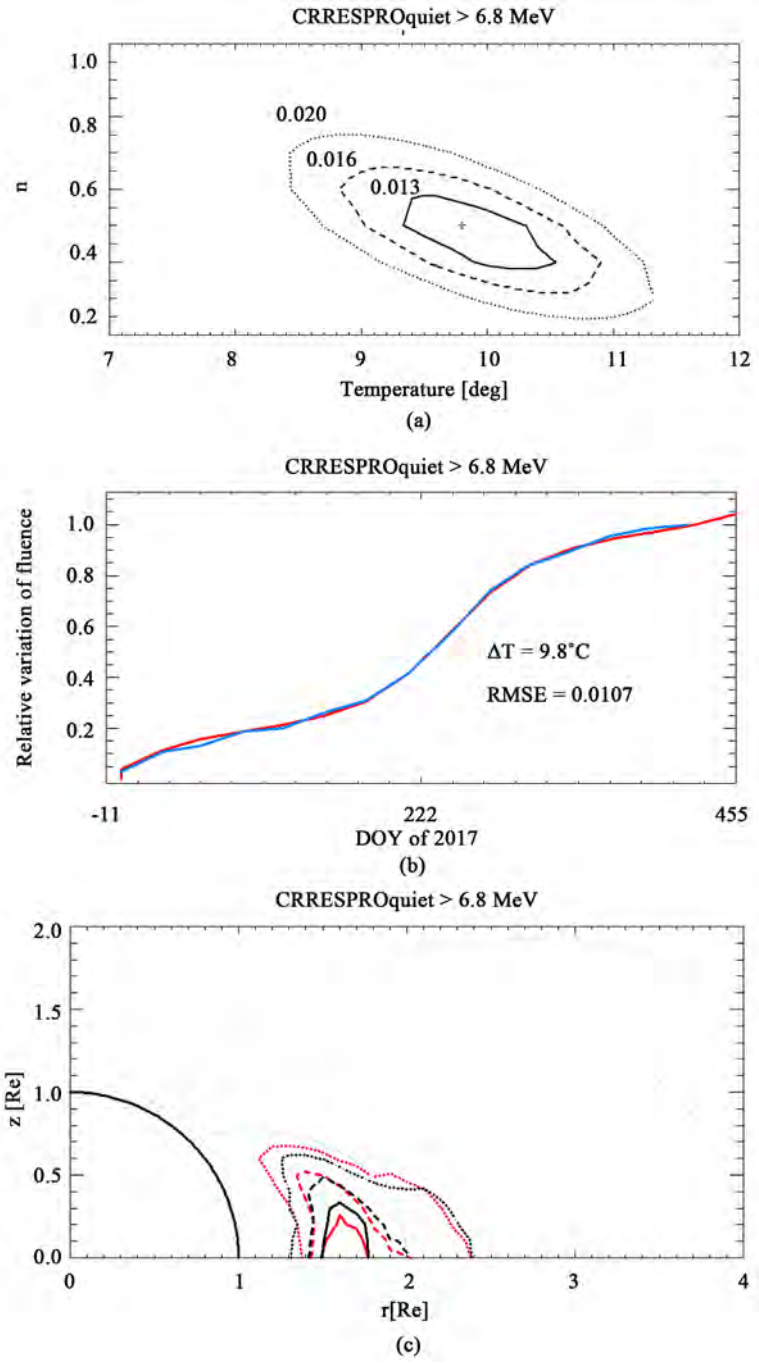

Figure 6. Summary for the modified CRRESPRO quiet model. (a) Contour map of RMSE between the relative fluence deduced from the SAP data and the calculated fluence from integration along the satellite orbit under the spatial distribution of >6.8 MeV protons of modified CRRESPRO quiet model. The RMSE is presented as a function of the amplitude of annual variation of temperature (ΔT) and n in Equation (1); (b) Variation of relative fluence deduced from the SAP data (blue line) and calculated from integration along the satellite orbit under the spatial distribution of >6.8 MeV protons of the modified CRRESPRO quiet model (red line); (c) Contour plot of the spatial distribution of >6.8 MeV protons of the original CRRESPRO quiet model (black line) and the modified model (red line). The solid, broken, and dotted lines represent 60%, 30%, and 10% of the peak flux, respectively.

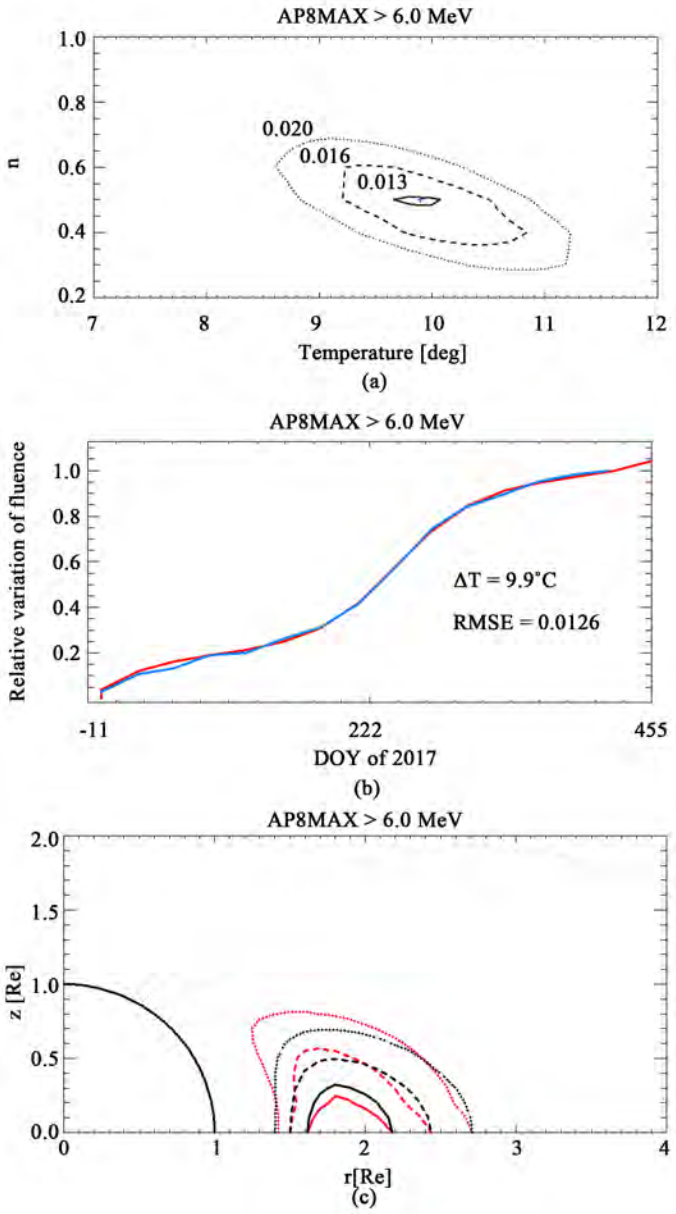

Figure 7. Summary for the modified AP8MAX model. The formats of each panel are the same as that used in **Figure 6**.

Trapped protons are generally divided into two components, *i.e.*, protons of SEP origin and those of cosmic ray albedo neutron decay (CRAND) origin. Observation by Van Allen Probes revealed that energetic protons in the inner belt have highly anisotropic pitch-angle distribution on the magnetic equator at larger L values, and that this tendency is more evident for lower-energy (26 MeV) protons. This anisotropy is interpreted in terms of a component of injected and trapped solar protons [14]. Proton energy affecting SAP degradation is more than 6 MeV, which is even lower than that in the report above, so we tried models of spatial distribution with an equatorial enhancement of proton flux at large L values. We introduced a slight modification to the three models by

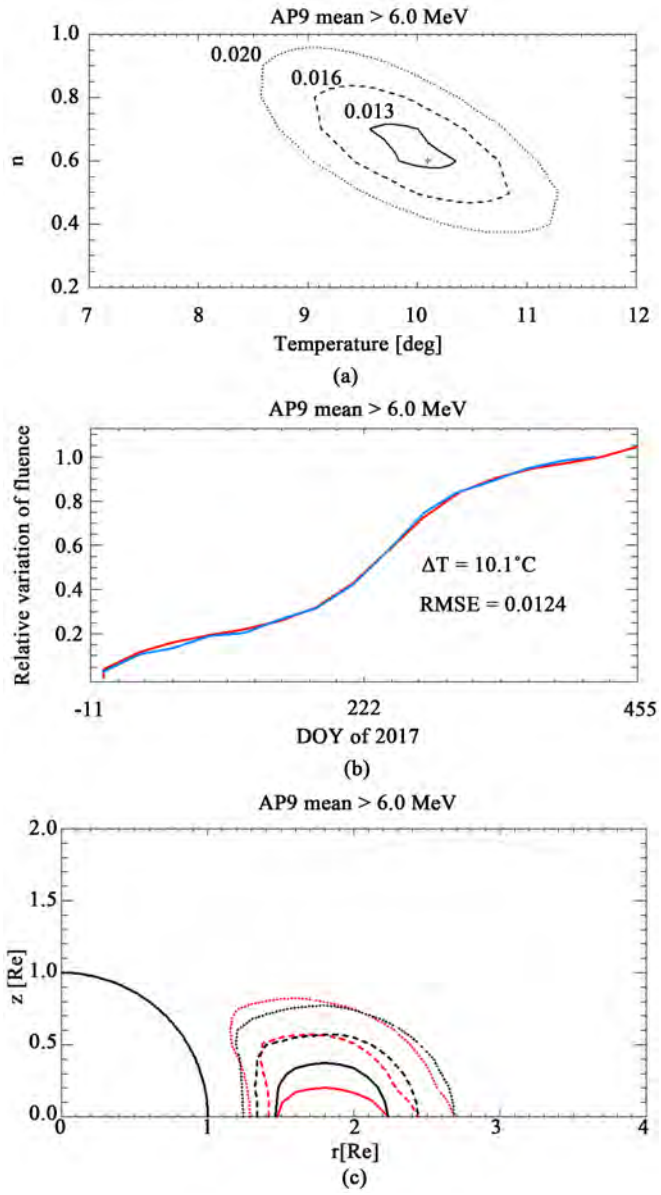

Figure 8. Summary for the modified AP9 mean model. The formats of each panel are the same as that used in **Figure 6**.

increasing the proton flux at z < 0.2 Re for L > 1.5, where z is the distance from the magnetic equator. For example, we set the proton flux at 2.0 times that of the original flux at z < 0.1 Re and 1.5 times at 0.1 Re < z < 0.2 Re of the original flux. This modification is a way of simulating one component, the SEP-derived trapped protons that are expected to concentrate near the magnetic equator.

To represent the other component, protons of CRAND origin, we also modified the proton flux distribution off the equator (z > 0.2 Re) along the field line following the equation

$$f = \left(\frac{f'}{f_{eq}} \right)^n f_{eq} \tag{1}$$

where f' is the flux of the original model at a point, and f_{eq} is the flux of the modified model on the magnetic equator with the same L value. Parameter n determines the overall distribution along the field line. The additional equatorial enhancement means that flux relative to the equator flux away from the equator decreases more drastically than the original model if we set $n > 1$. If we want only an equatorial enhancement without significantly changing the relative flux away from the equator, parameter n should be smaller than unity.

Figures 6-8 summarize the results for the modified CRRESPRO quiet, AP8MAX, and AP9 mean models, respectively. Here, we introduce a flux enhancement of 2.0 times at z < 0.1 Re and 1.5 times at 0.1 Re < z < 0.2 Re for L > 1.5 for all three models. We changed ΔT, the amplitude of annual temperature variation, by steps of 0.1˚, and n in Equation (1) by a 0.1 step, and looked for the best agreement between the fluence deduced from the SAP data and that from the spatial distribution model for energetic protons.

The top panel (A) of each figure shows a map of the RMSE as a function of the amplitude of annual variation of temperature (ΔT) and n in Equation (1). The blue mark + denotes the location of the minimum RMSE. The minimum RMSE is given in the middle panel (B). We present the monthly averaged fluence deduced from the SAP data (blue line) and the fluence integrated from the spatial distribution along the orbit in the middle panel (B) for the minimum RMSE. The bottom panel (C) of each figure shows a comparison of the spatial distribution of the original model (black lines) with that of the modified model (red lines). The original CRRESPRO quiet, AP8MAX, and AP9 mean (black lines) have a peak flux of 5.3e+5/cm^2/s, 1.1e+6/cm^2/s, and 4.7e+5/cm^2/s, respectively. The contour levels are normalized by the peak flux, and 60% (solid lines), 30% (broken lines), and 10% (dotted lines) levels are presented. Blue dotted lines show geomagnetic field lines of L = 2, 3, 4, and 5.

The minimum RMSE of 0.0107 is found at 9.8˚C and n = 0.5 for the modified CRRESPRO quiet model in Figure 6. This RMSE is better than 0.0232 for the original CRRESPRO quiet model shown in the upper panel of Figure 5. Similarly, the minimum RMSE for the modified AP8MAX and AP9 mean models is improved from the original values. We found that the deviations in the second (around DOY 155) and third intervals (around DOY 315) in Figure 5 almost vanish in the middle panel (B) of Figures 6-8. The deviation in the first interval (around DOY 50), on the other hand, does not seem to have improved in Figures 6-8. The amplitude of the annual temperature variation is around 10˚C for all three models. A flux enhancement just near the magnetic equator for L > 1.5 provides a better agreement for all three models.

4. Discussion

The results of the relative fluence estimated from the AP8MAX, AP9 mean and CRRESPRO quiet models are almost identical, as shown in Figure 5, which is rather remarkable. This is due to the equatorial orbit of the Arase satellite (Figure 3). Degradation of the solar cells of the polar orbiting Akebono satellite

was sensitive to the L-shell extent of energetic protons [5] [6], since the satellite integrated particle impact is roughly along the field lines. Therefore, the spatial extent for L-shell among the different models made a clear difference in estimating the degradation of the Akebono solar cells. On the other hand, the orbit of the Arase satellite crosses the field lines especially at low L-shell region where the proton radiation belts exist. This results in sensitivity for particle distribution along the field lines, which is clearly shown in the decreasing RMSE in **Figures 6-8**.

We assumed a steady state for the radiation environment in our study. However, there are reports on the temporal variation of proton radiation by the injection of solar energetic particles and magnetic storms cause the variation [15] [16]. The central part of the proton radiation belt ($L < 2.0$) is rather stable for most disturbances although two exceptional occasions are reported for extreme events [11] [17]. Our interval of analysis between December 2016 and March 2018 was fairly quiet with no large geomagnetic disturbances. The large events were in May and September 2017, where the Dst index reached only −125 and −142 nT, respectively.

Although we only had a few small geomagnetic disturbances, we did encounter an extreme SEP event in the interval of our analysis. The GOES satellite at GEO measured >10 MeV proton flux of 1208/cm^2 s/ster on September 11, 2017. The signature of a large flux of energetic protons can be seen as contamination in the particle detectors on board the Arase satellite. However, we did not see any abrupt change in the estimated Voc (**Figure 2**) or evaluated fluence (**Figure 4**) on that occasion (DOY = 251). Although quite a large flux of energetic protons certainly reached the Arase orbit, the injected energetic protons were not effectively trapped in the inner radiation belt for this event and the fluence was hardly affected. The associated magnetic disturbance seems to have been too small to trap the injected particles. Therefore, a steady state of the proton radiation belt can be a good approximation during the interval of our analysis.

We have so far assumed that trapped protons caused the degradation of solar cells of the Arase satellite. As discussed earlier, we found no evident effects attributable to solar protons. Trapped energetic electrons are another possible cause of the degradation of satellite solar cells. We made model calculations on the energetic electron fluence using the AE8 and AE9 models. We found that due to the outer belt, the variation in increasing relative fluence has an antiphase to that of the trapped protons during the analysis interval. Energetic electrons do not appear to be responsible for the alternating fast and slow periods of increasing relative fluence.

Trapped electrons in the outer belt are highly variable and the Arase satellite has detectors for energetic electrons. We took a quick look at the electron data of the HEP instrument [18] on board the Arase satellite. We found that the electron flux was high around April and October-November in 2017. The relative fluence from the SAP data in **Figures 5-8** (blue lines) shows that the increase was rather small in April (around DOY 100), which is consistent with the model

calculations (red lines) where only trapped protons are considered. In the September-October period (DOY 244-304), the model calculation for protons only (red line) gives an even faster increase in relative fluence compared to that deduced from the SAP data, so an additional contribution of large electron flux would make the deviation larger. Therefore, we conclude that energetic electrons do not significantly affect the particle fluence affecting the degradation of solar cells of the Arase satellite.

We conducted the analysis based on the spatial distribution of trapped protons with energies greater than 6.8 MeV for the CRRESPRO quiet model, and greater than 6.0 MeV for the AP8MAX and AP9 mean models. The range of flight for the cover glass only tells us that energetic protons with energies greater than 6 MeV can damage the solar cells. It is expected that effective damage by energetic protons peaks at around 8 MeV and decreases exponentially with energy. We also made a comparison with models of >8 MeV protons, and obtained almost identical results of the relative fluence for >6 MeV protons.

In this paper, we presented only the results for the case of equatorial proton flux 2.0 times that of the original models for L > 1.5. We have actually tried various modifications with larger/smaller enhancements and different approaches to flux variation along the field line. We found that any flux enhancement on the magnetic equator has the effect of improving the RMSE from that of the original models although the RMSE value varies from one model to another. A long-term variation of proton radiation belt was reported based on data from the Van Allen Probes [19]. Trapped proton flux of 19 MeV and 30 MeV with a pitch angle near 90˚ gradually increased around L = 1.6 to 2.0 from October 2013 to April 2017. Though the data were available only for energies larger than 17 MeV, trapped protons in this region are mainly of SEP origin and similar increase can be probable for >6 MeV protons. We tried steady temporal increase of proton flux just near the equator in our model, and found that any enhancement near the magnetic equator improves the RMSE from the original model. We are not looking further for the best-fitting model based on the minimum RMSE, but simply point out the effect of equatorial enhancement since the deviations appear to have sufficiently vanished from the middle panel (B) of **Figures 6-8**.

The deviation around DOY 50 between the relative fluence deduced from the SAP data and that from the model calculations persists for various models. One possibility to consider is that the satellite was still in the initial operation phase before March 2017. We should have removed data during sequences of special operation, but did not do so in this study. We leave the problem to future analysis. After the satellite shifted to regular operation, coincidence is evident in the middle panel (B) of **Figures 6-8**.

The observation of pitch-angle distribution from the Van Allen Probes suggested that high-energy protons around 26.0 MeV concentrate near the magnetic equator [2]. Particle measurement of the Van Allen Probes has a gap of proton energies between 1 and 17 MeV [3] and thus we cannot make a direct comparison with our results of >6.0 MeV protons. However, observation results of the

Van Allen Probes were obtained at 26.0, 46.0, and 66.0 MeV, and a greater concentration near the equator was found for lower energies. Radiation belt protons of SEP origin are expected to have lower energies and a greater concentration on the equator compared to those of cosmic ray albedo neutron decay (CRAND) origin. Therefore, protons with energies greater than 6.0 MeV are likely to concentrate near the magnetic equator. If we define 30% of the peak flux (broken line) as the outer limit of the equatorial concentration, the extent shown in the bottom panel (C) of **Figures 6-8** roughly corresponds to an equatorial pitch angle larger than about 60˚.

While there is a proton concentration near the magnetic equator, the 10% line of proton distribution extends along the field line off the equator in **Figures 6-8** (C). Trapped protons of CRAND origin are expected to be isotropic and widely spread along the field line. However, it should be noted that our results are significant only around the core portion of proton distribution, *i.e.*, near the flux peak. We analyzed the variation of increasing relative fluence deduced from the degradation of solar cells. The relative fluence mostly results in integration in a large flux region of the proton distribution. Our results are not sensitive to the extent of the low flux region such as low and/or high latitude regions. This point is quite different from the measurement of particle detectors with a wide (usually logarithmic) range of particle flux. Therefore, it would be misleading to draw low flux levels extending toward low and/or high latitude regions by using Equation (1). In this regard, the dotted line (10% of flux peak) in the bottom panel (C) of **Figures 6-8** is probably a fair limit of confidence.

Acknowledgements

We thank all the members of the Arase (ERG) project team for their extensive support.

Conflicts of Interest

The authors declare no conflicts of interest regarding the publication of this paper.

References

[1] Mauk, B.H., Fox, N.J., Kanekal, S.G., Kessel, R.L., Sibeck, D.G. and Ukhorskiy, A. (2013) Science Objectives and Rationale for the Radiation Belt Storm Probes Mission. *Space Science Reviews*, **179**, 3-27. https://doi.org/10.1007/s11214-012-9908-y

[2] Selesnick, R.S., Baker, D.N., Jaynes, A.N., Li, X., Kanekal, S.G., Hudson, M.K. and Kress, B.T. (2014) Observations of the Inner Radiation Belt: CRAND and Trapped Solar Protons. *Journal of Geophysical Research*, **119**, 6541-6552. https://doi.org/10.1002/2014JA020188

[3] Fennel, J.F., Blake, J.B., Claudepierre, S., Mazur, J., Kanekal, S., O'Brien, P., Baker, D., Crain, W., Mabry, D. and Clemmons, J. (2016) Current Energetic Particle Sensors. *Journal of Geophysical Research*: *Space Physics*, **121**, 8840-8858.

[4] Ishikawa, H., Miyake, W. and Matsuoka, A. (2013) Variation of Proton Radiation

Belt Deduced from Solar Cell Degradation of Akebono Satellite. *Earth Planets Space*, **65**, 121-125. https://doi.org/10.5047/eps.2012.06.004

[5] Miyake, W., Miyoshi, Y. and Matsuoka, A. (2014) On the Spatial Extent of the Proton Radiation Belt from Solar Cell Output Variation of the Akebono Satellite. *Advances in Space Research*, **53**, 1603-1609. https://doi.org/10.1016/j.asr.2014.03.002

[6] Miyake, W., Miyoshi, Y. and Matsuoka, A. (2015) An Empirical Modeling of Spatial Distribution of Trapped Protons from Solar Cell Degradation of the Akebono Satellite. *Advances in Space Research*, **56**, 2575-2581. https://doi.org/10.1016/j.asr.2015.10.021

[7] Miyoshi, Y., Shinohara, I., Takashima, T., Asamura, K., Higashio, N., Mitani, T., Kasahara, S., Yokota, S., Kazama, Y., Wang, S.-Y., Tam, S.W., Ho, P.T.P., Kasahara, Y., Kasaba, Y., Yagitani S., Matsuoka A., Kojima H., Katoh, H., Shiokawa, K. and Seki, K. (2018) Geospace Exploration Project ERG. *Earth Planets Space*, **70**, 101. https://doi.org/10.1186/s40623-018-0862-0

[8] Yokota, S., Kasahara, S., Mitani, T., Asamura, K, Hirahara, M., Takashima, T., Yamamoto, K. and Shibano, Y. (2017) Medium-Energy Particle Experiments-Ion Mass Analyzer (MEP-i) Onboard ERG (Arase). *Earth Planets Space*, **69**, 172. https://doi.org/10.1186/s40623-017-0754-8

[9] Knoll, G.F. (1989) Radiation Detection and Measurement. Wiley, New York.

[10] Ginet, G.P., O'Brien, T.P., Huston, S.L., Johnston, W.R., Guild, T.B., Friedel, R., Lindstrom, C.D., Roth, C.J., Whelan, P., Quinn, R.A., Madden, D., Morley, S. and Su, Y.-J. (2013) AE9, AP9 and SPM: New Models for Specifying the Trapped Energetic Particle and Space Plasma Environment. *Space Science Reviews*, **179**, 579-615. https://doi.org/10.1007/s11214-013-9964-y

[11] Gussenhoven, M.S., Mullen, E.G. and Brautigam, D.H. (1996) Improved Understanding of the Earth's Radiation Belts from the CRRES Satellite. *IEEE Transactions on Nuclear Science*, **43**, 353-368. https://doi.org/10.1109/23.490755

[12] Patel, M.R. (2005) Spacecraft Power Systems. Boca Raton, CRC Press.

[13] Kazama, Y. and Goka, G. (2008) A New Modeling Method of Solar Energetic Proton Events for ISO Specification. *Advances in Space Research*, **42**, 1293-1299. https://doi.org/10.1016/j.asr.2007.12.012

[14] Engel, M.A., Kress, B.T., Hudson, M.K. and Selesnick, R.S. (2016) Comparison of Van Allen Probes Radiation Belt Proton Data with Test Particle Simulation for the 17 March 2015 Storm. *Journal of Geophysical Research*: *Space Physics*, **121**, 11,035-11,041. https://doi.org/10.1002/2016JA023333

[15] Lorentzen, K.R., Mazur, J.E., Looper, M.D., Fennel, J.F. and Blake, J.B. (2002) Multisatellite Observations of MeV Ion Injections during Storms. *Journal of Geophysical Research*, **107**, 1231. https://doi.org/10.1029/2001JA000276

[16] Selesnick, R.S., Hudson, M.K. and Kress, B.T. (2010) Injection and Loss of Inner Radiation Belt Protons during Solar Proton Events and Magnetic Storms. *Journal of Geophysical Research*, **115**, Article ID: A08211. https://doi.org/10.1029/2010JA015247

[17] Looper, M.D., Blake, J.B. and Mewaldt, R.A. (2005) Response of the Inner Radiation Belt to the Violent Sun-Earth Connection Events of October-November 2003. *Geophysical Research Letters*, **32**, Article ID: L03S06. https://doi.org/10.1029/2004GL021502

[18] Mitani, T., Takashima, T., Kasahara, S., Miyake, W. and Hirahara, M. (2018) High-Energy Electron Experiment (HEP) Aboard the ERG (Arase) Spacecraft. *Earth Planet Space*, **70**, 77. https://doi.org/10.1186/s40623-018-0853-1

[19] Selesnick, R.S., Baker, D.N., Kanekal, S.G., Hoxie, V.C. and Li, X. (2018) Modeling the Proton Radiation Belt with Van Allen Probes Relativistic Electron-Proton Telescope Data. *Journal of Geophysical Research*, **123**, 685-697. https://doi.org/10.1002/2017JA024661

International Journal of Astronomy and Astrophysics, 2018, 8, 323-338
http://www.scirp.org/journal/ijaa
ISSN Online: 2161-4725
ISSN Print: 2161-4717

Structure of the Universe

Shihao Chen

Department of Physics, Northeast Normal University, Changchun, China
Email: shchen@nenu.edu.cn, Xuan.Chen@sanofi.com, baron@american.edu, mbaron@utdallas.edu

How to cite this paper: Chen, S.H. (2018) Structure of the Universe. *International Journal of Astronomy and Astrophysics*, **8**, 323-338.
https://doi.org/10.4236/ijaa.2018.84023

Received: August 8, 2018
Accepted: November 13, 2018
Published: November 16, 2018

Abstract

Based on a cosmological model without singularity, a possible structure of the universe is presented. It is proved that there must simultaneously be two sorts of symmetry breaking in the universe. The universe is composed of infinite s-cosmic islands, infinite v-cosmic islands and infinite transition zone. The existing and changing forms of the cosmic islands must be diverse. The cosmological principle holds only approximately within a cosmic island. No information can be exchanged between an s-cosmic island and an adjacent v-cosmic island so that every observer thinks his cosmic island to be the whole universe. It is possible that some cosmic islands are contracting, some cosmic islands are expanding, and other cosmic islands are stable for a time. But the universe as a whole is always invariable and contains all possible existing forms of matter. To give a possible explanation for orphan quasars. To predict some characteristics of contracting large and huge black holes in a cosmic island. The characteristics of the light coming from the contracting huge black holes are that the intensity of the light is huge relatively to their distance, the red shifts are huge, the distribution of the huge red shifts and the orphan quasars are anisotropic, and luminescence spectrum is very wide.

Keywords

Cosmic Island, Quasars, Anisotropy of Huge Red Shifts, $SU(5)$ Colour Singlets, Singularity

1. Introduction

The Ref. [1] has presented a cosmological model without singularity based on R-W metric. According to [1], there are two sorts of matter which are called s-matter and v-matter, respectively. The masses of the s-matter and the v-matter are all positive, but both gravitation masses are contrary to each other. S-elementary particles and v-elementary particles are perfectly symmetrical and are described by the symmetric groups $SU_S(5)$ and $SU_V(5)$, respectively.

There are two sorts of Higgs fields which are called the s-Higgs fields and the v-Higgs fields, respectively. Both are perfectly symmetrical. and there is the coupling of s-Higgs field Ω_S and v-Higgs field Ω_V. Both Ω_S and Ω_V are real fields with simple component. There are two sorts of symmetry breaking which are s-breaking and v-breaking, respectively. In the s-breaking $\langle\Omega_S\rangle = \langle\Omega\rangle_0$ and $\langle\Omega_V\rangle = 0$, and in the v-breaking $\langle\Omega_V\rangle = \langle\Omega\rangle_0$, and $\langle\Omega_S\rangle = 0$.

When $SU_S(5)$ or $SU_V(5)$ is not broken, *i.e.*, $\langle\Omega_S\rangle = 0$ or $\langle\Omega_V\rangle = 0$, the proper masses of all s-elementary particles or all v-elementary particles are zero. Consequently, all s-elementary particles or all v-elementary particles must combine into $SU_S(5)$ or $SU_V(5)$ colour singlets. This is similar to quarks or gluons to form hadrons and mesons.

There is no singularity and there is the highest temperature $T_{\max}$ or the highest energy density $\rho_{\max}$ according to the model. The evolution of the universe has been explained [1] when the cosmological principle holds in whole universe, and the problem of the cosmological constant can be solved. Some new predictions are given [1]. A definition of the locally conservative energy-momentum tensor is given based on this model [2].

In present paper we discuss the possibility that the universe is composed of infinite cosmic islands. The cosmological principle holds approximately in a cosmic island.

This idea of multiverse or parallel universes has been proposed for a long time, such as Ref. [3]. There still are some fundamental problems of cosmology, such as singularity and cosmological constant problems, in the concept of multiverse or parallel universes. This is essentially different from the model [1].

In Section 2 it is proved that there simultaneously are two sorts of symmetry breaking in the universe; In Section 3 evolution of a huge s-black hole inside an s-cosmic island and some predictions are discussed; In Section 4 the structure of the universe is discussed; In Section 5 to give a possible explanation to the orphan quasars and some predictions; The Section 6 is the conclusions.

2. There Simultaneously Are Two Sorts of Symmetry Breaking in the Universe

2.1. The Possibility That There Simultaneously Are the Two Sorts of Symmetry Breaking

Here and below Ω_S and Ω_V are taken as an example to illustrate the change of the expectation values of Higgs fields in [1]. On the other hand, the expectation values of other Higgs fields can be determined when $\langle\Omega_S\rangle$ and $\langle\Omega_V\rangle$ are determined [1]. According to [1], there are the $SU_S(5)$ symmetry s-breaking or the $SU_V(5)$ symmetry v-breaking. It is necessary that there is the transition zone between a s-region and a v-region To consider a spherically symmetric region with its radius r_O in a flat space. In the case, $\mathrm{d}s = R(t)\mathrm{d}r \equiv \mathrm{d}\tilde{r}$ in the radial at a time t, here $R(t)$ is the scale factor in the RW metric. We suppose that there is the following symmetry breaking

$$\langle\Omega_V\rangle=\langle\Omega\rangle_0,\ \langle\Omega_S\rangle=0,\ \text{when } r\geq r_O \tag{1}$$

$$\langle\Omega_S\rangle=\langle\Omega\rangle_0,\ \langle\Omega_V\rangle=0,\ \text{when } r\leq r_I, r_I<r_O, \tag{2}$$

$$\langle\Omega_S\rangle=\frac{1}{2}\langle\Omega\rangle_0\left[\cos\tilde{k}\left(\tilde{r}-\tilde{r}_I\right)+1\right],\ \tilde{k}=k/R=\pi/R\left(r_O-r_I\right),\ \text{when } r_I<r<r_O, \tag{3}$$

$$\langle\Omega_V\rangle=\frac{1}{2}\langle\Omega\rangle_0\left[-\cos\tilde{k}\left(\tilde{r}-\tilde{r}_I\right)+1\right],\ \text{when } r_I<r<r_O, \tag{4}$$

when

$$T_S=T_V=0 \tag{5}$$

The zones where $r\leq r_I$, $r_I<r<r_O$ and $r\geq r_O$ are called I-zone, T-zone and O-zone, respectively. We call such a region with the boundary conditions (1)-(2) an s-cosmic island, and such a region with the boundary conditions (1)-(2) in which the subscripts *s* and *v* exchange, *i.e.*, $s\rightleftarrows v$, a v-cosmic island.

Another choice of symmetry breaking easily to calculate is

$$\langle\Omega_V\rangle=\langle\Omega\rangle_0,\ \langle\Omega_S\rangle=0,\ \text{when } r\geq r_O \tag{1'}$$

$$\langle\Omega_S\rangle=\langle\Omega\rangle_0,\ \langle\Omega_V\rangle=0,\ \text{when } r\leq r_I, r_I<r_O, \tag{2'}$$

$$\langle\Omega_S\rangle=\frac{1}{2}\langle\Omega\rangle_0\left[\cos\tilde{k}\left(\tilde{r}-\tilde{r}_I\right)+1\right],\ \tilde{k}=k/R=\pi/R\left(r_O-r_M\right),\ \text{when } r_I<r<r_M, \tag{3'}$$

$$\langle\Omega_V\rangle=\frac{1}{2}\langle\Omega\rangle_0\left[-\cos\tilde{k}\left(\tilde{r}-\tilde{r}_I\right)+1\right],\ \text{when } r_M<r<r_O, \tag{4'}$$

when

$$T_S=T_V=0. \tag{5'}$$

We will discuss the case in another paper.

In the below discussion the coordinate *r* and the O-zone are regarded as invariant. We discuss evolution of an s-cosmic island. It is obvious that the results are true for a v-cosmic island as well.

It is easily seen from [1] that the expectation values of other Higgs fields and the masses of particles can be determined from (1) and (2). In the I-zone, s-elementary particles get their respective proper masses, are colourless due to $\langle\Omega_S\rangle=\langle\Omega\rangle_0$ and can form s-atoms, s-molecules and s-celestial bodies, but all v-elementary particles are massless, must possess some a sort of $SU_V(5)$ colours so that they must form $SU_V(5)$ colour singlets whose masses are not zero. There is no interaction of long range except gravitation among the $SU_V(5)$ colour singlets so that they can only diffusely distribute in the I-zone. Analogously, in the O-zone, v-elementary particles get their respective proper masses, are colourless due to $\langle\Omega_V\rangle=\langle\Omega\rangle_0$, and can form v-atoms, v-molecules and v-celestial bodies, but all s-elementary particles are massless, possess some a sort of $SU_S(5)$ colours and must form $SU_S(5)$ colour singlets. There is no interaction of long range except gravitation among the $SU_S(5)$ colour singlets so that they can only diffusely distribute in the O-zone. In the T-zone $\langle\Omega_S\rangle\neq 0$ and $\langle\Omega_V\rangle\neq 0$, but the breaking form of the $SU_S(5)$ group is the same as that

in the I-zone, and the breaking form of the $SU_V(5)$ group is the same as that in the O-zone. Consequently, the s-elementary particles and the v-elementary particles get all their respective proper masses. But the masses change as $\langle\Omega_S\rangle$ or $\langle\Omega_V\rangle$ continuously change. The mass m_{Sn} changes from m_{Sn0} to 0 and the mass m_{Vn} changes from 0 to m_{Vn0}, here m_{Sn} and m_{Sn0} are the masses of s-elementary particle S_n in the T-zone and in the I-zone, respectively; and m_{Vn} and m_{Vn0} are the masses of the v-elementary particle V_n in the T-zone and in the O-zone, respectively. Consequently, the elementary particles cannot form stable bound states similar to atoms or molecules because their masses change at any moment, and there is no $SU(5)$ colour singlet, because $\langle\Omega_S\rangle \neq 0$ and $\langle\Omega_V\rangle \neq 0$. The masses of the $SU(5)$ gauge particles are not zero in the T-zone. However, it is possible that the particles form bound states similar to colour singlets for a shorter time which are called quasi colour singlets.

We compute the Higgs potential energy V in the spherically symmetric T-zone. Although the calculation result is not very accurate, but V to be finite is qualitatively correct. It is easily seen from [1] that when $T_S = T_V = 0$, $\langle\Omega_S\rangle = \langle\Omega\rangle_0 = \sqrt{\mu^2/\lambda}$ and $\langle\Omega_V\rangle = 0$ or $\langle\Omega_V\rangle = \langle\Omega\rangle_0$ and $\langle\Omega_S\rangle = 0$

$$U_{\min} = -\frac{1}{2}\mu^2\langle\Omega\rangle_0^2 + \frac{1}{4}\lambda\langle\Omega\rangle_0^4 = -\frac{\mu^4}{4\lambda}. \tag{6}$$

It is obvious that the Higgs potential energy exists only in the T-zone. Considering (5)-(6) and let $\bar{\Omega} \equiv \langle\Omega\rangle$, we get

$$\begin{aligned} V = 4\pi\int_{\tilde{r}_I}^{\tilde{r}_O} \mathrm{d}\tilde{r}\cdot\tilde{r}^2 \Bigg\{ &\left[\frac{1}{2}\left(\partial_{\tilde{r}}\bar{\Omega}_S\right)^2 - \frac{1}{2}\mu^2\bar{\Omega}_S^2 + \frac{1}{4}\lambda\bar{\Omega}_S^4\right] \\ &+ \left[\frac{1}{2}\left(\partial_{\tilde{r}}\bar{\Omega}_V\right)^2 - \frac{1}{2}\mu^2\bar{\Omega}_V^2 + \frac{1}{4}\lambda\bar{\Omega}_V^4\right] + \frac{1}{2}\Lambda\bar{\Omega}_S^2\bar{\Omega}_V^2 - U_{\min}\Bigg\}. \end{aligned} \tag{7}$$

Substituting (1) - (6) into (7), we obtain

$$\begin{aligned} V = 4\pi\int_{\tilde{r}_I}^{\tilde{r}_O} \mathrm{d}\tilde{r}\cdot\tilde{r}^2 \Bigg\{ &\frac{\langle\Omega\rangle_0^2}{8}k^2(1-\cos\theta) - \frac{\langle\Omega\rangle_0^2}{8}\mu^2(3+\cos 2\theta) \\ &+ \frac{\lambda\bar{\Omega}_0^4}{64}\left[\frac{35}{4} + 7\cos 2\theta + \frac{1}{4}\cos 4\theta\right] \\ &+ \frac{\Lambda\bar{\Omega}_0^4}{64}\left[\frac{3}{4} - \cos 2\theta + \frac{1}{4}\cos 4\theta\right] - U_{\min}\Bigg\}, \quad \theta \equiv \tilde{k}\left(\tilde{r} - \tilde{r}_I\right). \end{aligned} \tag{8}$$

Substituting $\langle\Omega\rangle_0^2 = \mu^2/\lambda$ and (6) into (7) and let $R(r_O - r_I) \equiv a$, we get

$$V = \frac{\pi\mu^2}{2\lambda}\left\{\frac{\pi^2}{a}(Rr_I)^2 + \pi^2(Rr_I) + Aa + Ba^2 + Ca^3\right\}, \tag{9a}$$

$$A = \left(\frac{\pi^2}{3} - \frac{1}{2}\right) + \frac{3}{32}\mu^2(Rr_I)^2\left(1 + \frac{\Lambda}{\lambda}\right), \tag{9b}$$

$$B = \frac{3}{32}\mu^2(Rr_I)\left(1 + \frac{\Lambda}{\lambda}\right), \tag{9c}$$

$$C=\frac{1}{32}\mu^2\left[\left(1-\frac{5}{8\pi^2}\right)+\left(1-\frac{15}{8\pi^2}\right)\frac{\Lambda}{\lambda}\right]. \tag{9d}$$

We regard a as the variational parameter and $\tilde{r}_I = Rr_I$ as invariant for a time. From

$$\frac{\partial V}{\partial a}=0 \text{ at } a=a_0=a_0\left(Rr_I,\mu,\Lambda,\lambda\right)=a_0\left(\tilde{r}_I\right), \tag{10}$$

we get the minimun $V_{\min}$ for some a definite $\tilde{r}_I = Rr_I$. The pressure F_T of the T-zone on the I-zone and the intensity of the pressure corresponding to F_T are respectively

$$V_{\min}=V\left(Rr_I,a_0\right), \tag{11}$$

$$F_T=-\frac{\partial V_{\min}}{\partial \tilde{r}_I},\ P_T=\frac{F_T}{4\pi\tilde{r}_I^2}. \tag{12}$$

$V_{\min}\left(\tilde{r}_I,a_0\right)$ must be finite for a certain finite value of R_I. This is important, because the T-zone can exist so long as $V_{\min}\left(\tilde{r}_I,a_0\right)$ is finite, It is easily seen from (9) - (11) that

$$a_0\approx\frac{\pi}{\mu}\left(\frac{32}{3\left(1+\Lambda/\lambda\right)}\right)^{1/2}, \tag{13}$$

a_0 is approximately independent of R when $\tilde{r}_I$ is large.

Taking a rough approximation of P_T that a_0 is regarded to be independent of $\tilde{r}_I$, we get

$$P_T=\frac{F_T}{4\pi\tilde{r}_I^2}=-\frac{\mu^2}{4\lambda}\left[\pi^2+\frac{3}{32}\left(1+\frac{\Lambda}{\lambda}\right)a_0^2\mu^2\right]\left[\frac{1}{a_0\tilde{r}_I}+\frac{1}{2\tilde{r}_I^2}\right]. \tag{14}$$

The energy-momentum tensor of ideal gas is

$$T_{\mu\nu}=\left(\rho+p\right)u_\mu u_\nu-g_{\mu\nu}p,$$

where ρ and p are the gravitational mass density and the intensity of pressure of the gas. In order to consider the effect of P_T on the evolution of the s-cosmic island, we suppose that there is a effective ideal gas with $T_{\mu\nu}$ and $u_\mu=u_\nu=0$ corresponding to P_T and

$$P_T=w\rho_T=-\rho_T. \tag{15}$$

Consequently, the Friedmann equations become [1]

$$\left(\dot{R}\right)^2+k=\eta\left(\rho_S-\rho_V-P_T+V_{SI}\right)R^2=\eta\rho_g R^2, \tag{16}$$

$$\ddot{R}=-\frac{\eta}{2}\left[\left(\rho_S-\rho_V\right)+3\left(p_S-p_V\right)+2P_T-2V_{SI}\right]R=-\frac{\eta}{2}\left(\rho_g+3p_g\right)R, \tag{17}$$

where $\eta=8\pi G/3$, $k=0$ is taken, ρ_g is the gravitational mass density, $p_g=\left(p_S-p_V\right)+P_T-V_{SI}$, and V_{SI} is the s-Higgs potential energy in the I-zone. $V_{SI}=0$ when the temperature $T_S\approx 0$, and $V_{SI}=V_0$ **when** $T_S\gtrsim T_{\max}$ inside the I-zone. (16)-(17) hold only when $r<r_I$. Another choice different from (15) is $w\to\infty$, *i.e.*, $\rho_T=0$. We will discuss it in another paper.

Here only the effect of the intensity of pressure P_T is considered. The reasons are as follows.

A. The potential energy $V_{\min}$ in the T-zone is the Higgs potential energy, and no gravitational potential energy coming from gravitational masses.

B. Let V_{gT}, V_{ST} and V_{VT} be the gravitational potential energy, s-Higgs potential energy and the v-Higgs potential energy in the T-zone, respectively, then $V_{gT} \equiv V_{ST} - V_{VT} \approx 0$ because the gravitational masses of V_{ST} and V_{VT} are opposite from each other and $V_{ST} \approx V_{VT}$ in the T-zone.

C. No contribution of the total Higgs potential energy $V_{\min}$ in (11) to the Einstein tensor $G_{\mu\nu} = R_{\mu\nu} - (1/2) g_{\mu\nu} R$ inside the I-zone, because the T-zone is spherical symmetric.

It is seen that only the effect of P_T should be considered.

It is obvious that $V_{\min} = 0$ when $R_I \to 0$ and $a_0 \to 0$. This implies the T-zone will contract and it cannot exist. But, in fact, it is possible that the T-zone exists when the energy density ρ_V of the $SU_V(5)$ colour singlets and the energy density ρ_S of the s-particles in the I-zone are large enough. The reasons are as follows.

1) In the T-zone, the expectation values of the s-Higgs fields and the v-Higgs fields are different from those in the I-zone and the O-zone. But the breaking forms of these Higgs fields do not change. Hence the s-photons and v-photons in the T-zone are still massless. The s-photons are not the colour singles in the O-zone. The v-photons are not the colour singles in the I-zone as well. Consequently, when the s-photons pass the T-zone and arrive the O-zone, they cannot enter the O-zone and will be reflected back unless they and other s-particles combine to form $SU_S(5)$ quasi colour singlets for a shorter time. The same is true for the v-photons which arrive the I-zone from the O-zone. The s-photons reflected back to the I-zone resist the contraction of the T-zone. Analogously, the v-photons reflected back to the O-zone resist the expansion of the T-zone.

2) If a v-elementary particle E_V enters into the T-zone from the I-zone, it will get its proper mass m_{VE}, and m_{VE} will increase as $\langle \Omega_V \rangle$ continuously increases. Consequently, if a $SU_V(5)$ colour singlet S_V enters into the T-zone from the I-zone, S_V must suffer resistance coming from the T-zone due to its mass to increase**.** When the colour singlet S_V enters the T-zone, S_V is no longer a colour singlet and possibly splits into several v-elementary particles composing it, such as E_V and E_V^C. The changes of m_{VE} are realized by the interactions of E_V and the v-Higgs fields via exchanging virtual Higgs particles or by the interactions of E_V and other v-particles. The increasing of the mass m_{VE} from 0 to m_{VE0} needs multiple such interactions, here m_{VE0} is the mass of E_V when E_V is in the O-zone. Consequently, the probability of S_V or E_V^C to pass the T-zone and to enter the O-zone must be very small. On the other hand, if S_V gets its mass m_{VC0}, S_V as a whole can enter to the O-zone, here m_{VC0} is the mass of S_V when S_V is in the O-zone. It is obvious

that the probability must be smaller. It is seen that when E_V, E_V^C or S_V passes the T-zone and enters into the O-zone from the I-zone, it must suffer resistance coming from the T-zone due to the masses to increase

If S_V does not enter the O-zone, it will return to the I-zone. If E_V and E_V^C do not enter the O-zone, they will combine into a quasi $SU_V(5)$ colour singlet and returns to the I-zone. The v-particles to return to the I-zone resist the contraction of the T-zone. This implies that contraction of the T-zone (R_I reduces) must suffer a repulsing force coming from the $V-SU_V(5)$ colour singlets. It is seen from the above described that when the density of the $SU_V(5)$ colour singlets is large enough, the contraction of the T-zone can be prevented. The v-particles entering into the O-zone will mix with the original v-particles in the O-zone and cannot be distinguished. The T-zone seems to be the membrane of a balloon and the $SU_V(5)$ colour singlets in the I-zone seem to be gas in the balloon.

3) It is possible that a s-particle E_S with its proper mass m_{ES} enters into the T-zone from the I-zone. When it enters the T-zone, its mass m_{ES} will decrease as $\langle\Omega_S\rangle$ continuously decreases. But E_S is not a $SU_S(5)$ colour singlet, hence it cannot pass the T-zone to enter the O-zone unless E_S and other s-particles, such as E_S^C, combine to form a $SU_S(5)$ quasi colour singlet. But the probability must be very small, because there is no interaction with long range among the s-particles except the gravitation due to $\langle\Omega_S\rangle\neq 0$ in the T-zone. When E_S does not enter the O-zone, it will return back to the I-zone provided its mass renewedly increase to m_{ES0}, m_{ES0} is the mass when E_S is in the I-zone. The s-particles returning back to the I-zone resist the contraction of the T-zone. The $SU_S(5)$ quasi colour singlets can enter the O-zone. After they enter into the O-zone, they become the corresponding $SU_S(5)$ colour singlets, *i.e.*, dark energy particles which cannot be observed by observers in the O-zone.

4) When $\dot{R}\neq 0$, ρ_s and ρ_V will change, hence the intensity of pressure of the I-zone on the T-zone will change.

Let $P_{SI}=p_S$ and $P_{VI}=p_V$ be the intensities of the pressure of the s-particles and the v-colour singlets inside I-zone on the T-zone, respectively, and β_{SI} and β_{VI} be the probabilities of the s-particles and the v-colour singlets inside the I-zone to penetrate the T-zone, respectively, based on the discussion above, the intensity of the pressure of the particles in the I-zone on the T-zone is

$$P_I=(1-\beta_{SI})P_{SI}+(1-\beta_{VI})P_{VI}+(\zeta_{SI}\rho_S+\zeta_{VI}\rho_V)\dot{R}=-P_T. \tag{18}$$

P_I is regarded as the intensity of the counter pressure of P_T.

The discussions above are true as well for the process in which the $SU_S(5)$ colour singlets and the v-particles in the O-zone pass the T-zone and enter the I-zone. We do not consider the intensity of pressure of the O-zone on the T-zone for a time**,** because what directly affects the evolution of the I-none are P_T and $\tilde{r}_I$.

2.2. The Relationship of the Higgs Potential Energy and Temperature

The relationship of the Higgs potential energy and temperature is similar to that in (5.2) of [1], *i.e.*,

$$\begin{aligned} V_{eff}^{(1)T} &= \left[-\frac{1}{2}\left(\mu^2-\frac{\lambda}{4}T_S^2\right)\bar{\Omega}_S^2+\frac{\lambda}{4}\bar{\Omega}_S^4-\frac{\pi^2}{90}T_S^4+\frac{\mu^2}{24}T_S^2\right] \\ &+\left[-\frac{1}{2}\left(\mu^2-\frac{\lambda}{4}T_V^2\right)\bar{\Omega}_V^2+\frac{\lambda}{4}\bar{\Omega}_V^4-\frac{\pi^2}{90}T_V^4+\frac{\mu^2}{24}T_V^2\right] \\ &+\frac{1}{2}\Lambda\bar{\Omega}_S^2\bar{\Omega}_V^2-U_{\min}. \end{aligned} \tag{19}$$

When $T_S \sim T_V \simeq T_{\max}$, inflation will occur. The inflation process is a supercooled process. After inflation, reheating process will occur. If $T_S < T_V$, s-breaking occurs; If $T_S > T_V$, v-breaking occurs.

3. Evolution of a Cosmic Island

Let $P_{T\max}$ be the maximum intensity of pressure of the T-zone of an s-cosmic island in contracting process. We classify s-cosmic islands into three classes. The first class is called huge cosmic islands $C_S^{(1)}$ whose $P_{T\max} < V_0$; the second class is called large cosmic islands $C_S^{(2)}$ whose $P_{T\max} \lesssim V_0$, and the third class is called small cosmic islands $C_S^{(3)}$ whose $P_{T\max} > V_0$.

Evolution of the s-cosmic islands is determined by (16)-(17) and (14).

A. Evolution of an s-cosmic island in which there is inflation process.

Let there be a huge s-cosmic island $C_S^{(1)}$. At t_{-2} $\rho_g > 0$, $p_g > 0$, $V_{SI} = 0$ and $C_S^{(1)}$ is contracting., The temperature T_S inside the I-zone of $C_S^{(1)}$ must rise due to contraction. Let $T_S = T_{\max}$ at t_{-1}. In the case, $\langle\Omega_S\rangle = 0$ in the I-zone, the T-zone and the O-zone; $\langle\Omega_V\rangle = 0$ in the I-zone, $\langle\Omega_V\rangle$ is described by (4) in the T-zone and $\langle\Omega_V\rangle = \langle\Omega\rangle_0$ in the O-zone; the masses of all elementary s-particles and v-particles inside the I-zone are zero, the s-elementary particles and the v-elementary particles can transform to each other so that $T_V = T_S = T_{\max}$, $V_{SI} = V_0$, $\rho_g = -P_T\left(R\left(t_{-1}\right)r_I\right)+V_0 > 0$, $\ddot{R}/R = -\eta\left(P_T\left(R\left(t_{-1}\right)r_I\right)-V_0\right) > 0$, and $C_S^{(1)}$ continues to contract with a deceleration. The s-elementary particles will form s-colour singlets $S_S's$, and the elementary v-particles will form v-colour singlets $S_V's$. S_S can freely escape out $C_S^{(1)}$ because of $\langle\Omega_S\rangle = 0$ in every zone. But S_V cannot easily escape out $C_S^{(1)}$ because of $\langle\Omega_V\rangle \neq 0$ in the T-zone. and the O-zone. Consequently, it is necessary that $\rho_V > \rho_S$ and there is such a time t_0 at which

$$\rho_g\left(t_0\right) = \rho_S\left(t_0\right) - \rho_V\left(t_0\right) - P_T\left(t_0\right) + V_0 = 0, \tag{20}$$

$$\begin{aligned} -\left(\rho_g\left(t_0\right)+3p_g\left(t_0\right)\right) &= -3\left[\left(p_S\left(t_0\right)-p_V\left(t_0\right)\right)+P_T\left(t_0\right)-V_0\right] \\ &= -4\left(P_T\left(t_0\right)-V_0\right) > 0. \end{aligned} \tag{21}$$

This is because $\rho_S \sim R^{-4}$, $\rho_V \sim R^{-4}$, $P_T \sim R^{-2}$, $\rho_S < \rho_V$, $p_S \sim \rho_S/3$ and

$p_V \sim \rho_V/3$ when R. is small. Thus, $\dot{R}=0$, $\ddot{R}>0$ and there must be $R>0$, *i.e.*, there is no singularity. It is obvious that $P_T(t_0)=P_{T\max}$. $P_{T\max}<V_0$ is the condition of inflation and the physical significance of "large enough s-cosmic island". We call $P_T(t_0)=P_{T\max}$ the largest T-intensity of pressure.

It should be noted that when the symmetry $SU_S(5)\times SU_V(5)$ holds, *i.e.*, $\langle\Omega_S\rangle=\langle\Omega_V\rangle=0$, the evolution equations are no longer those in the s-breaking, *i.e.*, ρ_g is no longer $(\rho_S-\rho_V-P_T+V_0)$. The evolution equations can only be determined based on the principle $(\dot{R}/R)^2=\eta\rho_g\geq 0$. As described above, $\rho_S<\rho_V$ when $\rho_g=0$. On the other hand, the effects of P_T and V_0 are the same for the s-breaking and the v-breaking. Consequently, we determine the evolution equations are

$$\left(\dot{R}\right)^2=\eta\left(\rho_V-\rho_S-P_T+V_0\right)R^2=\eta\rho_g R^2, \tag{22}$$

$$\ddot{R}=-\frac{\eta}{2}\left[\left(\rho_V-\rho_S\right)+3\left(p_V-p_S\right)+2P_T-2V_0\right]R \tag{23}$$

It is seen from (22)-(23) that $C_S^{(1)}$ begin expands with a acceleration when $t>t_0$. There is such a time t_F due to $C_S^{(1)}$ to be large enough at which $\rho_V(t_F)-\rho_S(t_F)-P_T(t_F)=0$ because $\rho_S\sim R^{-4}$, $\rho_V\sim R^{-4}$ and $P_T\sim R^{-1}$ when R increases. In the case, $\ddot{R}(t_F)>0$ and inflation occurs,

$$\dot{R}/R=\sqrt{\eta V_0},\ R(t)=R(t_F)\exp\sqrt{\eta V_0}\,(t-t_F). \tag{24}$$

The energy scale of the $SU(5)$ grant unified theory is 10^{15} GeV and $V_0\sim T_{\max}^4=10^{60}$ GeV^4. Taking $(t_H-t_F)=10^{-33}$ s, we obtain $R=10^{43}R(t_F)$. This is consistent with the traditional theory. After inflation, temperature T_S and T_V significantly drop so that $T_S<2\mu/\sqrt{\lambda}$, and $T_S<T_V$ because S_S can freely escape out $C_S^{(1)}$ and S_V cannot easily escape out $C_S^{(1)}$ in the period t_H-t_0. But for $C_S^{(1)}$, the main factor of T_S and T_V to reduce is inflation, not the s-particles to escape, because the period t_H-t_0 is very short. This is a supercooling process.

When $t=t_H$, $\langle\Omega_S\rangle=0\Rightarrow\langle\Omega_S\rangle=\langle\Omega\rangle_0$ and $V_{SI}=V_0\Rightarrow V_{SI}=0$ occurs, but $\langle\Omega_V\rangle=0$ still holds. The Higgs potential energy V_0 transforms into the energies of s-particles and v-colour singlets and the energy of the T-zone. Thus, T_S and T_V anew rise. This is so-called reheating process. It is easily seen that after inflation, $C_S^{(1)}$ is still an s-cosmic island.

After the reheating process, $C_S^{(1)}$ will continue to expand and the evolution equations of $C_S^{(1)}$ is still (16)-(17) but in which $V_{SI}=0$ and $k=0$, the s-particles will form s-atoms, s-molecules and s-celestial bodies and $\rho_S\sim R^{-3}$ and $p_S\sim 0$, and the v-particles will form v-colour singlets and $\rho_V\sim R^{-4}$ and $p_V\sim\rho_V/3$. Thus, it is possible that in some a period

$$\dot{R}/R>0,\ \ddot{R}/R=-\frac{\eta}{2}\left[\rho_S-\rho_V-3p_V+2P_T\right]>0, \tag{25}$$

i.e., $C_S^{(1)}$ will expand with an acceleration. A detailed calculation is similar to that of [1]. It it obvious that there must be such a time t_U at which

$$\left(\dot{R}(t_U)\right)^2 = \eta\left(\rho_S(t_U) - \rho_V(t_U) - P_T(t_U)\right)R^2 = 0, \tag{26}$$

so long as $(t_U - t_H)$ is large enough, because $\rho_S \sim R^{-3}$, $\rho_V \sim R^{-4}$ and $P_T \sim R^{-1}$ when R is large. It is easily seen that

$$\ddot{R}(t_U) = -\frac{\eta}{2}\left[-3p_V(t_U) + 3P_T(t_U)\right]R(t_U) < 0. \tag{27}$$

Thus, after expansion and expansion with an acceleration, $C_S^{(1)}$ will stop to expand and begin to contract.

B. Evolution of an s-cosmic island in which there is no inflation process.

Let a large s-cosmic island $C_S^{(2)}$ with its largest T-intensity of pressure $P_T(t_0) = P_{T\max} \lesssim V_0$. In the case, when $T_S = T_{\max}$ and

$$\rho_g = \rho_S - \rho_V - P_T + V_0 = 0, \tag{28}$$

$$\ddot{R} = -2\eta\left(P_T - V_0\right)R \gtrsim 0, \tag{29}$$

Thus, when $t > t_0$, $C_S^{(2)}$ will expand.

When the temperature T_S inside the I-zone arrives $T_{\max}$, there are two ways of T_S to drop. The first way is R increases as described above. The second way is that R will slowly increase due to (28)-(29) and a lot of the s-colour singlets escape out the I-zone when $t > t_0$, so that T_S drops to T_{SO}, here T_{SO} is the temperature of the s-colour singlets outside the T-zone. Consequently, the s-breaking occurs, $\langle\Omega_S\rangle = 0 \to \langle\Omega_S\rangle = \langle\Omega\rangle_0$, *i.e.*, the reheating process occurs so that inflation cannot occur. In the case, it is seen from (22)-(23) that if $\rho_g = V_0$, $\ddot{R}/R = -\eta\left[2P_T - V_0\right] < 0$. Hence the condition $\rho_g = V_0$ of inflation cannot be realized when $t > t_0$. The evolution process after reheating process is similar to those of inflation. The main difference is that the scale factor R is smaller in the reheating time in the process than that in the inflation process.

In the processes above, when R increases, some energies of s-particles and v-colour singlets transform into the Higgs potential energy in the T-zone; when R decreases, a part of the energy of the Higgs potential energy in the T-zone transforms into the energies of s-particles and v-colour singlets.

It is easily seen that the I-zone of $C_S^{(1)}$ and the I-zone of $C_S^{(2)}$ are all uniform and flat. A observer outside $C_S^{(1)}$ or $C_S^{(2)}$ will detect v-particles to continuously emit out.

C. Disappearing of a small s-cosmic island

Let an s-cosmic island $C_S^{(3)}$ be so small that its largest T-intensity of pressure $P_T(t_0) = P_{T\max} > V_0$, when $\rho_g = \rho_S - \rho_V - P_T + V_0 = 0$. In the case,

$$\ddot{R} = -2\eta\left(P_T - V_0\right)R \leq 0, \tag{30}$$

$C_S^{(3)}$ will continue to contract, and the evolution equations are (22)-(23). The Higgs potential energy V_0 continuously transforms to the energies of s-particles and v-particles, and ρ_S and ρ_V continue reduce until $\rho_S \sim \rho_V \sim 0$. Finally, all Higgs potential energy of the T-zone transforms the energies of s-particles and v-particles so that the T-zone and $C_S^{(3)}$ disappear.

A v-observer outside $C_S^{(3)}$ will detect a lot of v-particles to erupt in a very

short period. This indicates that the lifespan of a small cosmic island is very short and very small cosmic island cannot exist.

Particles inside an s-cosmic island can escape out, and some particles can enter into the s-cosmic island. But total effect is that the s-cosmic island continuously decrease its energy. Thus, when $C_S^{(2)}$ again contracts, it will become $C_S^{(3)}$ to disappear. It is seen that the lifespan of such an s-cosmic island with its $P_T(t_0) = P_{T\max} \sim V_0$ will be short.

4. Evolution of a Huge S-Black Hole Inside an S-Cosmic Island and Some Predictions

4.1. Evolution of a Huge S-Black Hole Inside an S-Cosmic Island

We classify s-black holes into two classes. The first class of black holes is such black holes which can contract and the temperatures inside them can arrive $T_{\max}$. The first class of black holes is divided into two sorts $B_S^{(2)}$ and $B_S^{(3)}$ which are corresponding to the two classes of s-cosmic islands $C_S^{(2)}$ and $C_S^{(3)}$. The second class of black holes is the ordinary black holes which cannot contract and the temperatures inside them cannot arrive $T_{\max}$. It is obvious that the mass and density of a first class black hole must be huger than those of a second class black hole. Evolution of a first class black hole is discussed as follows.

Let there be a spherically symmetric s-black hole $B_S^{(i)}$, $i = 2$ and 3, in the s-cosmic island $C_S^{(1)}$ whose total mass M_S and density $\rho_s(t)$ are all large enough. There is no v-particle inside $B_S^{(i)}$ because its repulsion on the v-particles. Thus, $B_S^{(i)}$ must contract due to its gravitation and its temperature T_S must rise. When T_S is high enough, such as $T_S \geq 1\,\text{MeV}$, $\rho_S = g^* T_S^4$ and $P_S = \rho_S/3$, the corresponding Friedmann equations are

$$\dot{R}^2 + k = \eta\rho_S R^2, \quad \ddot{R} = -(\eta/2)(\rho_S + 3P_S). \tag{31}$$

$$\rho_S R^4 = \sigma T_S^4 R^4 = const \cdot \sigma = (\pi^2/30) g^*, \dot{R}/R = -\dot{T}_S/T_S, \tag{32}$$

where g^* is the total degrees of spin freedom. Taking $k = 0$ and considering $\rho_s = \sigma T_S^4$, we have

$$\dot{R}^2 = \eta\sigma T_S^4 R^2, \tag{33}$$

$$\dot{T}_S = \sqrt{\eta\sigma}\, T_S^3, \quad \frac{1}{T_S^2(t_0)} - \frac{1}{T_S^2(t_1)} = 2\sqrt{\eta\sigma}\,(t_1 - t_0). \tag{34}$$

To consider the contraction process of $B_S^{(i)}$. Let $T_S(t_0) = 1\,\text{MeV}$, $\sigma = 25$ and $T_S(t_1) = T_{\max} = 10^{15}$ GeV. we get $(t_1 - t_0) \approx 0.3\,\text{s}$. 10^{15}GeV is the energy scale of the $SU(5)$ grant unified theory. At the energy scale $\langle \Omega_S \rangle = 0$ and the expectation values of other s-Higgs fields are all zero because of the temperature effect (12), $V = V_0 = V(0) - U_{\min} = \mu^4/4\lambda$ inside $B_S^{(i)}$, and $\langle \Omega_S \rangle = \langle \Omega \rangle_0$ and $V = 0$ outside $B_S^{(i)}$. There must be a transit zone (T-zone) which satisfies (3) in the boundary zone of $B_S^{(i)}$. As mentioned before, $\langle \Omega_V \rangle = 0$ in the s-cosmic island. In the case, the s-elementary particles and the v-elementary particles can transform to each other because $\langle \Omega_S \rangle = \langle \Omega_V \rangle = 0$ inside $B_S^{(i)}$. The v-colour

singlets can freely escape out $B_S^{(i)}$ due to $\langle\Omega_V\rangle = 0$ in every zone. But the s-colour singlets cannot easily escape out $B_S^{(i)}$ due to $\langle\Omega_S\rangle = \langle\Omega\rangle_0$ and $V = 0$ outside $B_S^{(i)}$. Let ρ_{SCI} and ρ_{VCI} be the energy densities of s-colour singlets and v-colour singlets in the I-zone, respectively, there must be $\rho_{SCI} > \rho_{VCI}$ and $T_{SI} > T_{VI}$, because the v-colour singlets can freely escape out $B_S^{(i)}$. Consequently, it must occur inside $B_S^{(i)}$ that

$$\langle\Omega_V\rangle = 0 \to \langle\Omega_V\rangle = \langle\Omega\rangle_0, V_{SI} = V_0 \to V_{SI} = 0, \tag{35}$$

and $\langle\Omega_S\rangle = 0$ is unchanged. Thus, a v-cosmic island called $C_V^{(i)}$ appears. It is seen from (35) that a huge s-black hole $B_S^{(i)}$ can transform into a v-cosmic island $C_V^{(i)}$ inside an s-cosmic island and it is necessary that there simultaneously are the two sorts of symmetry breaking in the universe so long as there are huge black holes inside $C_S^{(1)}$.

Evolution of C_V can be determined by the discussions similar to those in last subsection of above section, so long as to exchange the subscripts S and V in the subsection. The v-cosmic islands $C_V^{(2)}$ and $C_V^{(3)}$ are corresponding to $C_S^{(2)}$ and $C_S^{(3)}$, respectively.

The inflation or expansion process after contraction of an s-cosmic island or a v-cosmic island in the universe is similar to the following process. To suppose that there is an infinite planar rubber membrane, its a zone of radius R becomes semi-spherical due to being heated. There is no significant change of its border, but the area of this zone has significantly increased in the process. Then the semi-spherical gradually become flat and tis border significantly increases.

It is obvious that the evolution of the first class of black hole is essentially different from that of the second class of black holes. It is possible that a second class black hole will disappear by the Hawking radiation.

It is seen from the above mentioned that s-matter and v-matter can transform into each other when the temperature T inside a black hole or a cosmic island arrives the highest temperature $T_{\max}$.

4.2. The Characteristics of the V-Cosmic Island and Some Predictions

1) The v-cosmic island inside a the s-cosmic island $C_S^{(1)}$ cannot be very large and its largest T-intensity of pressure $P_T(t_0) = P_{T\max} \sim V_0$, because it stems from a huge black hole inside $C_S^{(1)}$. Hence there are the actual v-cosmic islands to be the two classes $C_V^{(2)}$ and $C_V^{(3)}$. $C_V^{(2)}$ and $C_V^{(3)}$ are similar to $C_S^{(2)}$ and $C_S^{(3)}$, their lifespan are all short.

2) Huge black holes can only be formed in earlier times of the s-cosmic island $C_S^{(1)}$, because $C_S^{(1)}$ expands and the celestial bodies inside $C_S^{(1)}$ are away from each other so that the celestial bodies cannot gather to form a huge black late. Consequently, the huge black holes can only appear in earlier times.

3) There is no s-celestial body around $C_V^{(i)}$ because the repulsion $C_V^{(i)}$ on s-celestial bodies. After the s-black hole $B_S^{(i)}$ transforms into the v-cosmic island $C_V^{(i)}$, the celestial bodies around $B_S^{(i)}$ must go away. The v-cosmic island

$C_V^{(i)}$ must be solitary inside the s-cosmic island.

4) $C_V^{(2)}$ and $C_V^{(3)}$ can emit a lot of s-particles and v-colour singlets. Particularly, when $C_V^{(2)}$ and $C_V^{(3)}$ will disappear, they will emit huge quantity of s-particles and v-colour singlets. A observer in the earth cannot detect the v-colour singlets, but can detect the s-particles. Only s-photons and neutrinos can be detected. Other s-particles are hard detected because they must suffer many interactions on their long roads or have decayed.

5) The characteristics of the detected s-photons and s-neutrinos on the earth as follows.

a) The red shifts of the detected s-photons and the s-neutrinos must be very large, because $C_v^{(2)}$ and $C_v^{(3)}$ must be formed in earlier times and their lifespan are all short.

b) The intensities of the photons and the neutrinos are huge relatively to their distance, and the luminescence spectrum is very wide..

c) The headstreams of the detected s-photons and s-neutrinos must be solitary due to the repulsion of $C_v^{(2)}$ and $C_v^{(3)}$ on s-celestial bodies.

Based the characteristics, we guess that

a) $C_v^{(2)}$ and $C_v^{(3)}$ are so-called orphan quasars;

b) Distribution of the orphan quasars is anisotropic, because it is possible that the earth is not in the centre of the present s-cosmic island $C_S^{(1)}$.

5. Structure of the Universe

5.1. The Universe Is Composed of Infinite S-Cosmic Islands, V-Cosmic Islands and Transition Regions

As described above, the s-cosmic islands and the v-cosmic islands can simultaneously exist. Based on this, we think that the universe is composed of infinite s-cosmic islands, infinite v-cosmic islands and infinite transition regions among the s-cosmic islands and the v-cosmic islands. It is necessary that the cosmic islands adjacent to an s-cosmic island must be v-cosmic islands, because if two s-cosmic islands are adjacent, both will combine into a larger s-cosmic island. This is true for two adjacent v-cosmic islands as well. No information can be exchanged between an s-cosmic island and a adjacent v-cosmic island so that every observer thinks his cosmic island to be the whole universe. The evolution process of a huge cosmic island is as follows: Contraction, contraction stops, expansion, inflation, reheating process, expansion, expansion with an acceleration, expansion with a deceleration, expansion stops and contraction begin. There is no inflation process in the evolution process of a larger and small cosmic island. Every cosmic island has its life and death. The existing and changing forms of the cosmic islands must be diverse. It is possible that some cosmic islands are contracting, some cosmic islands are expanding, and other cosmic islands are stable for a time. Some cosmic islands are forming, and some cosmic islands are disappearing, some cosmic islands are combining to form a larger cosmic island, and some cosmic islands are splitting into few smaller

cosmic island. Every existence has its birth and death, and is changing. Only the universe as a whole is infinite and always unchanging, and contains all possible existing and changing forms.

The interior of cosmic island is uniform, but is not absolutely isotropic for such an observer who is not in the centre of his cosmic island. Thus, the cosmological principle holds only approximately within a cosmic island because every cosmic island must be finite. There is no singularity in every cosmic island and in the whole universe.

There are many s-black holes inside a huge s-cosmic island. A huge s-black hole can transform into a v-cosmic island in the huge s-cosmic island. The evolution of the v-cosmic island is the same as that of a large or small s-cosmic island. An observer in the s-cosmic island can detect the s-photons and neutrinos emitted by the v-cosmic island.

The present cosmological model is essentially different from the conventional cosmological theory. If the universe comes from a singularity as the conventional theory, there must be only one sort of breaking, there is no cosmic island, and the universe as a whole is variational.

5.2. No Information Can Be Exchanged between an S-Cosmic Island and an Adjacent V-Cosmic Island

When $\langle\Omega_S\rangle = \langle\Omega\rangle_0$ and $\langle\Omega_V\rangle = 0$ or $\langle\Omega_V\rangle = \langle\Omega\rangle_0$ and $\langle\Omega_S\rangle = 0$, the masses of the Higgs particles Ω_V and Ω_S are all very large [1]. Hence the interactions between s-particles and v-colour singlets by exchanging the Higgs particles must be very weak so that they may be ignored. The repulsion between s-particles and v-colour singlets are very weak and may be ignored as well. Consequently, it is impossible that v-colour singlets are detected in an s-cosmic island, It is true as well that s-colour singlets cannot be detected in a v-cosmic island. Colour singlets have only the cosmological effects and are regarded as dark energy [1].

Let a $SU_V(5)$ colour singlet S_V in an s-cosmic island enter into an adjacent v-cosmic island. S_V is a dark energy particle in the s-cosmic island so that S_V cannot carry any information to the v-cosmic island. After S_V enters the v-cosmic island, it will splits into few v-particles whose proper masses are not zero. The v-particles and the original v-particles in the v-cosmic island mix together and cannot be differentiate from each other.

Let s-particles in the s-cosmic island enter into the T-zone, and some s-particles combine each other to form a quasi $SU_S(5)$ colour singlet $\tilde{S}_S$ in the T-zone, then $\tilde{S}_S$ can enter into the v-cosmic island and become $SU_S(5)$ colour singlet S_S. S_S cannot be detected by v-observers because there is no interaction between S_S and v-particles. Such s-particles which do not combine to quasi s-colour singlets in the T-zone cannot enter the v-cosmic island. Consequently, the s-cosmic island cannot convey any information to the s-cosmic island, and vice verse. Thus, the observers in every cosmic island will

all think their cosmic island to be the whole universe.

Although no information can be exchange between our cosmic island and the adjacent v-cosmic islands, some s-colour singlets inside the v-cosmic islands can enter into our cosmic island. The s-colour singlets entering into our cosmic island are visible particles. Consequently, in fact, the boundary of our cosmic island is slightly anisotropic, because the distribution of the adjacent v-cosmic islands. Around our s-cosmic island is not symmetric. Of course, the slight anisotropy is too hard observed.

6. Conclusions

Based on [1], a possible structure of the universe is presented. It is proved that there must simultaneously be two sorts of symmetry breaking in the universe. The universe is composed of infinite s-cosmic islands, infinite v-cosmic islands and infinite transition zone. It is necessary that the cosmic islands adjacent to an s-cosmic island must be v-cosmic islands. No information can be exchanged between an s-cosmic island and an adjacent v-cosmic island so that every observer thinks his cosmic island to be the whole universe.

The evolution process of a huge cosmic island is as follows: contraction, contraction stops, expansion, inflation, reheating process, expansion, expansion with an acceleration, expansion with a deceleration, expansion stops and contraction begin. There is no inflation process in the evolution process of a larger and small cosmic island.

The existing and changing forms of the cosmic islands must be diverse. It is possible that some cosmic islands are contracting, some cosmic islands are expanding, and other cosmic islands are stable for a time. But the universe as a whole is infinite, always invariable and contains all possible existing and changing forms of matter.

The cosmological principle holds only approximately within a cosmic island. To give a possible explaintion for orphan quasars. To predict some characteristics of contracting large and huge black holes in a cosmic island. The characteristics of the light coming from the contracting huge black holes are that the intensity of the light is huge relatively to their distance, the red shifts are huge, the distribution of the huge red shifts and the orphan quasars is anisotropic, and luminescence spectrum is very wide.

Acknowledgements

This work is supported by National Natural Science Foundation of China (No. 11075064). I am very grateful to them.

Conflicts of Interest

The authors declare no conflicts of interest regarding the publication of this paper.

References

[1] Chen, S.H. (2014) A Cosmological Model without Singularity Based on RW Metric

(1). *International Journal of Astronomy and Astrophysics*, **4**, 264-293. https://doi.org/10.4236/ijaa.2014.41023

[2] Chen, S.H. (2016) A Locally Conservative Energy-Momentum Tensor in the General Relativity Based on a Cosmological Model without Singularity. *Journal of Modern Physics*, **7**, 4. https://doi.org/10.4236/jmp.2016.73027

[3] Hubbard, K.A. (ed.) (2008) The In Ationary Multiverse. *Frontier Science*, **2**, 37-44.

International Journal of Astronomy and Astrophysics, 2018, 8, 339-346
http://www.scirp.org/journal/ijaa
ISSN Online: 2161-4725
ISSN Print: 2161-4717

Effects of Time Dilation on the Measurements of the Hubble Constant

Naser Mostaghel

Civil Engineering Department, University of Toledo, Toledo, USA
Email: naser.mostaghel@utoledo.edu

How to cite this paper: Mostaghel, N. (2018) Effects of Time Dilation on the Measurements of the Hubble Constant. *International Journal of Astronomy and Astrophysics*, **8**, 339-346.
https://doi.org/10.4236/ijaa.2018.84024

Received: October 7, 2018
Accepted: December 7, 2018
Published: December 10, 2018

Abstract

We show that, when measuring the Hubble constant by starting the evaluation from the time of the big bang era, the effect of time dilation results in a decrease in the value of the Hubble constant. But when evaluating the Hubble constant by starting the evaluation from the present time, the effect of time dilation results in an increase in the value of the Hubble constant. To elucidate the process, the time dilation is calculated both directly and through Schwarzschild solution of the Einstein equation for the gravitational time dilation. It is concluded that both measured values are valid but because of time dilation, different starting times for the evaluation of the Hubble constant have resulted in different measured values for the Hubble constant.

Keywords

Hubble Constant, Time Dilation, Redshift, Time Symmetry, Gravitation

1. Introduction

The recently reported measured value for the Hubble constant by the Plank team [1] is $H_0 = 67.66 \pm 0.42\ \text{km}\cdot\text{s}^{-1}\cdot\text{Mpc}^{-1}$. The Plank team obtains this value for H_0 by using the cosmic microwave background (CMB) data together with the ΛCDM standard model. Since CMB happens in the recombination era, the process involves evaluating the Hubble time from the surface of last scattering to the present time and then calculating the value for H_0. In this measurement, the direction of time is future pointing, that is, toward the future as it progresses from the surface of last scattering toward the present time. Thus as the length of time from the center of gravity is increased, the hold of gravity on time is decreased. The evaluated Hubble time intrinsically includes the time dilation.

Another measured value for the Hubble constant, reported by the Reiss team

[2] is $H_0 = 73.24 \pm 1.7\ \mathrm{km \cdot s^{-1} \cdot Mpc^{-1}}$. This team starts its evaluation from the present time by measuring both the redshift and distance first and then calculating the H_0. In this measurement the redshift increases as one goes back from the present time. Here the direction of time, for evaluation of H_0, is past pointing, that is, toward the surface of last scattering. Thus as the length of time to the center of gravity is decreased, the hold of gravity on time is increased. In this case the evaluated H_0 also intrinsically includes the effect of time dilation.

The discrepancy or tension between the above two values of H_0 has been puzzling [3] [4] [5]. Here we first evaluate a reference Hubble constant without including the time dilation. Then we show that including the time dilation and starting the evaluation from the surface of last scattering proceeding toward the present time yields $H_0 = 67.8236\ \mathrm{km \cdot s^{-1} \cdot Mpc^{-1}}$. This value of H_0 is remarkably consistent with the Plank measured value. Then, still including the time dilation, we reverse the starting point for the evaluation of H_0. We show that starting the evaluation from the present time proceeding toward the surface of last scattering yields $H_0 = 74.2119\ \mathrm{km \cdot s^{-1} \cdot Mpc^{-1}}$ which is also consistent with the value measured by Reiss *et al.* It is concluded that, because of time dilation, the direction of evaluation of the Hubble time is the cause of discrepancy or tension between the two measured values.

2. Evaluation of the Reference Hubble Constant

According to General Relativity (GR) time and space are coupled and a global reversal of coordinate system has no effect on the result. That is, time symmetry is inherent in GR. Because in the above two measurements the reversal of the proper time of a single world-line from a future-pointing to a past-pointing has resulted in different values for the Hubble constant; the time symmetry is broken [6]. As such one cannot use GR in its classical form to address the problem at hand. In the Plank measurement the direction of time is pointing toward the future while in the Reiss measurement the direction of time is pointing toward the past. In the following it is shown that in the Plank measurement, because the time dilation is positive it increases the Hubble time, resulting in a lower value for the Hubble constant. But in the Reiss measurement, because the time dilation is negative, it decreases the Hubble time, resulting in a higher value for the Hubble constant. It should be noted that the Friedmann-Robertson-Walker model (FRW) of the standard model of relativistic cosmology includes both isotropy and homogeneity, Peacock [7]. But the effect of time dilation does not directly show up in the FRW model because the FRW model is based on General Relativity, in which time is symmetric. Below it will be shown that the time dilations for the future pointing and the past pointing measurements have opposite signs. Increasing entropy with the forward flow of time (which is not included in GR) may be the cause of the broken symmetry.

Here we first evaluate a reference Hubble constant not including the effect of time dilation. Then we evaluate the effects of time dilation on the above two measurements. Because of broken time symmetry, as an alternative exploration

to GR, let $T_e(t)$ represent the expanding time part of the expanding universe where cz represents the rate of expansion of the universe. Since the speed of light, c, is constant, the redshift, z, represents the rate of change of the expanding time, $T_e(t)$. It has been shown that the quantity $a_t = z^2/t$ represents the second rate or the acceleration of $T_e(t)$ at the present time [8]. Thus, the spatial velocity, $v(t)$, and the spatial acceleration, $a(t)$, of the expansion of the universe, in this simple model, are given by

$$v(t) = cz(t) \tag{1}$$

$$a(t) = ca_t(t) = \frac{c\left(z(t)\right)^2}{t} = \frac{\left(v(t)\right)^2}{R(t)} \tag{2}$$

The acceleration, $a(t)$, is a centrifugal acceleration and its effect according to the equivalence principle of GR is equivalent to gravitational acceleration. Thus

$$a(t) = \frac{\left(v(t)\right)^2}{R(t)} = \frac{c\left(z(t)\right)^2}{t} = \frac{GM}{\left(R(t)\right)^2} = \frac{GM}{c^2t^2} \tag{3}$$

Because the sign of $a(t)$ is positive, it represents a repulsive inertia acceleration. The above relation yields

$$\left(z(t)\right)^2 = \frac{GM}{c^3t} \tag{4}$$

Considering the radius of the universe at the time of the big bang to have been equal to ct_p where $t_p = 5.391157549003072\times10^{-44}$ s represents the Plank time (the smallest unit of time), based on Equation (4) the total mass of our universe, M, is given by

$$M = \frac{c^3\left(z_p\right)^2 t_p}{G} \tag{5}$$

where z_p represents the Plank redshift. Since the total mass of the universe, M, is conserved, Equation (5) implies that

$$\frac{GM}{c^3} = \left(z_p\right)^2 t_p = \left(z_H\right)^2 t_{St} = \left(z(t)\right)^2 \frac{t}{2} \tag{6}$$

where t_{St} represents the radius of the surface of last scattering (the horizon) and z_H represents its corresponding redshift, and $t/2$ represents the time distance from the big bang at any time t.

We evaluate the Plank redshift, z_p, based on Plank temperature, $\tau_p = 1.416807993748161\times10^{32}$ K, the black body radiation temperature at the present time, and Wien's displacement law [9] [10] according to the following relations

$$z_p = \frac{\lambda_o}{\lambda_e} - 1 = \frac{\tau_{\text{then}}}{\tau_{\text{now}}} - 1 = \frac{\tau_p}{2.72548} - 1 = \frac{1.41681\times10^{32}}{2.72548} = 5.19838\times10^{31} \tag{7}$$

From the CMB radiations at the time of decoupling, the temperature has been estimated to have been about 3000 K, and the black body radiation temperature

now is $\tau_{\text{now}} = 2.72548\ \text{K}$ [11]. From relations (7) one obtains

$$z_H = \frac{\tau_{\text{then}}}{\tau_{\text{now}}} - 1 = \frac{3000}{2.72548} - 1 = 1099.7235 \tag{8}$$

From Equation (6) the radius of the surface of last scattering, t_{St}, is given as

$$t_{St} = \frac{\left(z_p\right)^2 t_p}{\left(z_H\right)^2} = 1.20462251807 \times 10^{14}\ \text{s} \tag{9}$$

Thus the reference Hubble time, $\left(t_H\right)_r$, is given by

$$\left(t_H\right)_r = t_0 - t_{St} = 4.35374417748 \times 10^{17}\ \text{s} \tag{10}$$

where $t_0 = 13.8\ \text{Gyr}$ represents the assumed age of the universe at the present time. Therefore, the reference Hubble constant, $\left(H_0\right)_r$, is given by

$$\left(H_0\right)_r = \left(\frac{1}{\left(t_H\right)_r}\right)\frac{\text{Mpc}}{1000} = 70.874\ \text{km}\cdot\text{s}^{-1}\cdot\text{Mpc}^{-1} \tag{11}$$

3. Evaluation of the Effects of Time Dilation on the Hubble Constant

Here we show that the effect of time dilation manifests itself in two ways. If we make our measurement toward the present time, the effect of a positive change in time is a negative change in the redshift. But if we make our measurement toward the big bang, the effect of a negative change in time is a positive change in the redshift. Let δt represent a small change in time. Since according to Equation (6)

$$\frac{t}{2} = \frac{\left(z_p\right)^2 t_p}{z^2} \tag{12}$$

it follows that

$$t \pm \delta t = \frac{2\left(z_p\right)^2 t_p}{\left(z \mp \delta z\right)^2} \tag{13}$$

That is, a positive change in the value of time, *t*, corresponds to a negative change in the value of the redshift, *z*. But a positive change in the value of redshift corresponds to a negative change in the value of time. If we start the measurement from the surface of last scattering to the present time, t_0, the length of time is $\left(t_H\right)_r = t_0 - t_{St}$. Thus the corresponding change in redshift is given by

$$\delta z_1 = z\left(t_0\right) - z\left(t_H\right)_r \tag{14}$$

Substitutions for $z\left(t_0\right)$ and $z\left(t_H\right)_r$ using Equation (12) yield the change in the redshift as

$$\delta z_1 = \sqrt{\frac{2\left(z_p\right)^2 t_p}{t_0}} - \sqrt{\frac{2\left(z_p\right)^2 t_p}{\left(t_H\right)_r}} = -0.0035782\ \text{s/s} \tag{15}$$

Due to initial conditions, $z\left(t_0\right)$ is not zero, but its effect cancels out. In

making the measurement toward the present time one is moving away from the gravitational center in the direction of increasing time, which according to Equation (4) causes a reduction or a negative change in the value of the redshift. Since δz_1 is negative, the change in time according to Equation (13) must be positive. Thus changing the sign of δz_1, one obtains the time dilation as

$$\Delta t_1 = 2\left(-\delta z_1 \times 2\pi t_0\right) = 1.9581837 \times 10^{16} \text{ s} \tag{16}$$

Factor 2 in the above equation represents the fact that, from the time of the big bang, the expanding time expands both toward the earth and in the opposite direction. The 2π factor represents the fact that, based on Equation (3), the path of expanding time is circular. Now evaluating the Hubble time via evaluation based on measurement from the surface of last scattering toward the present time, including time dilation, one obtains the Hubble time as

$$\left(t_H\right)_1 = \left(t_H\right)_r + \Delta t_1 = 4.5495625 \times 10^{17} \text{ s} \tag{17}$$

where $\left(t_H\right)_r$ is the reference Hubble time given in Equation (10). Therefore the present time value of the Hubble constant, in this case, is calculated to be

$$\left(H_0\right)_1 = \frac{1}{\left(t_H\right)_1}\frac{\text{Mpc}}{1000} = 67.824 \text{ km}\cdot\text{s}^{-1}\cdot\text{Mpc}^{-1} \tag{18}$$

The above value for the Hubble constant is consistent with Plank's value of $H_0 = 67.66 \pm 0.42$.

In the foregoing case the evaluation of the Hubble time, $\left(t_H\right)_1$, is from the surface of last scattering to the present time, t_0, on earth. Now we consider evaluation of the Hubble constant through measurement of redshift from the present-time toward the surface of last scattering. Reversing the direction of evaluation of Hubble time causes the change in the redshift to be positive. This is so because in making the measurement going back from the present-time one is moving toward the gravitational center, reducing the length of time and, according to Equation (4), causing an increase or a positive change in the value of the redshift. The length of time to the surface of last scattering is $\left(t_H\right)_r = t_0 - t_{St}$. Thus the change in redshift is

$$\delta z_2 = z\left(t_H\right)_r - z\left(t_0\right) = \sqrt{\frac{2\left(z_p\right)^2 t_p}{\left(t_H\right)_r}} - \sqrt{\frac{2\left(z_p\right)^2 t_p}{t_0}} = 0.0035782 \text{ s/s} \tag{19}$$

Since δz_2 is positive, the change in time according to Equation (13) must be negative. Thus changing the sign of δz_2 one obtains the time dilation as

$$\Delta t_2 = 2\left(-\delta z_2 \times 2\pi t_0\right) = -1.9581837 \times 10^{16} \text{ s} \tag{20}$$

Consequently the Hubble time including the effect of time dilation is given by

$$\left(t_H\right)_2 = \left(t_H\right)_r + \Delta t_2 = 4.1579258 \times 10^{17} \text{ s} \tag{21}$$

Thus the Hubble constant including the effect of time dilation is given by

$$\left(H_0\right)_2 = \frac{1}{\left(t_H\right)_2}\frac{\text{Mpc}}{1000} = 74.212 \text{ km}\cdot\text{s}^{-1}\cdot\text{Mpc}^{-1} \tag{22}$$

The above value for the Hubble constant is consistent with the Reiss, *et al.* value of $H_0 = 73.24 \pm 1.7$.

4. Time Dilation Based on the Schwarzschild Solution

As an approximate check on the numerical values of the time dilations calculated above, assuming the total mass of the universe to be non-rotating and spherically-symmetric, here we explore the use of the Schwarzschild solution of the Einstein equation for the gravitational time dilation between points close and far from the gravitational center. The Schwarzschild solution has been a useful approximation for describing slowly rotating astronomical objects such as stars and planets [12] [13]. The solution is given as

$$t_0 = \tilde{t}\sqrt{1-\frac{2GM}{c^3 t_0}} = \tilde{t}\sqrt{1-\frac{2\left(z_p\right)^2 t_p}{t_0}} \tag{23}$$

where t_0 and $\tilde{t}$ correspond to slow-ticking and fast-ticking clocks respectively. The length of time between the surface of last scattering and the earth is $\left(t_H\right)_r = t_0 - t_{St}$. Therefore, based on Equation (6) the corresponding change in the redshift, *z*, due to time dilation, is given by

$$\delta\tilde{z}_1 = \frac{t_0}{\tilde{t}_0} - \frac{t_H}{\left(\tilde{t}_H\right)_r} = \left|\sqrt{1-\frac{2\left(z_p\right)^2 t_p}{t_0}}\right| - \left|\sqrt{1-\frac{2\left(z_p\right)^2 t_p}{\left(t_H\right)_r}}\right| = -0.0035808 \text{ s/s} \tag{24}$$

where, to avoid imaginary values, as an exploratory evaluation, we have used the absolute values. Thus the time dilation is given by

$$\Delta\tilde{t}_1 = 2\left(-\delta\tilde{z}_1 \times 2\pi t_0\right) = 1.9596485\times 10^{16} \text{ s} \tag{25}$$

Now calculating the Hubble time via evaluation based on measurement from the surface of last scattering toward the present time, including time dilation, one obtains the Hubble time as

$$\left(\tilde{t}_H\right)_1 = \left(t_H\right)_r + \Delta\tilde{t}_1 = 4.5497090\times 10^{17} \text{ s} \tag{26}$$

where $\left(t_H\right)_r$ is the reference Hubble time given in Equation (10). Therefore the present time value of the Hubble constant in this case is given by

$$\left(\tilde{H}_0\right)_1 = \frac{1}{\left(\tilde{t}_H\right)_1}\frac{\text{Mpc}}{1000} = 67.821 \text{ km}\cdot\text{s}^{-1}\cdot\text{Mpc}^{-1} \tag{27}$$

Reversing the direction of evaluation, the change in redshift due to time dilation is given by

$$\delta\tilde{z}_2 = \frac{t_H}{\left(\tilde{t}_H\right)_r} - \frac{t_0}{\tilde{t}_0} = \left|\sqrt{1-\frac{2\left(z_p\right)^2 t_p}{\left(t_H\right)_r}}\right| - \left|\sqrt{1-\frac{2\left(z_p\right)^2 t_p}{t_0}}\right| = 0.0035808 \text{ s/s} \tag{28}$$

Thus the value of time dilation is given by

$$\Delta\tilde{t}_2 = 2\left(-\delta\tilde{z}_2 \times 2\pi t_0\right) = -1.9596485\times 10^{16} \text{ s} \tag{29}$$

Table 1. Measured and calculated values of Hubble constant.

	H_0 km·s^{-1}·Mpc^{-1} Measured	$(H_0)^*$ km·s^{-1}·Mpc^{-1} Calculated	$(\tilde{H}_0)^{**}$ km·s^{-1}·Mpc^{-1} Calculated
Plank 2018	67.66 ± 0.42	67.824	67.821
Reiss *et al.*	73.24 ± 1.7	74.212	74.215

*Time dilation is evaluated directly; **Time dilation is evaluated based on the Schwarzschild solution.

Consequently the Hubble time including the effect of time dilation in this case is given by

$$\left(\tilde{t}_H\right)_2 = \left(t_H\right)_r + \Delta\tilde{t}_2 = 4.1577793\times10^{17}\ \text{s} \tag{30}$$

Thus the Hubble constant including the effect of time dilation is calculated to be

$$\left(\tilde{H}_0\right)_2 = \frac{1}{\left(\tilde{t}_H\right)_2}\frac{\text{Mpc}}{1000} = 74.215\ \text{km}\cdot\text{s}^{-1}\cdot\text{Mpc}^{-1} \tag{31}$$

For comparison, the calculated Hubble constants and the measured ones are presented in Table 1.

5. Conclusion and Remarks

Based on the results presented above it is clear that, because of time dilation, the measurement of H_0 is sensitive to the direction in which the measurement is performed, that is toward the present time or away from it. Therefore, considering the directions of evaluation, both measured values of the Hubble constant are valid. Removal of time dilation would yield a unique value for H_0. However, because time dilation is inherent in the evaluation of the length of time, its effect cannot be removed through more precise measurements. Also according to Equation (3) the redshift, z, that is, the rate of change of the expanding time, $T_e(t)$, can represent the repulsive gravity.

Conflicts of Interest

The author declares no conflicts of interest regarding the publication of this paper.

References

[1] Aghanim, N., Akrami, Y., Ashdown, M., *et al.* (2018) Plank 2018 Results. VI. Cosmological Parameters. https://arxiv.org/abs/1807.06209

[2] Riess, A.G., Casertano, S., Yuan, W., *et al.* (2018) Milky Way Cepheid Standards for Measuring Cosmic Distances and Application to *Gaia* DR1: Implications for the Hubble Constant. https://arxiv.org/abs/1804.10655

[3] Freedman, W.L. (2017) Cosmology at Crossroads: Tension with the Hubble Constant. https://arxiv.org/abs/1706.02739

[4] Donna Weaver, D. and Villard, R. (2018) Improved Hubble Yardstick Gives Fresh Evidence for New Physics in the Universe. NASA.

https://www.nasa.gov/feature/goddard/2018/improved-hubble-yardstick-gives-fresh-evidence-for-new-physics-in-the-universe/

[5] Devlin, H. (2018) The Answer to Life, the Universe and Everything Might Be 73. Or 67. *The Guardian*. https://www.theguardian.com/science/2018/may/10/the-answer-to-life-the-universe-and-everything-might-be-73-or-67

[6] Ripalda, J.M. (2010) Time Reversal and Negative Energies in General Relativity. arXiv:gr-qc/9906012, v14.

[7] Peacock, J. (1999) Cosmological Physics. Cambridge University Press, Cambridge.

[8] Mostaghel, N. (2018) The Role of Time in Cosmic Expansion. *American Journal of Astronomy and Astrophysics*, **6**, 9-21.

[9] NIST, CODATA VALUE: Wien Wavelength Displacement Law Constant. http://physics.nist.gov/cgi-bin/cuu/Value?bwien

[10] Wikipedia, Wien's Displacement Law. https://en.wikipedia.org/wiki/Wien%27s_displacement_law

[11] Fixsen, D.J. (2009) The Temperature of the Cosmic Microwave Background. *The Astrophysical Journal*, **707**, 916-920. https://doi.org/10.1088/0004-637X/707/2/916

[12] Wikipedia, Gravitational Time Dilation. https://en.wikipedia.org/wiki/Gravitational_time_dilation

[13] Wikipedia, Schwarzschild Solution. https://en.wikipedia.org/wiki/Schwarzschild_metric

International Journal of Astronomy and Astrophysics, 2018, 8, 347-367
http://www.scirp.org/journal/ijaa
ISSN Online: 2161-4725
ISSN Print: 2161-4717

Star Formation in Magnetized, Turbulent and Rotating Molecular Cloud: The Critical Mass

Gemechu Muleta Kumssa, Solomon Belay Tessema

Astronomy and Astrophysics Research Division, Entoto Observatory and Research Center (EORC), Ethiopian Space Science and Technology Institute (ESSTI), Addis Ababa, Ethiopia
Email: gemechumk@gmail.com, tessemabelay@gmail.com

How to cite this paper: Kumssa, G.M. and Tessema, S.B. (2018) Star Formation in Magnetized, Turbulent and Rotating Molecular Cloud: The Critical Mass. *International Journal of Astronomy and Astrophysics*, **8**, 347-367.
https://doi.org/10.4236/ijaa.2018.84025

Received: August 27, 2018
Accepted: December 7, 2018
Published: December 10, 2018

Abstract

In this paper, we present the critical mass of magnetized, turbulent and rotating star-forming molecular cloud core (MCc) in the presence of magnetic tension. The critical mass of star-forming magnetized cloud is influenced by the magnetic tension, magnetic pressure and other pressures. Applying the method of theoretical modelling by taking into account the basic equations and assumptions, we formulate the critical mass of magnetized MCc in different cases. Accordingly, the minimum critical masses we find in both cases are different. Energy due to magnetic tension significantly triggers the collapse at relatively larger radius of the core. The model shows that when the initial radius of the parent cloud (R_o) is larger than that of collapsing core radius (R_{core}) the magnetic tension also has the larger radius of curvature, so it plays a significant role in supporting gravity to collapse the core. The results indicate gravity without magnetic tension may not overcome magnetic pressure, turbulence pressure and pressure due to rotation. This shows the critical mass of MCc for the collapse depends on the tension force that magnetic field lines apply on the envelope. We conclude that if there is magnetic pressure in star-forming MCc, there is also unavoidable magnetic tension, which triggers the collapse of the core. If there is no magnetic tension, the magnetized MCc needs relatively larger mass and higher density within the small size to collapse.

Keywords

Star Formation, Molecular Cloud, Critical Mass, Magnetic Field, Turbulence, Magnetic Tension

1. Introduction

Star formation is one of the most important and yet unsolved problems of

astrophysics. It plays an important role in many different areas of astrophysics, especially in the field of galaxy formation and evolution [1]. Without a theory of star formation, it will be difficult to understand the origin of galaxies and luminous matter in our universe. Molecular cloud is a cool dense interstellar region composed of a wide variety of molecules, mainly hydrogen, plus some dust, in which stars are forming. Cores are the denser sites of star formation in molecular clouds with number density $\gtrsim 10^3$ cm^{-3} [2]. A star forms as the final stage of various complexes, non-linear dissipative processes that are the result of the interplay between turbulent, thermal and magnetic pressure effects on one side and gravity on the other side [3]. However, how star formation is triggered and inhabited by pressures supporting gravity and opposing gravity needs a detail theoretical formulation by incorporating magnetic tension.

The standard theory simply related to the magnetic fields of the progenitor main-sequence stars frozen during collapse or flux conservation [4]. This model does not deliver the mechanism how magnetic field supports and opposes gravity in star formation. Understanding the origin and evolution as well as physical behaviour of the complex process of star formation (SF) is still an ongoing research area in modern astrophysics. Solving those problems will help to develop a theory regarding origin of stars. Some of unanswered questions regarding the role of magnetic fields in star formation are: What is the effect of magnetic fields on MC core collapse? It has been suggested that magnetic fields suppress fragmentation [5]. The other way suggested is that the presence of magnetic fields may enhance fragmentation [6]. To this end, we perform theoretical formulation how magnetic field counteracts gravity and how magnetic tension supports gravity in a gravitating, magnetized turbulent rotating MCc.

The first numerical calculations of the collapse of a molecular cloud core to stellar-core formation and beyond was performed by [7]. Where as [8] combined the radiation hydrodynamical (RHD) method of [9] and the magnetohydrodynamical method of [10] and performed the first smoothed particle radiation magnetohydrodynamic (SPRMHD) calculations of protostellar collapse to stellar-core formation. In this paper, we combine energies due to gravity opposing pressures and energies of gravity supporting pressures to formulate the critical mass of gravitating, magnetized, turbulent and rotating MC core in the presence of magnetic tension effect. Thus we show how those pressures counteract and support gravity in dispersing and collapsing MC core respectively.

Clouds do not become gravitationally bound, and they dissipate; those that are self-gravitating form stars in essentially a free-fall time [11] [12]. But what if the cloud is strongly magnetized? This needs additional theoretical formulation to understand how magnetic pressure, with turbulence and rotation controls star formation. It is also necessary to describe how the size of the core influences magnetic pressure and magnetic tension. In other case it has been explained that supersonic turbulence will dissipate on roughly the free-fall time scale as collapse of gravitationally bound clouds [13] [14]. Although magnetic pressure cannot

stop the collapse [15] [16]. Strong magnetic pressure together with supersonic turbulence in large scale and pressure due to rotation can dominate gravity and elongate the SF time. Therefore, we intend to explain how magnetic tension supports gravity in collapsing the MCc. The general purpose of the study is: Theoretically to formulate the critical mass of gravitating, magnetized, turbulent and rotating MCc in the presence of restoring force due to magnetic tension.

2. Basic Equations and Approximations

In the process of star formation different energy pressures are involving in collapsing as well as holding the cloud. As an initial condition we assume gravitating, magnetized, turbulent and rotating molecular cloud. Some energies are supporting gravity and some are opposing gravity during star forming process. The energies involved in star formation are originated from, gravity, magnetic field, turbulence, rotation, thermal effect as well as external pressures. For the MC initially in force balance, the combination of these energies is written as

$$\left|E_g + E_{mt}\right| = 2E_{th} + 2E_{turb} + 2E_{rot} + E_m - \rho v^2 V \tag{1}$$

where E_g is the total gravitational energy, E_{th} is the total thermal energy, E_m is the total magnetic energy (If B inside is greater than out side), E_{mt} is energy due to the magnetic tension, E_{turb} energy due to turbulent motion, E_{rot} is rotational energy, and $\rho v^2 = P_{surf}$ is the external pressure, and V is the total volume. The sum of gravitational energy, energy due to magnetic tension and energy of external pressure must exceed the sum of all pressures counteracting gravity for the MCc to collapse. Thus Equation (1) is re-written as

$$\left|E_g + \rho v^2 V + E_{mt}\right| > 2E_{th} + E_m + 2E_{turb} + 2E_{rot} \tag{2}$$

The coefficient 2 for total kinetic energy (where $E_{ktot} = E_{th} + E_{turb} + E_{rot}$) shows half of the gravitational energy goes to total kinetic energy during MC collapse. In this process tremendous amount of gravitational energy is released and taken away via mechanisms of energy transport. The gravitational energy released raises temperature of the core and kinematics of the particles in the gas cloud. Half the gravitational energy is released in the form of radiation and half of it rises temperature, kinematics and tend the cloud to rotate. Thus rotation also plays its own role in supporting the cloud core as well as determining critical mass of the cloud. In this paper we do not consider external pressure because the source of external pressure is violent explosions like supernova, which we can not specify its equation for the time being. Therefore we focus on energies or pressures, which we can formulate their equations. Since gravitational energy released when a MC of mass M and radius R collapses is given by

$$E_g = -c_g \frac{GM^2}{R} \tag{3}$$

where $c_g = 3/5$ is gravitational constant for spherical cloud. In the same manner rotational energy is written as

$$E_{rot} = c_{rot} MR^2 \Omega^2 \tag{4}$$

where M is mass of the rotating cloud core, R is its radius, Ω is its angular velocity and $c_{rot} = \frac{1}{5}$ is rotational constant. In this study we assume angular velocity that depends on mass distribution. In other way turbulent energy of the cloud of mass M with turbulent velocity dispersion is given by

$$E_{turb} = \frac{1}{2} M \sigma^2 \tag{5}$$

where σ is three-dimensional velocity dispersion given by

$$\sigma^2 = \sigma_r^2 + \sigma_\theta^2 + \sigma_\phi^2 \tag{6}$$

In this study we consider isotropic velocity dispersion, hence for isotropic velocity dispersion $\sigma_r^2 = \sigma_\theta^2 = \sigma_\phi^2$, where σ_r^2 is the radial velocity dispersion and it is the only one we can measure (the other two are perpendicular to our line of sight). Therefore

$$\sigma^2 = 3\sigma_r^2 \tag{7}$$

whereas the known equation of thermal energy is written as

$$E_{th} = \frac{3}{2} \frac{k_B TM}{m_u \mu} \tag{8}$$

Now neglecting external pressure from Equation (2) and using Equations (3), (4), (5) & (8) we rewrite Equation (2) as

$$\left| E_g + E_{mt} \right| > M\sigma^2 + 2c_{rot} MR^2 \Omega^2 + E_m + 3\frac{k_B TM}{m_u \mu} \tag{9}$$

where K_B is the Boltzmann constant, T is temperature of the cloud, m_u and μ are atomic mass unit and mean molecular weight of the gas in atomic mass unit.

Magnetic Pressure & Magnetic Tension

One of the most fundamental questions in astrophysics is how do stars form [17]. Observations clearly show that this process takes place in self-gravitating, turbulent, magnetized filamentary molecular clouds (for more clarification see [18]). However, the question of how magnetic tension supports gravity in collapsing MCc is still largely unanswered. In gravitating, magnetized, turbulent and rotating MC core some energies are counteracting gravity and some are supporting gravity (such as magnetic tension and external pressure). In this study we mainly focus on magnetic tension than external pressure. Equations of those energies can be obtained from their corresponding pressures. Where magnetic pressure is given by

$$P_m = \frac{B^2}{8\pi} \tag{10}$$

Magnetic energy is volume integral of magnetic pressure, so that

$$E_m = \int P_m \mathrm{d}v = \int \frac{B^2}{8\pi} \mathrm{d}v = \frac{1}{8\pi} \int B^2 \mathrm{d}v \tag{11}$$

Integrating Equation (9) over the volume of sphere of MC core leads to

$$E_m = \frac{B_R^2}{6} R^3 \tag{12}$$

This is if the field inside the cloud is much larger than the field outside it. Magnetic field B can be the initial field (seed field) from galaxy. Hence the core inherits magnetic field from its parental MC or clump, thus we consider conservation of magnetic flux. Assuming the total flux threading a given area is a conserved quantity, then

$$B_o R_o^2 = B_R R^2 \tag{13}$$

where B_o and R_o are the magnetic field and radius of the initial or parent cloud which is not yet collapsed; where as B_R is the new magnetic field strength after the sphere of cloud has been compressed slightly to radius *R*. Thus

$$B_R = B_o \left(\frac{R_o}{R} \right)^2 \tag{14}$$

Inserting Equation (14) in Equation (12) we have

$$E_m = \frac{B_o^2 R_o^4}{6R} \tag{15}$$

In actual fact there is an extra term of the same magnitude for the magnetic field strength between R and R_o [19], so that the magnetic energy is

$$E_m = \frac{B_o^2 R_o^4}{3R} \tag{16}$$

Assuming radius of curvature of the magnetic field line extends over the core radius. Therefore,finally magnetic energy of a molecular cloud of radius R_o collapsing to a cloud core of $R = R_{core}$ is written as

$$E_m = \frac{B_o^2 R_o^4}{3R_{core}} \tag{17}$$

We apply this equation (Equation (17)) for our next work. On the other hand, there is a magnetic curvature force pointing toward its center of curvature; there is a restoring force called magnetic tension force, which is caused by magnetic field lines extended over a given radius of curvature and is given by

$$T_m = \frac{B^2}{4\pi} \tag{18}$$

Magnetic tension is the restoring force due to magnetic field line over its radius of curvature. Then magnetic tension acts to straighten bent magnetic field lines. To obtain magnetic energy due to its tension we integrate Equation (18) over the radius dr of the spherical cloud core as

$$E_{mt} = \int T_m \mathrm{d}r = \int_0^{R_B} \frac{B^2}{4\pi} \mathrm{d}r \tag{19}$$

We assume the radius of curvature of the magnetic field line extends over the cloud core radius ($R_B \Rightarrow R_{core} \sim R$ in our expression). Thus we have

$$E_{mt} = \frac{B_R^2}{4\pi} R_{core} \tag{20}$$

Using conservation of flux, and thus inserting Equation (14) in Equation (20) we have

$$E_{mt} = \frac{B_o^2 R_o^4}{4\pi R^3} \tag{21}$$

As cloud core collapses from radius R_o to R the field strength increases so that, we assume, there is an extra magnetic tension term of the same magnitude for the magnetic tension between R and R_o. Therefore, energy due to magnetic tension, which is directed towards centre of curvature of B is redefined as

$$E_{mt} = \frac{B_o^2 R_o^4}{2\pi R^3} \tag{22}$$

This is energy due to magnetic tension over a given radius of curvature which supports gravitational energy in collapsing MC core and dilutes magnetic pressure as much as possible. If B_o has larger radius of curvature than B, therefore, B_o has larger restoring force due to tension. This energy acts to straighten bent magnetic field lines, simultaneously it enhances the inflow of matter. So that, it is important in collapsing molecular cloud to form star. This is why we define magnetic tension is a gravity supporting force in star formation.

3. Results & Discussions

The Critical Mass

Critical mass of the molecular cloud is the minimum amount of mass needed by the cloud to collapse and form star. In this section we formulate the critical mass of gravitating, turbulent, magnetized and rotating molecular cloud core by incorporating magnetic tension. Now plugging Equations (17) and (22) in Equation (9) we have

$$\begin{aligned} \left| \frac{3GM_{core}^2}{5R_{core}} + \frac{B_o^2 R_o^4}{2\pi R_{core}^3} \right| > M_{core}\sigma^2 + \frac{3k_B T_{core} M_{core}}{\mu m_H} \\ + 2c_{rot} M_{core} \left(R_{core} \Omega_{core} \right)^2 + \frac{B_o^2 R_0^4}{3R_{core}} \end{aligned} \tag{23}$$

where M_{core} & R_{core} are the mass and radius of the collapsing cloud core respectively. From Equation (23) we have

$$\begin{aligned} \frac{GM_{core}^2}{R_{core}} > \frac{5}{3} M_{core}\sigma^2 + \frac{5k_B T_{core} M_{core}}{\mu m_H} + \frac{10}{3} c_{rot} M_{core} \left(R_{core} \Omega_{core} \right)^2 \\ + \frac{5}{9} \frac{B_o^2 R_0^4}{R_{core}} - \frac{5}{6} \frac{B_o^2 R_o^4}{\pi R_{core}^3} \end{aligned} \tag{24}$$

Multiplying both sides of Equation (24) by R_{core} and considering spherical core of mass $M_{core}=\frac{4}{3}\pi R_{core}^3\rho_{core}$ as well as substituting $R_{core}=3M_{core}\Big/\left(R_{core}^2 4\pi\rho_{core}\right)$ we arrive at

$$M_{core}^2>\frac{5R_{core}}{3G}M_{core}\sigma^2+\frac{5R_{core}k_BT_{core}M_{core}}{G\mu m_H}+\frac{10R_{core}^3}{3G}c_{rot}M_{core}\Omega_{core}^2+\frac{5B_o^2R_o^4 3M_{core}}{4\pi G\rho_{core}R_{core}^2}\left(\frac{1}{9R_{core}}-\frac{1}{6\pi R_{core}^3}\right) \tag{25}$$

Simplifying the last two terms we have

$$M_{core}^2>\frac{5R_{core}}{3G}M_{core}\sigma^2+\frac{5R_{core}k_BT_{core}M_{core}}{G\mu m_H}+\frac{10R_{core}^3}{3G}c_{rot}M_{core}\Omega_{core}^2+\frac{5B_o^2R_o^4M_{core}}{4\pi G\rho_{core}R_{core}^2}\left(\frac{1}{3R_{core}}-\frac{1}{2\pi R_{core}^3}\right) \tag{26}$$

Dividing both sides of Equation (26) by M_{core} and taking out R_{core} from the last terms we arrive at

$$M_{core}>\frac{5R_{core}}{3G}\sigma^2+\frac{5R_{core}k_BT_{core}}{G\mu m_H}+\frac{10R_{core}^3}{3G}c_{rot}\Omega_{core}^2+\frac{5B_o^2R_o^4}{4\pi G\rho_{core}R_{core}^3}\left(\frac{1}{3}-\frac{1}{2\pi R_{core}^2}\right) \tag{27}$$

We assume isotropic turbulent velocity dispersion σ, which is given by $\sigma^2=\sigma_r^2+\sigma_\theta^2+\sigma_\phi^2$, hence for isotropic velocity dispersion $\sigma^2=3\sigma_r^2$, where σ_r^2 is the radial velocity dispersion the only one we can measure (the other two are perpendicular to our line of sight). Thus Equation (27) becomes

$$M_{core}>\frac{5R_{core}}{G}\sigma_r^2+\frac{5R_{core}k_BT_{core}}{G\mu m_H}+\frac{10R_{core}^3}{3G}c_{rot}\Omega_{core}^2+\frac{5B_o^2R_o^4}{4\pi G\rho_{core}R_{core}^3}\left(\frac{1}{3}-\frac{1}{2\pi R_{core}^2}\right) \tag{28}$$

Now substituting $\rho_{core}=n_{core}\mu m_H$

$$M_{core}>\frac{5R_{core}}{G}\sigma_r^2+\frac{5R_{core}k_BT_{core}n_{core}}{G\rho_{core}}+\frac{10R_{core}^3}{3G}c_{rot}\Omega_{core}^2+\frac{5B_o^2R_o^4}{4\pi G\rho_{core}R_{core}^3}\left(\frac{1}{3}-\frac{1}{2\pi R_{core}^2}\right) \tag{29}$$

By rearranging Equation (29) we get

$$M_{core}>\frac{5R_{core}}{G}\left(\frac{k_BT_{core}n_{core}}{\rho_{core}}+\sigma_r^2\right)+\frac{10R_{core}^3}{3G}c_{rot}\Omega_{core}^2+\frac{5B_o^2R_o^4}{4\pi G\rho_{core}R_{core}^3}\left(\frac{1}{3}-\frac{1}{2\pi R_{core}^2}\right) \tag{30}$$

Hence the gas pressure from equation of state is given by

$$P_g=n_{core}K_BT_{core} \tag{31}$$

where n_{core} is particle number density of the core, K_B is the Boltzmann constant and T_{core} is core temperature. Then, using Equation (31) we have

$$M_{core} > \frac{5R_{core}}{G}\left(\frac{P_g\left(\rho_{core}\right)}{\rho_{core}} + \sigma_r^2\right) + \frac{10R_{core}^3}{3G} c_{rot}\Omega_{core}^2 + \frac{5B_o^2 R_o^4}{4\pi G\rho_{core} R_{core}^3}\left(\frac{1}{3} - \frac{1}{2\pi R_{core}}\right) \tag{32}$$

The core can collapse & form the star if the condition in Equation (32) satisfied. But it expands if

$$M_{core} < \frac{5R_{core}}{G}\left(\frac{P_g\left(\rho_{core}\right)}{\rho_{core}} + \sigma_r^2\right) + \frac{10R_{core}^3}{3G} c_{rot}\Omega_{core}^2 + \frac{5B_o^2 R_o^4}{4\pi G\rho_{core} R_{core}^3}\left(\frac{1}{3} - \frac{1}{2\pi R_{core}^2}\right) \tag{33}$$

Finally, the critical mass of gravitating, magnetized, turbulent, and rotating star-forming molecular cloud core in the presence of magnetic tension is formulated as

$$M_{crt} = \frac{5R_{core}}{G}\left(\frac{P_g\left(\rho_{core}\right)}{\rho_{core}} + \sigma_r^2\right) + \frac{10R_{core}^3}{3G} c_{rot}\Omega_{core}^2 + \frac{5B_o^2 R_o^4}{4\pi G\rho_{core} R_{core}^3}\left(\frac{1}{3} - \frac{1}{2\pi R_{core}^2}\right) \tag{34}$$

where M_{crt} is the critical mass of magnetized MC core. The core mass has to exceed this critical mass to collapse and form star. Equation (34) is the critical core mass explained in general way. Recent studies show average values of the magnetic field of molecular cloud is ≈5 - 15 μG [20] [21]. We use the average of this magnetic field in our calculation. Since angular speed of molecular cloud is approximated to 10^{-15} s^{-1} - 10^{-13} s^{-1}. For instance, given a pre-stellar core of initially collapsing MC (parent cloud) rotating with $\Omega_{core} = 10^{-13}\ s^{-1}$, depends on mass distribution, $c_{rot} = 1/5$, $R_{core} = 0.01\,pc$, R_o is radius of parent MC ~ 1pc, $\rho_{core} = 10^{-10}\ kg\cdot m^3$, typical MC magnetic field $B_o = 10\,\mu G$, speed of sound $c_s = 332\ m\cdot s^{-s}$, assuming supersonic turbulent velocity dispersion $\sigma \sim 400\ m\cdot s^{-1}$, we find the critical mass of this MC is ~ $33.743M_{\odot}$, beyond this mass the MC core becomes supercritical. Due to this reason the cloud core collapses and can form star. This confirms that properties of the parent cloud governs the critical mass of molecular cloud core. The role of rotation is displayed in **Figure 1** when the core rotates rapidly the cloud supporting pressures increase, so that the cloud must contain large mass within small size to collapse. The critical mass is lower at $R_{core} = 0.2$ pc in **Figure 1**, it may be the minimum critical mass required in order to collapse for the MCc under consideration. Above this radius it needs larger MCc mass to collapse and form star. We understand that from **Figure 2** outflow from the core disperses gases and dusts near to the surface of the protostar. At this stage stellar wind also made the circumstellar disk to disperse. Far away from the core those dispersed

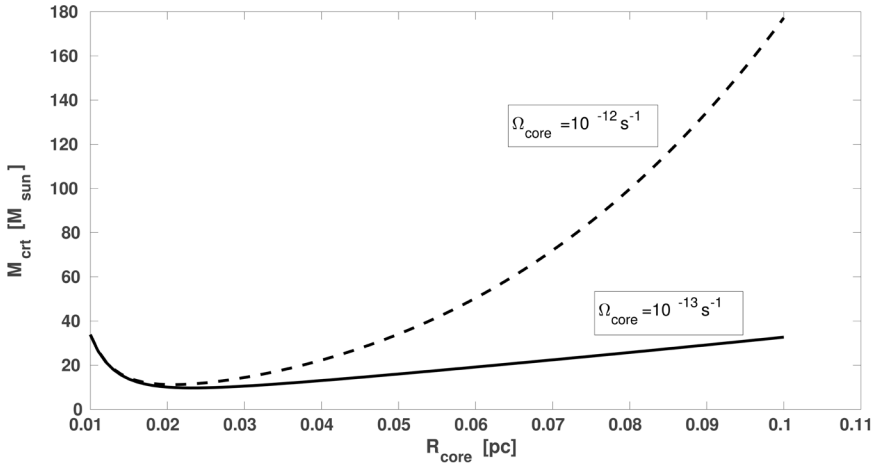

Figure 1. The pre-stellar core radius vs its relative critical mass (M_{crt}). With parent MC radius $R_o = 1\,\mathrm{pc}$, $R_{core} = 0.01\,\mathrm{pc}$ - $0.1\,\mathrm{pc}$, $c_s = 332\,\mathrm{m}\cdot\mathrm{s}^{-1}$, $B_{core} = 10\,\mu\mathrm{G}$, $\rho_{core} = 10^{-10}\,\mathrm{kg}\cdot\mathrm{m}^{-3}$, and $\sigma_r = 400\,\mathrm{m}\cdot\mathrm{s}^{-1}$. The figure shows high angular velocity results in larger critical mass. This figure is plotted making use of Equation (34). This figure shows to overcome the pressure of rotation the MCc mass has to be relatively larger to collapse.

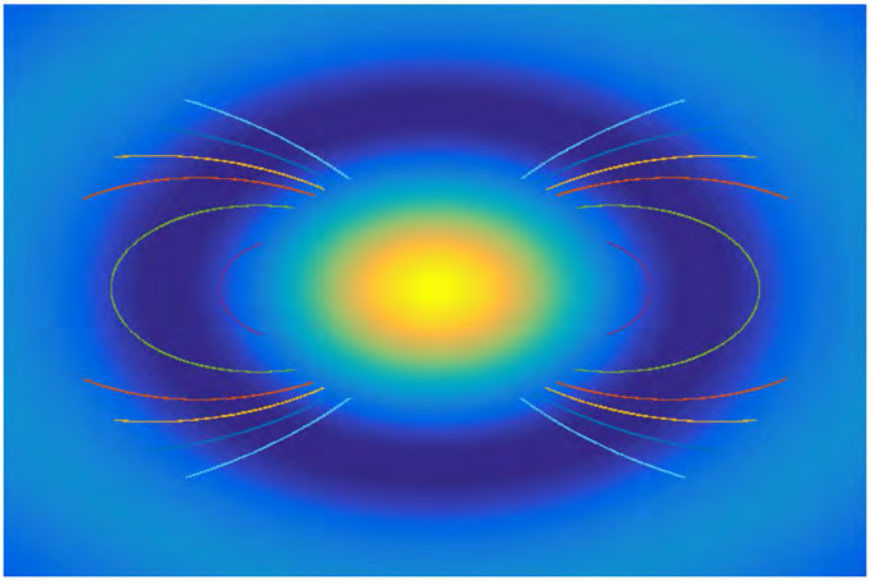

Figure 2. When magnetic field lines stretched over its radius of curvature. Here, the protostar grows to pre-main sequence star. Simulated using vertical structure and disk radius where $\sin\theta = g_z/g$ is the angle between the horizontal and core's gravity (g), where as g_z is the vertical component of the core's gravity. Dipolar magnetic field line equation is used to simulate the field lines. This figure is just to show the importance of magnetic tension how it holds the central core and its envelope together.

materials condense and coagulate. A strong stellar wind breaks out at the rotational poles, reversing the infall and producing bipolar outflows. This phase is connected with the disk formation phase. Then after the newly formed star/disk system becomes optically visible and the protostar is identified as a T

Tauri star or Low mass ($M < 2M_{\odot}$) young stellar objects (YSOs) [22] [23].

Magnetic field line extends out of the central protostar radius this helps to hold the protoplanetary disc and the central stellar object (see **Figure 2**). Therefore, if there is strong magnetic tension the disc may not escape from the star and has great chance to form planets. Of course the strength and geometry of magnetic fields implanted in protostars during the star formation process is unknown [8]. However, we use dipolar field lines for simplicity, and to show how magnetic tension is playing a crucial role in star formation. As the protostar collapses and rotates the field lines are twisted into helical shapes. Then drawing the field lines closer together results in strong field and the twisting of the field causes torsional Alfve'n waves to travel along the field lines, like torsional waves on a string. The magnetic field is responsible for carrying away excess angular momentum by being tied to the surrounding envelope. We show in **Figure 3** & **Figure 4** the minimum critical mass is $M_{mincrt} \approx 5.6290 M_{\odot}$ in the presence of all possible energies in our model (Equation (34)) for those specified conditions. If there is no magnetic tension the minimum critical mass is beyond the value we get here, *i.e.* $M_{mincrt} > 5.6290 M_{\odot}$.

4. Critical Mass in Different Cases

In this section, we consider different cases to see how conditions can vary the critical mass of a star-forming MCc. In our assumptions, the initial condition for sound speed in MCc is $c_s \approx 200\ \mathrm{s}^{-1}$ [24] and the supersonic turbulent velocity dispersion is greater than 332 m·s^{-1}.

Case I: *For* $1/2\pi R_{core}^2 \Rightarrow 0$

If the core is very large in size the ratio of $\dfrac{1}{R_{core}^2}$ approaches to zero. So that

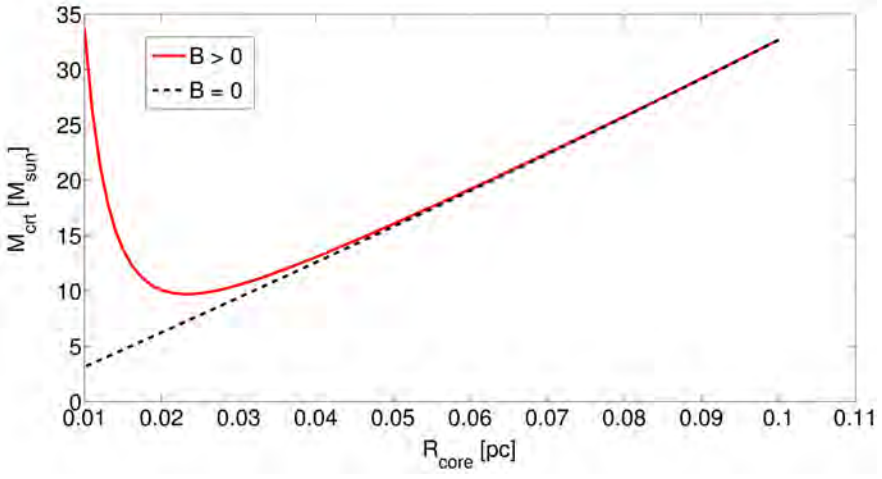

Figure 3. The pre-stellar core radius vs its relative critical mass (M_{crt}). Assuming parent MC radius $R_o = 1\,\mathrm{pc}$, $\Omega_{core} \sim 10^{-13}\ \mathrm{s}^{-1}$, $R_{core} = 0.01\,\mathrm{pc}$ - $0.1\,\mathrm{pc}$, $c_s = 332\ \mathrm{m \cdot s}^{-1}$, $\rho_{core} = 10^{-10}\ \mathrm{kg \cdot m}^{-3}$, and $\sigma_r = 400\ \mathrm{m \cdot s}^{-1}$. The red solid line is for the magnetized parent cloud core whereas the black broken line is for unmagnetized MC core. The figure is plotted from Equation (34) (the red curve) and Equation (36) (the black broken line).

we omit the last term of Equation (34) in parenthesis. It is almost approaches to zero ($1/2\pi R_{core}^2 \Rightarrow 0$) and has no significant effect unless the core radius is too small. Due to this reason Equation (34) becomes

$$M_{crt} = \frac{5R_{core}}{G}\left(\frac{P_g\left(\rho_{core}\right)}{\rho_{core}} + \sigma_r^2\right) + \frac{10R_{core}^3}{3G}c_{rot}\Omega_{core}^2 + \frac{5}{12\pi G}\frac{B_o^2 R_o^4}{\rho_{core}R_{core}^3} \tag{35}$$

If a core is very large in size its critical mass can be calculated using Equation (35). This kind of core has to be denser and massive to collapse.

Case II: *For* $B_o \Rightarrow 0$

This condition is for unmagnetized MC if it exists. Or when the influence of magnetic pressure and tension is insignificant. Thus Equation (34) becomes

$$M_{crt} = \frac{5R_{core}}{G}\left(\frac{P_g\left(\rho_{core}\right)}{\rho_{core}} + \sigma_r^2\right) + \frac{10R_{core}^3}{3G}c_{rot}\Omega_{core}^2 \tag{36}$$

A non-magnetized cloud core's critical mass depends mainly on density, radius and angular speed. If the core is denser, small in size and slow rotating it can collapse, even if it has small mass according to Equation (36).

Case III: *For* $\Omega_o \Rightarrow 0$

If magnetized turbulent cloud core is not rotating $\Omega_{core} = 0$. Then its critical mass is expressed as

$$M_{crt} = \frac{5R_{core}}{G}\left(\frac{P_g}{\rho_{core}} + \sigma_r^2\right) + \frac{5B_o^2 R_o^4}{4\pi G\rho_{core}R_{core}^3}\left(\frac{1}{3} - \frac{1}{2\pi R_{core}^2}\right) \tag{37}$$

This situation describes a non-rotating cloud core's critical mass. Here the role of magnetic tension is significant to protect the cloud from dispersing.

Case IV: *For* σ_r & $\Omega_{core} \Rightarrow 0$

This condition explains where there is a probability of getting non-turbulent and non-rotating, but magnetized and gravitating molecular cloud core. For this case Equation (34) becomes

$$M_{crt} = \frac{5R_{core}}{G}\left(\frac{P_g\left(\rho_{core}\right)}{\rho_{core}}\right) + \frac{5B_o^2 R_o^4}{4\pi G\rho_{core}R_{core}^3}\left(\frac{1}{3} - \frac{1}{2\pi R_{core}^2}\right) \tag{38}$$

Case V: *For* σ_r, Ω_{core} & $B_o \Rightarrow 0$

In this case gravity left alone to trigger MC to collapse. For this condition Equation (34) becomes

$$M_{crt} = \frac{5R_{core}}{G}\left(\frac{P_g\left(\rho_{core}\right)}{\rho_{core}}\right) \tag{39}$$

From both cases (case I to case V) we clearly understand that star formation process depends on varies parameters and physical conditions in addition to magnetic tension. Therefore, understanding factors affecting critical mass of the MCc will provide some idea for star formation theory. In this paper, we formulated five different equations of critical mass from the basic model (Equation (34)). Then those equations are useful to calculate the critical mass of star-forming cloud core. In rare case if there are no gravity opposing pressures

the minimum critical mass we obtained is $\approx 0.4617 M_{\odot}$ (shown by the black line in Figure 7). These show how critical mass of star-forming MC depends on different dynamical process and conditions. However, the minimum critical mass contained in different radius of the core is quite different from one another regardless of having the same ρ, B, σ_r and Ω. This means that there is a specified critical mass for each radius of the core (example see Figures 4-7).

The blue curve in Figure 7 indicates near the center of the core magnetic pressure is extremely high, so that the cloud has to be massive and more dense to collapse. But as radius the increases the corresponding critical mass reduces,

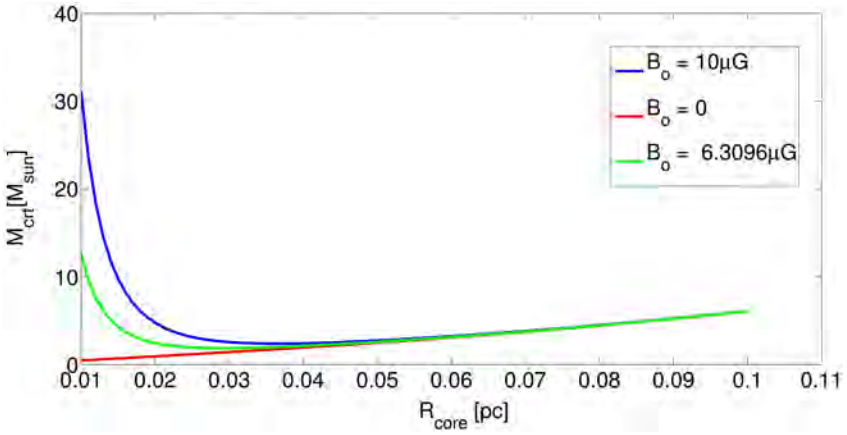

Figure 4. Critical mass comparison of unmagnetized and magnetized, but rotating and turbulent MC core. At a point far from the center of the core (relatively larger radius) magnetic pressure is dominated by magnetic tension plus gravity. Thus the graphs overlap after $R_{core} \gtrsim 0.05$ pc in this particular case. With parent MC radius $R_o = 1$ pc, $c_s = 200\ \mathrm{m \cdot s^{-1}}$, $\rho_{core} = 10^{-10}\ \mathrm{kg \cdot m^{-3}}$, and $\sigma_r = 300\ \mathrm{m \cdot s^{-1}}$. It is Plotted from Equation (34) (the blue and green curves) and Equation (36) (the red line).

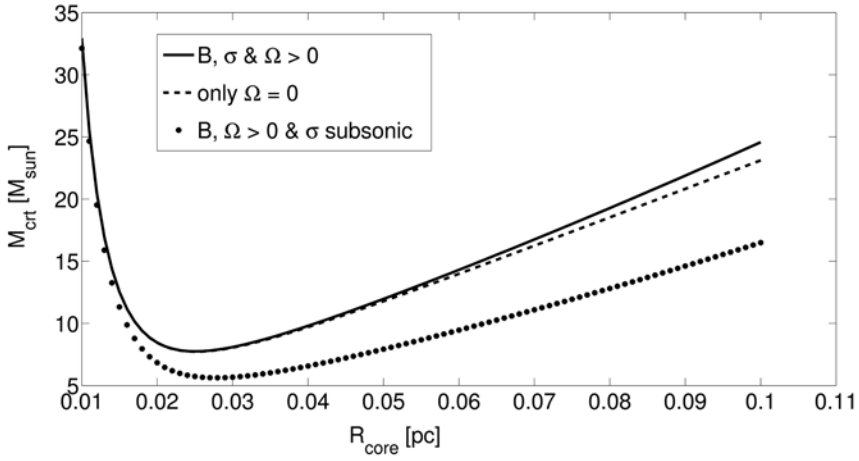

Figure 5. Critical mass versus radius of the core for different conditions. With parent MC radius $R_o = 1$ pc, $c_s = 200\ \mathrm{m \cdot s^{-1}}$, $B_{core} = 10\ \mu\mathrm{G}$, $\rho_{core} = 10^{-10}\ \mathrm{kg \cdot m^{-3}}$, $\Omega_{core} = 10^{-13}\ \mathrm{s^{-1}}$, we assume $\sigma_r = 400\ \mathrm{m \cdot s^{-1}}$ for supersonic (in solid and dashed lines) and $\sigma_r = 300\ \mathrm{m \cdot s^{-1}}$ for subsonic indicated in the doted line. Plotted from Equation (34) (the black solid line and black dotted line) and Equation (37) (the black broken line).

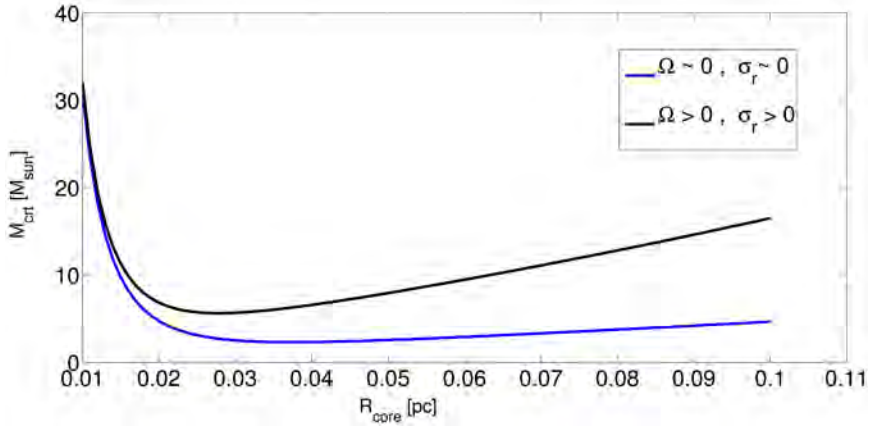

Figure 6. Critical mass comparison of non-turbulent and non-rotating, but magnetized MCc (the black curve) with turbulent and rotating magnetized MCc (the blue curve). Assuming parent MC radius $R_o = 1\,\text{pc}$, $c_s = 200\,\text{m}\cdot\text{s}^{-1}$, $B_{core} = 10\,\mu\text{G}$, $\Omega_{core} = 10^{-13}\,\text{s}^{-1}$, $\rho_{core} = 10^{-10}\,\text{kg}\cdot\text{m}^{-3}$, and $\sigma_r = 300\,\text{m}\cdot\text{s}^{-1}$. The figure is plotted using Equation (34) (black curve) and Equation (38) (blue curve). The black curve in **Figure 6** shows how the existence of rotation and turbulence create difference in critical mass. Where as near the center of the core magnetic pressure dominates magnetic tension.

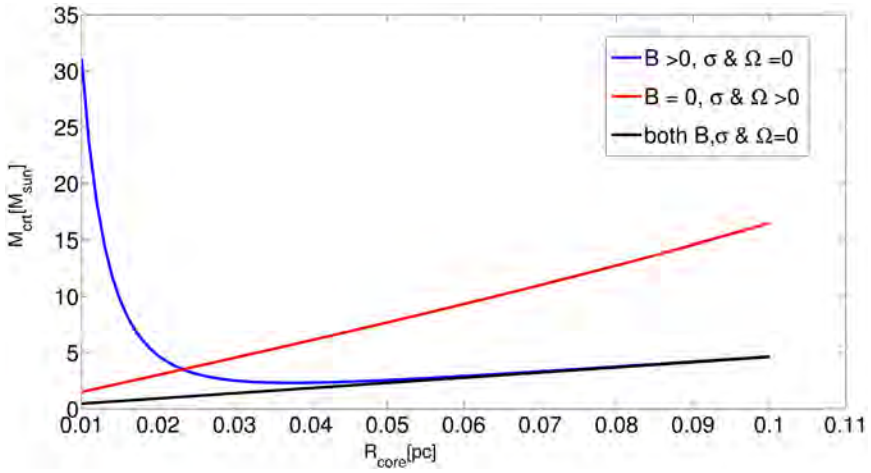

Figure 7. The core requires relatively low critical mass compared to other conditions. With parent MC radius $R_o = 1\,\text{pc}$, $R_{core} = 0.01\,\text{pc}$ - $0.1\,\text{pc}$, $c_s = 200\,\text{m}\cdot\text{s}^{-1}$, $\rho_{core} = 10^{-10}\,\text{kg}\cdot\text{m}^{-3}$, $\sigma_r = 300\,\text{m}\cdot\text{s}^{-1}$ for subsonic turbulent velocity. The figure is plotted using Equation (38) (blue curve), Equation (36) (red line) and Equation (39) (black line).

because as the radius of curvature increases magnetic tension increases. The point at which the blue and red curves cross each other is the point (radius) at which magnetic field effect is equal to the effect of turbulence plus rotation. At the same time, the red line shows as radius increases critical mass also slightly increases, and the curve has positive slope, this tells us no magnetic tension as $B = 0$. Therefore, gravity struggles alone to bring matter from the envelope to the central core. Thus the black line in **Figure 7** shows the only dominating energy is gravitational energy, due to this the graph attains positive slope and the smallest critical mass at smaller radius than other cases.

The blue curve in Figure 7 confirms how strong magnetic pressure is near the center of the core and being diluted by magnetic tension plus gravity at a point far from the center. Fortunately if the cloud is not magnetized but rotating and turbulent, we obtain the graph of radius versus critical mass with positive slope (see red curve in Figure 7). As indicated in Figure 8 a highly supersonic turbulent cloud core has to contain very large mass within a small radius to collapse, but this small radius can not hold the amount of masses indicated by the black dashed line in this figure, which is out of reality, therefore, magnetized and highly supersonic cloud may not collapse before cloud life time. However, it seems realistic for subsonic turbulence *i.e.* indicated by the red line in this figure. For dense regions in cold molecular clouds of $c_s = 0.2\ \mathrm{km\cdot s^{-1}}$, $B_o = 30\ \mu\mathrm{G}$ and $r = 0.05\ \mathrm{pc}$ it has been found that the initial core mass $M_o = 1.5 M_\odot$ [25]. However, turbulence and rotation were not considered by [25] in his particular finding. Nevertheless, we interpret our findings using simple energy balance equations by incorporating gravity, thermal, rotation, turbulence, magnetic pressure and magnetic tension. In Table 1 different critical masses have been displayed because all possible pressures except external pressure have been incorporated in our model (Equation (34)), and then critical masses are calculated for different conditions (as shown in Table 1).

Numerical Results of Magnetic Field from Literature for Comparison

Magnetic fields of the line of sight for OMC B (Orion molecular cloud B) and CMC (California molecular cloud) has been measured using rotation measure data from the literature [26]. The Orion molecular cloud (OMC) is a well-studied, active star-forming region. CMC is also a giant molecular cloud, but with relatively little star formation activity. This indicates the combination of

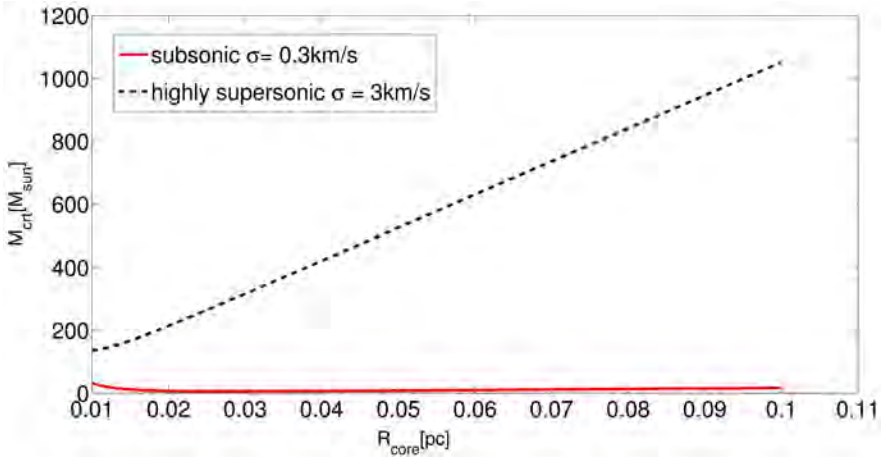

Figure 8. Critical mass comparison of magnetized turbulent subsonic and highly supersonic velocity dispersion. Assuming parent MC radius $R_o = 1\ \mathrm{pc}$, $c_s = 300\ \mathrm{m\cdot s^{-1}}$, $B_{core} = 10\ \mu\mathrm{G}$, $\Omega_{core} = 10^{-13}\ \mathrm{s^{-1}}$, $\rho_{core} = 10^{-10}\ \mathrm{kg\cdot m^{-3}}$, and $\sigma_r = 3000\ \mathrm{m\cdot s^{-1}}$. The graph can be plotted from Equation (34) using the specified conditions.

Table 1. Calculated critical masses of molecular cloud cores in different conditions. Assuming $R_o = 1\,\mathrm{pc}$, $c_s = 200\,\mathrm{m\cdot s^{-1}}$, $B_{core} = 10\,\mu\mathrm{G}$, $\Omega_{core} = 10^{-13}\,\mathrm{s^{-1}}$, $\rho_{core} = 10^{-10}\,\mathrm{kg\cdot m^{-3}}$, with temperature ($T$) ~ 10 K and $\sigma_r = 300\,\mathrm{m\cdot s^{-1}}$ (subsonic) for the case of magnetized, rotating, turbulent molecular cloud core.

R_{core}/pc	$B,\Omega,\sigma \neq 0$	$B=0$ & $\Omega,\sigma \neq 0$	$B \neq 0,\sigma = 0,\Omega = 0$	$B=0,\sigma=0,\Omega=0$
	$M_{crt}/M_\odot$	$M_{crt}/M_\odot$	$M_{crt}/M_\odot$	$M_{crt}/M_\odot$
0.01	32.124	1.502	31.084	0.462
0.011	24.660	1.653	23.515	0.508
0.012	19.524	1.803	18.275	0.554
0.013	15.892	1.954	14.538	0.600
0.014	13.265	2.105	11.806	0.646
0.015	11.329	2.256	9.766	0.693
0.016	9.883	2.407	8.215	0.739
0.017	8.791	2.558	7.016	0.785
0.018	7.961	2.710	6.082	0.831
0.019	7.326	2.861	5.342	0.877
0.02	6.841	3.013	4.751	0.923
0.021	6.472	3.165	4.276	0.970
0.022	6.193	3.317	3.892	1.016
0.023	5.986	3.469	3.579	1.062
0.024	5.837	3.622	3.323	1.108
0.025	5.734	3.775	3.114	1.154
0.026	5.670	3.928	2.943	1.201
0.027	5.637	4.081	2.803	1.247
0.028	5.629	4.234	2.688	1.293
0.029	5.643	4.388	2.595	1.339
0.03	5.676	4.542	2.519	1.385
0.031	5.724	4.696	2.459	1.431
0.032	5.785	4.850	2.412	1.478
0.033	5.857	5.005	2.376	1.524
0.034	5.939	5.160	2.349	1.570
0.035	6.029	5.315	2.330	1.616
0.036	6.127	5.471	2.319	1.662
0.037	6.231	5.627	2.313	1.709
0.038	6.341	5.783	2.313	1.755
0.039	6.456	5.395	2.317	1.801
0.04	6.575	6.096	2.325	1.847
0.041	6.698	6.254	2.338	1.893
0.042	6.825	6.411	2.353	1.939

Continued

0.043	6.954	6.569	2.371	1.986
0.044	7.087	6.728	2.391	2.032
0.045	7.222	6.886	2.414	2.078
0.046	7.360	7.046	2.439	2.124
0.047	7.500	7.205	2.465	2.170
0.048	7.642	7.365	2.493	2.216
0.049	7.786	7.525	2.523	2.263
0.05	7.931	7.686	2.554	2.309
0.051	8.078	7.848	2.586	2.355
0.052	8.227	8.009	2.619	2.401
0.053	8.377	8.171	2.653	2.447
0.054	8.528	8.334	2.689	2.494
0.055	8.681	8.497	2.724	2.540
0.056	8.835	8.661	2.760	2.586
0.057	8.990	8.825	2.797	2.632
0.058	9.146	8.989	2.835	2.678
0.059	9.303	9.154	2.873	2.724
0.06	9.462	9.320	2.912	2.771
0.061	9.621	9.486	2.952	2.817
0.062	9.781	9.653	2.991	2.863
0.063	9.942	9.820	3.032	2.909
0.064	10.1044	9.988	3.072	2.955
0.065	10.267	10.156	3.113	3.001
0.066	10.431	10.325	3.154	3.048
0.067	10.596	10.494	3.196	3.094
0.068	10.762	10.664	3.237	3.140
0.069	10.928	10.835	3.279	3.186
0.07	11.095	11.006	3.322	3.232
0.071	11.263	11.178	3.364	3.279
0.072	11.432	11.350	3.407	3.324
0.073	11.602	11.524	3.451	3.371
0.074	11.773	11.697	3.493	3.417
0.075	11.944	11.872	3.536	3.463
0.076	12.116	12.047	3.579	3.509
0.077	12.289	12.222	3.623	3.556
0.078	12.463	12.399	3.666	3.602
0.079	12.638	12.576	3.710	3.648
0.08	12.813	12.754	3.754	3.694

Continued

0.081	12.989	12.932	3.798	3.740
0.082	13.167	13.111	3.842	3.787
0.083	13.343	13.291	3.886	3.833
0.084	13.523	13.472	3.931	3.879
0.085	13.703	13.653	3.975	3.925
0.086	13.883	13.835	4.019	3.971
0.087	14.065	14.018	4.064	4.017
0.088	14.247	14.202	4.109	4.064
0.089	14.429	14.386	4.153	4.110
0.09	14.613	14.571	4.198	4.156
0.091	14.798	14.757	4.2427	4.202
0.092	14.983	14.944	4.288	4.248
0.093	15.169	15.131	4.333	4.294
0.094	15.357	15.321	4.377	4.341
0.095	15.544	15.509	4.423	4.387
0.096	15.733	15.699	4.468	4.433
0.097	15.923	15.899	4.513	4.479
0.098	16.114	16.082	4.558	4.525
0.099	16.306	16.274	4.603	4.571
0.1	16.498	16.468	4.648	4.618

those parameters we have been used in Equation (34) is very important to determine the minimum cloud core mass required for collapse. Since CMC has lower density than Orion [26] For this reason, magnetic pressure dominates gravity plus magnetic tension, this made CMC has lower star formation rate than OMC. Therefore, our model will help to describe why some giant molecular clouds are not active in forming star. Despite their similarity in size and mass, Some molecular clouds are characterized by rates of star formation that differ by more than an order of magnitude [27]. So that our results more securely establish that significant variations in the level of star formation activity and star formation rate are common in magnetized molecular clouds and are dependent on the cloud core magnetic field strength. As a result, it is possible from comparative studies of such clouds to determine the physical factors that govern the star formation rates in molecular clods.

The negative and positive signs in **Figure 9** & **Figure 10** indicate magnetic field directed away from the observer and magnetic field toward the observer respectively. This comparison is just to see how critical mass depends on dynamical process & parameters including magnetic field. Thus our result has its own contribution in building star formation theory. Even so, the author ([26])

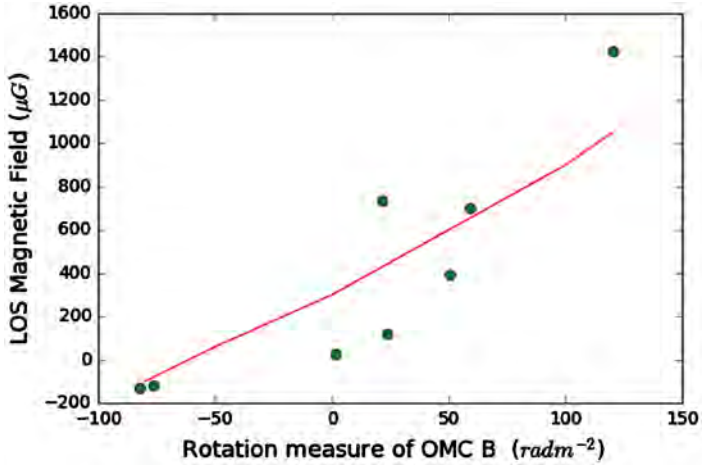

Figure 9. Line of sight (LOS) magnetic field of OMC B (Orion molecular cloud B) versus Rotation measure of Molecular Cloud (RMmc) J2000. RMmc is the rotation measure of the molecular cloud alone as described in literatures [26]. The graph is plotted using data available online and obtained from J/A + A/614/A100 [26]. Green circles indicate the magnitude of magnetic field of the cloud at its corresponding rotation measure.

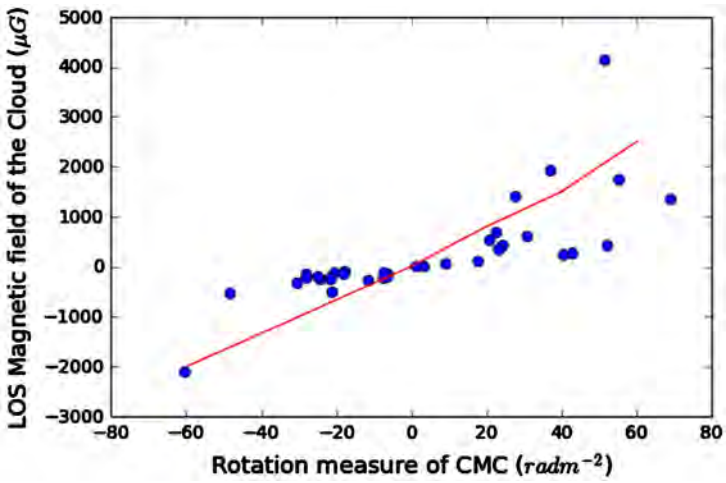

Figure 10. Line of sight (LOS) magnetic field of CMC (California molecular cloud) versus Rotation measure of Molecular Cloud (RMmc) J2000. The graph is plotted using data available online and obtained from J/A + A/614/A100 [26]. RMmc is the rotation measure of the molecular cloud alone. Blue circles indicate the magnitude of magnetic field of the cloud at its corresponding rotation measure.

did not calculate the critical mass of those molecular clouds with respect to their magnetic field strength. Rather they measured magnetic fields of the line of sight using rotation measure data.

5. Conclusions

Star formation in magnetized, turbulent and rotating MC may take longer time unless magnetic tension supports gravity. The minimum core mass required to collapse, and form star can be calculated for different conditions. Indeed, the model indicates magnetic tension has also its own role in protecting cloud

dissipation. If the role of magnetic tension is negligible, the core would take longer time than cloud life time to collapse, which results in non-star-forming region. In other way, for the case of no magnetic tension, turbulence has to decay before the free fall time, then the core collapses in time to form star. This implies there is a competition between turbulence and magnetic tension. Our findings confirm that the interplay among many dynamical processes made too difficult to fix the critical mass, unless we know the properties of the environment in which the star-forming cloud resides. Recent observations confirmed that there are non-star-forming giant molecular clouds. Therefore, our model displays some reasons to answer the question why some clouds do not form star through identifying the role of magnetic pressure and tension of magnetic field lines.

Strong magnetic pressure causes dissipation of the cloud through ambipolar diffusion (slow drift of neutral particles across magnetic field lines) and forbidding the infall of matter from the envelope. In addition, rotation also supports magnetic pressure, the faster the envelope rotates around central core the more difficult for the core to gain mass. We have shown to what extent each energy pressure determines the critical mass of star-forming MC core (see **Figures 2-8** and **Table 1**). These figures indicate how magnetic pressure is too strong at relatively inner radius of the core, and results in the necessity of larger critical mass for MCc to collapse and form star. In **Figure 7**, we show magnetic tension has significant role in supporting gravity at a point far from the center of the core. Thus at a great distance from the center of the core, magnetic pressure is diluted by the sum of magnetic tension and gravity. This is why the blue curve and black line overlap in **Figure 7** at $R_{core} \gtrsim 0.05\,\mathrm{pc}$ for this particular situation. In general, we model critical mass of star-forming molecular cloud core in different cases by involving magnetic tension at the beginning. According to our view, where there is magnetic field in star-forming cloud core there is also unavoidable magnetic tension.

Acknowledgements

We thank Ethiopia Space Science and Technology Institute (ESSTI), Entoto Observatory and Research Center (EORC) for providing this research opportunity. Our gratitude also goes to International Science Programme (ISP) for supporting this study. We also acknowledge with thanks the anonymous reviewers for their constructive comments as well as [26] for making their data publicly available online for scientific community. G.M. Kumssa, thanks Jimma University for permitting study leave.

Conflicts of Interest

The authors declare no conflicts of interest regarding the publication of this paper.

References

[1] Larson, R.B. (1991) Fragmentation of Molecular Clouds and Star Formation (IAU Symp. 147). In: Falgarone, E. *et al*., Eds., Kluwer, Dordrecht, 261-273.

[2] Bertram, *et al*. (2016) Synthetic Observations of Molecular Clouds in a Galactic Centre Environment-I. Studying Maps of Column Density and Integrated Intensity. *MNRAS*, **455**, 3763.

[3] Scalo, J.M. (1985) Protostars and Planets II ed D C Black and M S Matthews. University of Arizona Press, Tucson, 201-296.

[4] Gregory, S.G., Jardine, M., Gray, C.G. and Donati, J.F. (2010) The Magnetic Fields of Forming Solar-Like Stars. *Reports on Progress in Physics*, **73**, 126-901. https://doi.org/10.1088/0034-4885/73/12/126901

[5] Hosking, J.G. and Whitworth, A.P. (2004) Fragmentation of Magnetized Cloud Cores. *MNRAS*, **347**, 1001-1010. https://doi.org/10.1111/j.1365-2966.2004.07274.x

[6] Boss, A.P. (2002) Collapse and Fragmentation of Molecular Cloud Cores. VII. Magnetic Fields and Multiple Protostar Formation. *ApJ*, **568**, 743. https://doi.org/10.1086/339040

[7] Larson, R.B. (1969) Numerical Calculations of the Dynamics of a Collapsing Proto-Star. *Monthly Notices of the Royal Astronomical Society*, **145**, 271-295. https://doi.org/10.1093/mnras/145.3.271

[8] Bate, M.R., Tricco, T.S. and Price, D.J. (2014) Collapse of a Molecular Cloud Core to Stellar Densities: Stellar-Core and Outflow Formation in Radiation Magnetohydrodynamic Simulations. *MNRAS*, **437**, 77-95. https://doi.org/10.1093/mnras/stt1865

[9] Whitehouse, S.C., Bate, M.R. and Monaghan, J.J. (2005) A Faster Algorithm for Smoothed Particle Hydrodynamics with Radiative Transfer in the Flux-Limited Diffusion Approximation. *MNRAS*, **364**, 1367-1377. https://doi.org/10.1111/j.1365-2966.2005.09683.x

[10] Tricco, T.S. and Price, D.J. (2012) Constrained Hyperbolic Divergence Cleaning for Smoothed Particle Magnetohydrodynamics. *Journal of Computational Physics*, **231**, 7214-7236. https://doi.org/10.1016/j.jcp.2012.06.039

[11] Elmegreen, B.G. (2000) Star Formation in a Crossing Time. *The Astrophysical Journal*, **530**, 277-281. https://doi.org/10.1086/308361

[12] Elmegreen, B.G. and Palou's, J., Eds. (2007) Triggered Star Formation in a Turbulent ISM. *Proceedings of the International Astronomical Union Symp.* 237, Cambridge University Press, Cambridge.

[13] (2016) Mordecai-Mark Mac Low 2016. Atomic and Molecular Phases of the Interstellar Medium. *Proceedings IAU Symposium No*. 315.

[14] MacLow, M.M., Smith, M.D., Klessen, R.S. and Burkert, A. (1998) Decay Timescales of MHD Turbulence in Molecular Clouds. *Astrophysics and Space Science*, **261**, 195-196. https://doi.org/10.1023/A:1002036113496

[15] Mac Low, M.M. and Klessen, R.S. (2004) Control of Star Formation by Supersonic Turbulence. *Reviews of Modern Physics*, **76**, 125-194. https://doi.org/10.1103/RevModPhys.76.125

[16] Ballesteros-Paredes, J., Klessen, R.S., Mac Low, M.-M. and Va'zquez-Semadeni, E. (2007) Molecular Cloud Turbulence and Star Formation.

[17] Körtgen, B., Banerjee, R., Pudritz, R.E. and Schmidt, W. (2018) The Origin of Filamentary Star Forming Clouds in Magnetized Galaxies. *Monthly Notices of the Roy-*

al Astronomical Society: *Letters*, **479**, L40-L44.

[18] Blitz, L. (2007) Radial Gas Distributions and Gas Depletion Time Problem.

[19] Ward-Thompson, D. and Whitworth, A.P. (2011) An Introduction to Star Formation. Cambridge University Press, Cambridge, 5.

[20] Beck, R. (2001) Galactic and Extragalactic Magnetic Fields. *Space Science Reviews*, **99**, 243-260. https://doi.org/10.1023/A:1013805401252

[21] Crutcher, R.M., Hakobian, N. and Troland, T.H. (2010) Self-Consistent Analysis of OH Zeeman Observations. *Monthly Notices of the Royal Astronomical Society*: *Letters*, **402**, L64-L66. https://doi.org/10.1111/j.1745-3933.2009.00802.x

[22] Gorti, U., Dullemond, C.P. and Hollenbach, D. (2009) Time Evolution of Viscous Circumstellar Disks Due to Photoevaporation by Far-Ultraviolet, Extreme-Ultraviolet, and X-Ray Radiation from the Central Star. *The Astrophysical Journal*, **705**, 1237-1251. https://doi.org/10.1088/0004-637X/705/2/1237

[23] Yorke, H.W., *et al*. (1995) The Formation of Protostellar Disks. 2: Disks around Intermediate-Mass Stars. *The Astrophysical Journal*, **443**, 199-208. https://doi.org/10.1086/175514

[24] Holt, E.S. and Mundy, L. (1997) Star Formation near and far. AIP Press.

[25] Shu, F.H., Li, Z.-Y. and Allen, A. (2004) Does Magnetic Levitation or Suspension Define the Masses of Forming Stars? *The Astrophysical Journal*, **601**, 930-951. https://doi.org/10.1086/380602

[26] Tahani, M., Plume, R., Brown, J.C. and Kainulainen, J. (2018) A& A, 614A.100T.

[27] Lada, C.J., Lombardi, M. and Alves, J.F. (2009) The California Molecular Cloud. *The Astrophysical Journal*, **703**, 52. https://doi.org/10.1088/0004-637X/703/1/52

International Journal of Astronomy and Astrophysics, 2018, 8, 368-385
http://www.scirp.org/journal/ijaa
ISSN Online: 2161-4725
ISSN Print: 2161-4717

Trajectory Design and Optimization for LEO Satellites in Formation to Observe GEO Satellites' Beams

Yi Lu[1], Yu Sun[1], Xiyun Hou[2], Yunhe Meng[3]

[1]State Key Laboratory of Astronautic Dynamics, China Xi'an Satellite Control Center, Xi'an, China
[2]School of Astronomy & Space Science, Nanjing University, Nanjing, China
[3]Tianqin Research Center for Gravitational Physics, Sun Yat-sen University, Zhuhai, China
Email: luyi_xscc@126.com

How to cite this paper: Lu, Y., Sun, Y., Hou, X.Y. and Meng, Y.H. (2018) Trajectory Design and Optimization for LEO Satellites in Formation to Observe GEO Satellites' Beams. *International Journal of Astronomy and Astrophysics*, **8**, 368-385.
https://doi.org/10.4236/ijaa.2018.84026

Received: September 7, 2018
Accepted: December 15, 2018
Published: December 18, 2018

Abstract

This paper presents the methods and results for the trajectory design and optimization for the low earth orbit (LEO) satellites in formation to observe the geostationary orbit (GEO) satellites' beams. The background of the trajectory design mission is the 9th China Trajectory Optimization Competition (CTOC9). The formation is designed according to the observation demands. The flying sequence is determined by a reference satellite using a proposed improved ephemeris matching method (IEMM). The formation is changed, maintained and transferred following the reference satellite employing a multi-impulse control method (MICM). Then the total observation value is computed by propagating the orbits of the satellites according to the sequence and transfer strategies. Based on the above methods, we have obtained a fourth prize in the CTOC9. The proposed methods are not only fit for this competition, but can also be used to fulfill the trajectory design missions for similar multi-object explorations.

Keywords

Trajectory Design, Global Optimization, Formation Flying, Flying Sequence, Formation Maintaining

1. Introduction

Geostationary orbit (GEO) plays an important role in communication, navigation, and other areas [1] [2]. With an orbital period equal to the Earth's rotation period, the GEO satellites are always above the Earth's equator, and are fixed

relative to an Earth-fixed observer [3]. This principal characteristic of the GEO makes it suitable for communication and navigation satellites [4]. Meanwhile, it is essential of the frequency resources for construction of the communication and navigation satellites' systems [5]. Hence, it is of significance to monitor the usage of the frequency resources of GEO satellites. Based on this background, problem A of CTOC9 has considered the orbit design and optimization mission for the low earth orbit (LEO) satellites in formation to observe the GEO satellites' beams [6]. The J2 perturbation must be considered when propagating the orbits and maintaining the flying formation [7].

The problem is a multi-object optimization problem, which appears in many practical applications. For example, the multi-asteroid exploration, the multi-planet exploration and the multi-debris clearing mission [8] [9]. At the end of the CTOC9, teams from NUAA [10], NUDT [11], and Tsinghua University [12] have obtained the first, second, and third prizes. And we have obtained the fourth. Most of them used the regressive orbit to solve the special problem, but our methods are different from theirs. We attempted to propose more general methods to solve not only this problem but also other multi-objective trajectory design problems.

This paper is organized as follows. Section 2 gives a brief description of the problem. Section 3 gives the general description of the methods. Application of the methods to the problem is presented in Section 4. Results and conclusions are finally presented in Sections 5 and 6.

2. Brief Description of the Problem

In the problem, the GEO constellation consists of 18 satellites, each of which is equipped with a transmitter which directs its beam to the ground station. The diagram of the projection of the GEO satellites' beams is shown in **Figure 1**.

An LEO formation consisting of 3 monitoring satellites is inserted into circular orbits of altitude of 400 km and inclination of 42.8˚ at initial time. The task of the three monitoring satellites is to monitor all the beams of the GEO satellites. The "monitoring" operation of a GEO satellite beam is executed only when the three monitoring satellites are in the coverage of the beam. Monitoring profit of a GEO satellite, which is defined by the geometry between the three monitoring satellites and the GEO satellite, is accumulated in the process of monitoring execution. Assuming the three monitoring satellites are in the coverage of a GEO satellite's beam at a specified time, **Figure 2** shows the geometry of the three monitoring satellites and the GEO satellite. When the monitoring profits of all 18 GEO satellites reach a certain threshold (In the problem, it is 1×10^7 km^2), the whole monitoring task is completed. Please refer to Ref. [6] for more information of the monitoring profits' computational method and the overall description of the problem.

There are two optimization objectives of different priorities in the problem. The primary objective is to minimize the time duration of the whole monitoring

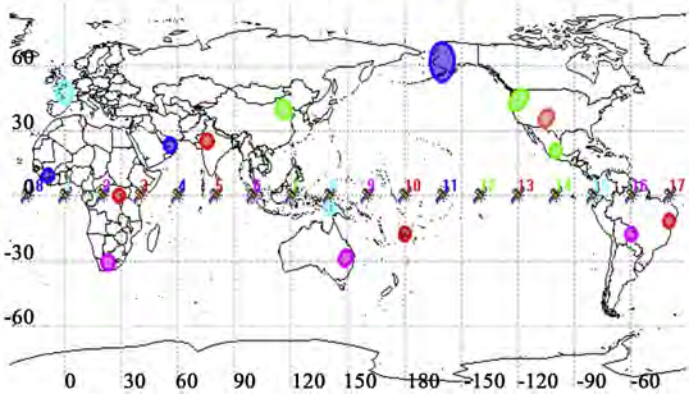

(a)

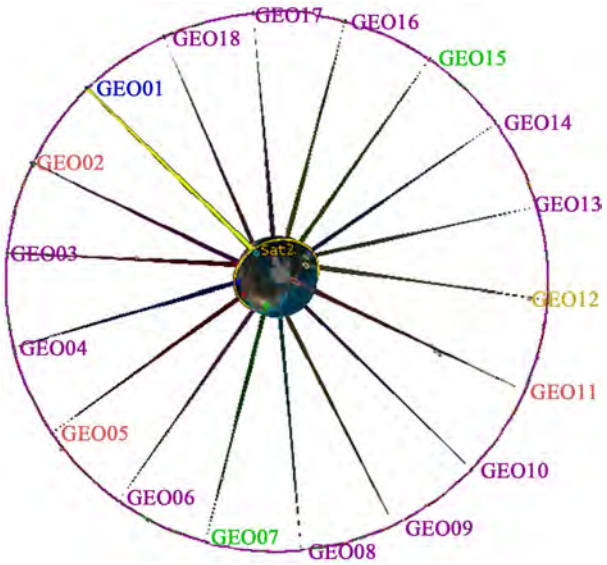

(b)

Figure 1. The diagram of the projection of the GEO satellites' beams [6]. (a) Refers to the two-dimensional view and (b) Refers to the three-dimensional view.

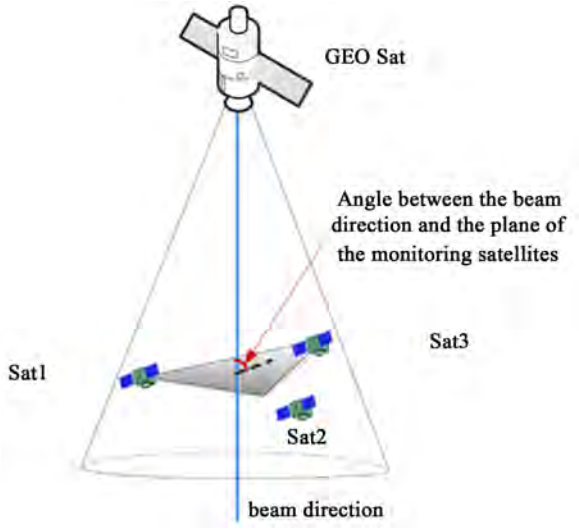

Figure 2. Geometry of the three monitoring satellites and one GEO satellite [6].

task. The secondary objective, in case two or more teams achieve the same primary objective, is to minimize the total fuel consumption of the three monitoring satellites.

Each monitoring satellite is subject to the J_2 perturbation. And the motion equation in the J2000 earth centered inertial coordinate is as follows,

$$\begin{cases} \dot{x} = v_x \\ \dot{y} = v_y \\ \dot{z} = v_z \\ \dot{v}_x = -\dfrac{\mu x}{r^3}\left(1+\dfrac{3}{2}J_2\left(\dfrac{R_e}{r}\right)^2\left(1-5\dfrac{z^2}{r^2}\right)\right) \\ \dot{v}_y = -\dfrac{\mu y}{r^3}\left(1+\dfrac{3}{2}J_2\left(\dfrac{R_e}{r}\right)^2\left(1-5\dfrac{z^2}{r^2}\right)\right) \\ \dot{v}_z = -\dfrac{\mu z}{r^3}\left(1+\dfrac{3}{2}J_2\left(\dfrac{R_e}{r}\right)^2\left(3-5\dfrac{z^2}{r^2}\right)\right) \end{cases} \tag{1}$$

In which, μ is the gravitational constant of the earth. x, y, and z refer to the position of the satellites. v_x, v_y, v_z refer to the velocity. $r = \sqrt{x^2+y^2+z^2}$ refers to the range from the earth center to the satellite. R_e is the radius of the earth, and J_2 is the perturbation constant of the earth's oblateness.

The initial masses of all satellites are 500 kg, and the allowed fuel consumption should not be more than 200 kg. The maneuvers of the monitoring satellites are instantaneous changes of the satellites velocities. After each maneuver, the fuel consumption Δm should be evaluated using the Tsiolkovsky equation.

$$\Delta m = m\left(1-\mathrm{e}^{\frac{-\Delta V}{g_e I_{sp}}}\right) \tag{2}$$

where m is the mass before the maneuver, ΔV is the magnitude of the maneuver, g_e is the acceleration of gravity at sea level of Earth, I_{sp} is the specific impulse of the propulsion.

The GEO satellites are assumed to follow non-perturbed Keplerian orbits. The longitude and radius of each GEO satellite remain constant, and the latitude remains zero during the whole mission. For more information of the problem description, please refer to Ref. [6].

3. General Description of the Method

3.1. Outline of the Method

In order to solve the problem effectively, we decomposed the methods used by us into following steps.

Step 1: The formation is designed according to the observation demands by analyzing the observation features.

Step 2: The flying sequence is firstly determined by a specified reference satellite using a proposed improved ephemeris matching method (IEMM). Then, the

formation is maintained and transferred following the reference satellite by a multi-impulse control method (MICM). The total monitoring profit is computed by propagating the satellites' orbits subject to J_2 perturbation according to the sequence and transfer strategies.

Step 3: The result data is checked and submitted to the competition organizer.

The basic procedure of the methods employed in this paper for solving the problem A of CTOC9 is described in **Figure 3**.

3.2. Formation Designing

In order to design stable formations and reduce the maintaining cost, we analyzed the stability of the formations by propagating the differential equations of the elements difference between the satellites. In the presence of the J_2 perturbation, some orbital elements change, including the drifts in perigee and mean anomaly, and the nodal regression. Employing orbit-averaged quantities [13] [14], differences in the orbital elements between the leader and the follower satellites are given as below:

$$\begin{cases} \delta\dot{a} = \delta\dot{e} = \delta\dot{i} = 0 \\ \delta\dot{\Omega} = -\dfrac{3\sqrt{\mu}J_2R_e^2}{2\left(1-e_L^2\right)^2 a_L^{3.5}}\left[-\sin i_L \delta i + \cos i_L\left(\dfrac{4e_L\delta e}{1-e_L^2} - \dfrac{7\delta a}{2a_L}\right)\right] \\ \delta\dot{\omega} = \dfrac{3\sqrt{\mu}J_2R_e^2}{4\left(1-e_L^2\right)^2 a_L^{3.5}}\left[-5\sin 2i_L\delta i + \left(5\cos^2 i_L - 1\right)\left(\dfrac{4e_L\delta e}{1-e_L^2} - \dfrac{7\delta a}{2a_L}\right)\right] \\ \delta\dot{M} = -\dfrac{3}{2}\sqrt{\dfrac{\mu}{a_L^3}}\dfrac{\delta a}{a_L} + \dfrac{3\sqrt{\mu}J_2R_e^2}{4\left(1-e_L^2\right)^{1.5} a_L^{3.5}} \\ \qquad \times\left[-3\sin 2i_L\delta i + \left(3\cos^2 i_L - 1\right)\left(\dfrac{3e_L\delta e}{1-e_L^2} - \dfrac{7\delta a}{2a_L}\right)\right] \end{cases} \tag{3}$$

where μ is the gravity constant of Earth. a, e, i, Ω, ω, M are the orbital elements of the satellites, and δa, δe, δi, $\delta\Omega$, $\delta\omega$, δM are the elements' differences between

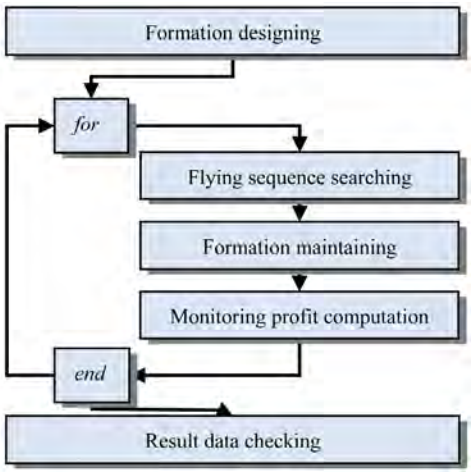

Figure 3. The procedure of the methods employed for solving the problem A of CTOC9.

the leader and the follower satellites. The elements with subscript L refer to the leader satellites.

Equation (3) shows that the J_2 perturbation does not change the differences of a, e, i but changes the differences of Ω, ω, M between the leader and the follower satellites. If the initial values of the elements' differences with subscript "0" at time t_0 are given, the values at any time t can be computed as follows,

$$\begin{cases} \delta a = \delta a_0, \delta e = \delta e_0, \delta i = \delta i_0 \\ \delta\Omega = \delta\Omega_0 + \delta\dot{\Omega}\left(t - t_0\right) \\ \delta\omega = \delta\omega_0 + \delta\dot{\omega}\left(t - t_0\right) \\ \delta M = \delta M_0 + \delta\dot{M}\left(t - t_0\right) \end{cases} \tag{4}$$

Equations (3) and (4) obviously show that, when there are differences in the elements a, e or i, the formation is unstable, and changes quickly. As a result, in this paper, the three satellites' initial elements a, e and i are chosen to be nearly the same.

The initial relations of the three satellites' elements will be determined by the mission's requirements, which will be shown in Section 4.1.

3.3. Flying Sequence Searching

For the flying sequence searching, the improved ephemeris matching method (IEMM) is proposed.

From the characteristics of the Lambert problem [15], it is not hard to understand that, the closer distance from the satellite's position (propagated to the target time without any control from the leaving beam b_l) to the position of the target beam b (propagated to the target time) is, the less energy is needed for the satellite to transfer from b_l to flyby b. Thereby we can measure the relative size of the transfer energy consumed by examining the closeness between the target beam's ephemeris and the satellite' ephemeris propagated from the leaving beam. In this paper, we define the reference satellite as the leader satellite. When propagating the reference satellite's orbit, the satellite's velocity when leaving the beam is not fixed. We add a small Δv along the velocity in range [−25 m/s, 25 m/s] at the departure epoch with a step size of 5m/s and propagate the satellite's trajectory. We pick up the one closest to the matching target beam (if the monitoring profit for this beam is not fulfill the requirement), record the Δv value, the arrival time t_f, and the position $\boldsymbol{R}$ and velocity $\boldsymbol{V}$ of the closest point from the central line of the beam to the reference satellite's propagated orbit. This process is different from the ephemeris matching method (EMM) in Ref. [16], in which the trajectory is propagated without Δv along the velocity, so we call it improved ephemeris matching method (IEMM).

For a segment of the transfer trajectories, the mathematical model of IEMM can be expressed as

$$\Delta v = f\left(\lambda_r \left\|\boldsymbol{R}(t) - \boldsymbol{R}_b(t)\right\|, \lambda_v \left\|\boldsymbol{V}(t) - \boldsymbol{V}_b(t)\right\|\right) \tag{5}$$

where $f(\cdot)$ is a monotonic increasing function; $\boldsymbol{R}$ and $\boldsymbol{V}$ are respectively the position and velocity of the satellite's propagated orbit at arrival time t; $\boldsymbol{R}_b$ and $\boldsymbol{V}_b$ are

respectively the position and velocity of a point on the central line of a beam b. The point is chosen to be with the same height to the satellite's propagated orbit at the arrival time. λ_r and λ_v are the weights of the positions' difference and velocities' difference. For this paper, the satellites need to flyby (not rendezvous) the target beam, so the velocities between them need not to be equal. Only the positions need to match. Therefore, λ_v is set to be 0, and λ_r could be 1.

For a transfer segment, when we have set a Δv_i (which is determined by step 5m/s in the small range [−25, 25] m/s from lowest to highest), the target beam b_i whose ephemeris matches the reference satellite could be found along the propagating satellite's orbit till t_f. Then we identify the target beam and record the corresponding parameters that meet the condition of top 5 values of the net accumulated monitoring profits when propagating the satellites orbits in the segment. Here net profit means when the accumulated monitoring profit of a GEO satellite's beam has up to the threshold, it will not be added to the total accumulated value computed along this segment. When computing the monitoring profit, the formation is formed theoretically by the geometry relationship between the leader and the follower satellites, because in this sequence searching process, the formation maintaining is not considered.

The procedure of the IEMM algorithm is shown in Figure 4, and is described as follows:

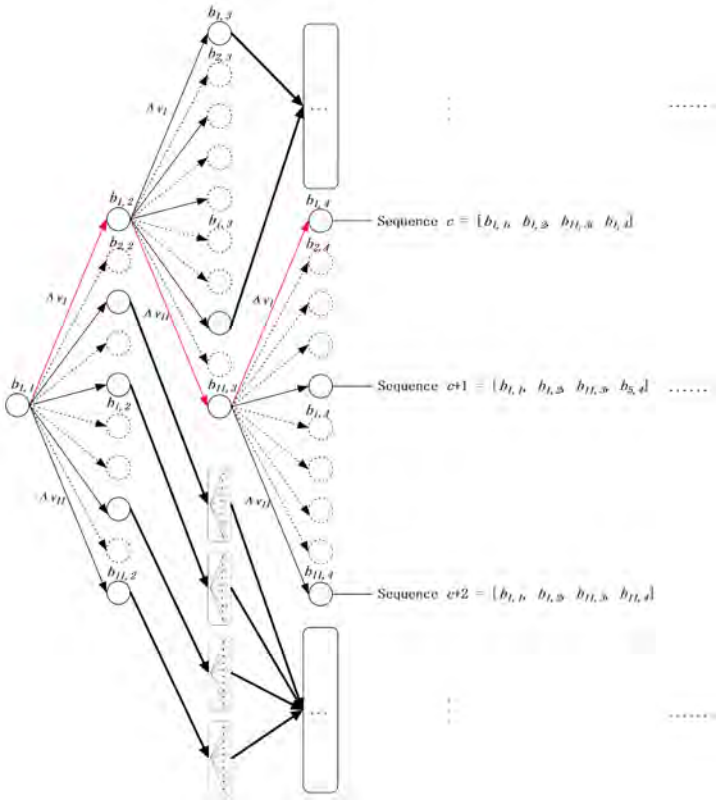

Figure 4. The procedure of the IEMM algorithm. The solid arrows and circles refer to the recorded sequences, and the dotted arrows and circles refer to the abandoned sequences. The red arrows are connected to show an example sequence c.

Step 1: Propagate the reference satellite's orbits from the last beams of the recorded sequences with the initial velocity offset Δv_i from −25 m/s to 25 m/s with a step size of 5 m/s. There will be 11 orbits to be propagated.

Step 2: Find the 11 target beams whose central line is closest to the satellite's orbits corresponding to Δv_i at the end time t_f.

Step 3: Propagate the reference satellite's orbit and use the theoretical formation (by the geometry relationship between the leader and follower satellites) to compute the net accumulated monitoring profits.

Step 4: For a sequence, if the total monitoring profit meets the condition of all the beams' monitoring profits up to the threshold, record the new sequence as one of the candidate sequences. If any one of the satellite's fuel has all been consumed but not all the observation values of the beams have been up to the threshold, the sequence is abandoned. Otherwise, abandon the 6 sequences with the least monitoring profits, record the top 5 sequences for further searching, and turn to Step 1.

Step 5: If all recorded sequences have fulfilled the threshold, stop searching, and pick out the sequence with shortest mission time for further processing.

3.4. Formation Maintaining

For the formation maintaining and orbit transfer, a multi-impulse control method (MICM) is employed. The Δvs of all maneuvers are optimized by the differential evolution (DE) algorithm and the J_2 perturbed Lambert problem solving algorithm. The algorithm procedure is shown in Figure 5.

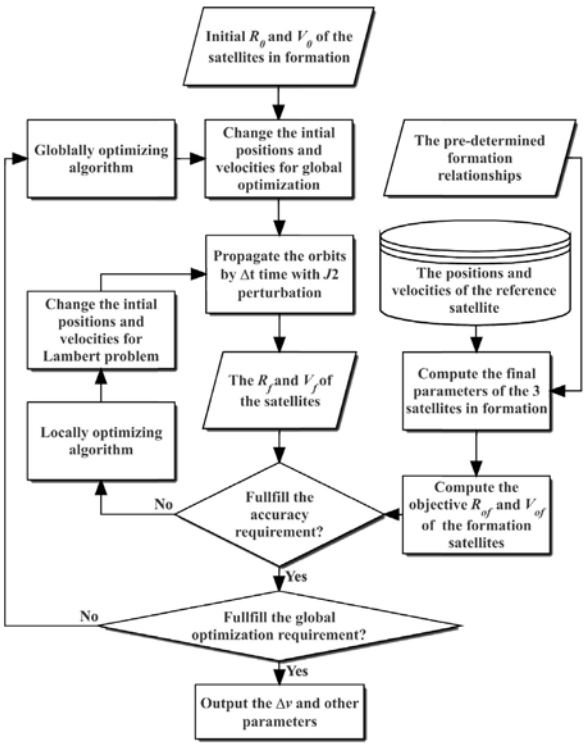

Figure 5. The procedure of the MICM algorithm.

There are two layers of the loop. The inner layer is the solving of the J_2 perturbed Lambert problem. The locally optimization shooting method is used to solve the boundary value problem. If the three satellites' final positions $\boldsymbol{R}_f$ and velocities $\boldsymbol{V}_f$ equal the values predetermined by the theoretical relationship of the formation, the problem is solved. The predetermined values are given by the sequence searching and formation designing algorithms. When the position and velocity of the reference satellite are provided, based on the relationship between the three satellites in formation, the required positions and velocities of the follower satellites are determined, which are the objective values of the shooting method.

The outer layer of the loop is using the DE algorithm to optimize the velocity increments (Δvs) to be minimal. The optimizing problem is a time-fixed optimal transfer problem. DE is a heuristic searching algorithm introduced by Storn and Price [17]. Its remarkable performance as a global optimization algorithm on continuous numerical minimization problems has been extensively explored [18]. As with other evolutionary algorithms, DE solves optimization problems by evolving a population of candidate solutions using alteration and selection operators. For the problem in this paper, the objective function is as follows:

$$J = \min\left\{\Delta v_{i,k}\right\} \tag{7}$$

where $\Delta v_{i,k}$ refers to the sum of the velocity increments of the i^{th} transfer of satellite k. The variables to be determined by the optimization are as follows,

$$\begin{cases} \boldsymbol{\Phi}_{1,k} = \left[\Delta t_{1,k}, \Omega_{1,k}, \omega_{1,k}, M_{1,k}, \Delta t'_{1,k}, \Delta R_{1,x}, \Delta R_{1,y}, \Delta R_{1,z}\right] \\ \boldsymbol{\Phi}_{c,k} = \left[\Delta t_{c,k}, \Delta t'_{c,k}, \Delta R_{c,x}, \Delta R_{c,y}, \Delta R_{c,z}\right] \\ \boldsymbol{\Phi}_{i,k} = \left[\Delta t_{i,k}, \Delta\omega_{i,k}\right], i \neq 1 \neq c \end{cases} \tag{8}$$

in which $\boldsymbol{\Phi}_{1,k}$ indicates the variables relative to the three-impulse transfer for the first maneuver of satellite k; $\Delta t_{1,k}$ is the waiting time when the satellite is flying along the initial orbit; $\Omega_{1,k}$, $\omega_{1,k}$, and $M_{1,k}$ are respectively the right ascension node, the argument of perigee, and the mean anomaly of the initial orbit; $\Delta t'_{1,k}$ is the transfer time from the leaving point to a middle point on an initial J_2 perturbed Lambert orbit; $\Delta R_{1,x}$, $\Delta R_{1,y}$, and $\Delta R_{1,z}$ are the position offsets from the middle points. Then two Lambert orbits are computed again to fulfill the transfers from the leaving point to the middle point and from the middle point to the end point.

$\boldsymbol{\Phi}_{c,k}$ indicates the variables relative to the three-impulse transfer for formation changing (Why the formation need to be changed? Please refer to section 4.1.) of satellite k; $\Delta t_{c,k}$ is the waiting time, at the end of which the satellite start to transfer; $\Delta t'_{c,k}$ is the transfer time from the leaving point to a middle point on an initial J_2 perturbed Lambert orbit; $\Delta R_{c,x}$, $\Delta R_{c,y}$, and $\Delta R_{c,z}$ are the position offsets from the middle points. Then two Lambert orbits are computed again to fulfill the transfers from the leaving point to the middle point and from the middle point to the end point.

$\Phi_{i,k}$ indicates the variables relative to the two-impulse transfers for the rest maneuvers of satellite k; $\Delta\omega_{i,k}$ is the difference of the argument of perigee between the leader satellite and the follower satellite. When propagating the orbits, only small difference of $\Delta\omega_{i,k}$ will be generated by the J_2 perturbation. In order to save fuel, we do not require the argument of perigee for the 3 satellites exactly equal each other. But when solving the J_2 perturbed Lambert problem, the offset of the target mean anomaly should be set to have an opposite value to $\Delta\omega_{i,k}$. This will ensure a relatively stable shape to fulfill the observation. The bounds of the variables are shown in Table 1.

3.5. Monitoring Profit Computation

Incorporating all the maneuvers of the 3 monitoring satellites, the observation values W_j are computed by propagating the J_2 perturbed orbits with a step time t_m of 1 second using Equation (9) [6]:

$$W_j = \sum_{m=1}^{M} S_j(t_m)\, g_j(t_m) \tag{9}$$

where j refers to the label of the GEO satellite's beam, S_j is the area of the triangle formed by 3 monitoring satellites, and g_k is sine of the angle from the GEO satellite's beam to the triangle plane. The results are organized to fit the submission format in order to pass the data checking process. M refers to the total duration (in second) when the triangle is in the beam j.

4. Application of the Method to the Problem

4.1. Formation Determination

In order to monitor the 11th GEO satellite whose beam is locating at the highest latitude (which is shown in Figure 6), we raise the apogees of the three orbits and make the formation be a triangle parallel with the orbit plane to reach the beam. Of course if we raise the inclinations of the orbits, the 11th beam could also be monitored, but it will consume too much fuel. So we choose the first way.

Table 1. Bounds of the variables.

	$\Delta t_{1,k}$/s	$\Omega_{1,k}$/deg	$\omega_{1,k}$/deg	$M_{1,k}$/deg	$\Delta t'_{1,k}$/s	$\Delta R_{1,x}$/km	$\Delta R_{1,y}$/km	$\Delta R_{1,z}$/km
up	$\Delta T_1/2$	10	90	90	90	30	30	30
low	0	−10	−90	−90	−90	−30	−30	−30
	$\Delta t_{c,k}$/s	$\Delta\omega_{c,k}$/deg	$\Delta t'_{c,k}$/s	$\Delta R_{c,x}$/km	$\Delta R_{c,y}$/km	$\Delta R_{c,z}$/km		
up	180	4	$\Delta T_c + 500$	50	50	50		
low	−60	−4	$\Delta T_c - 500$	−50	−50	−50		
	$\Delta t_{i,k}$/s	$\Delta\omega_{i,k}$/deg						
up	45	2						
low	−45	−2						

Note: ΔT_1 is the time range from initial to the first beam in the sequence. ΔT_c is the time range from the leaving to the arriving point of the formation changing transfer.

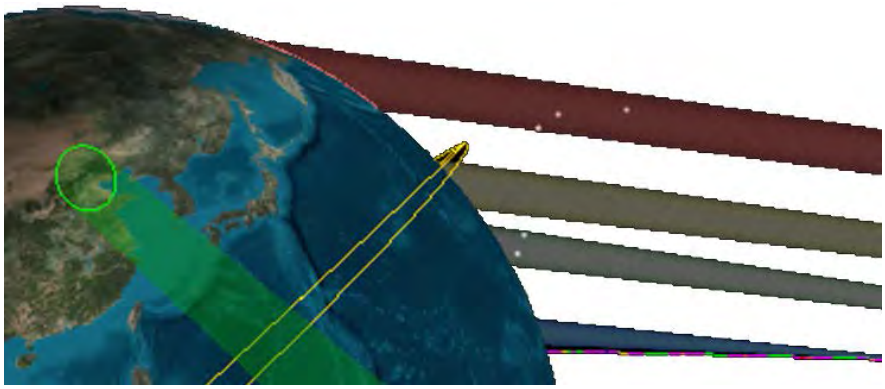

Figure 6. The three-diminsional geometry of the 11th beam, which is the highest one in the figure. The yellow thin lines are the satellites's initial orbits.

When the monitoring profit of the 11th GEO satellite's beam is near 1×10^7 km^2, the formation is changed from the first one to the second one which constitutes a triangle perpendicular to the orbit plane for the observing of the remaining GEO satellites' beams locating at the low latitudes. The first and the second formations are shown in Figure 7.

When designing the formations, not only the monitoring requirements, but also the stability should be considered to reduce the formation maintaining cost. Finally, the relations of the 3 satellites are determined and shown in Table 2.

The leader satellites' elements a_L, e_L, i_L, Ω_L, ω_L, M_L are determined by the flying sequence and transferring strategies. The follower satellites are transferred to fit the relations in Table 2. The values of differences between the elements of the leader and the followers are determined by optimization to find the highest mean monitoring profit for passes of the GEO satellite's beams.

4.2. Flying Sequence Determination

For the flying sequence determination, the proposed IEMM described in Section 3.3 is employed. For every searched sequence, the labels of the beams, the epochs when the leader satellite arrive the beams and the positions & velocities of the orbits are recorded. Then the top 5 beams with high monitoring profits are chosen and added to the sequence to form new sequences. For a special sequence, if the total monitoring profit meets the condition of all the beams' monitoring profits up to the threshold, record the new sequence as one of the candidate sequences. If any one of the satellite's fuel has all been consumed but not all the monitoring profits of the beams have been up to the thresholds, the sequence is abandoned. Otherwise, abandon the last 6 values, and record the top 5 sequences for further searching. If all recorded sequences have fulfilled the threshold condition, stop searching, and pick out the sequence with shortest mission time for further processing.

The sequence searching result is shown in Figure 8, which shows that most of the durations between two target beams of the ephemeris matching processes are no longer than 1×10^5 s (27.8 hours). Most of the distances between the

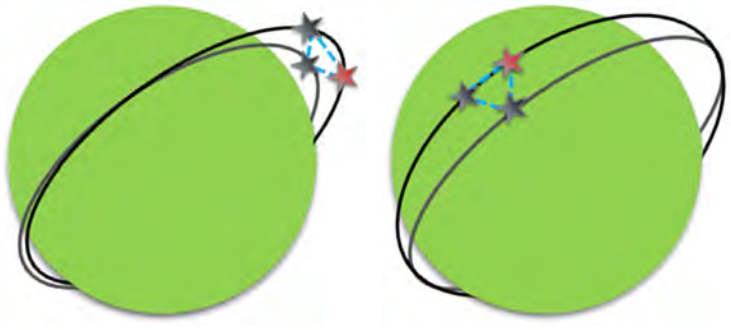

(a) (b)

Figure 7. The designed formations. The red star refers to the reference satellite which is also the leader satellite, and the other two are the follower satellites. (a) The first formation constitutes a triangle parallel to the orbit plane. (b) The second formation constitutes a triangle perpendicular to the orbit plane.

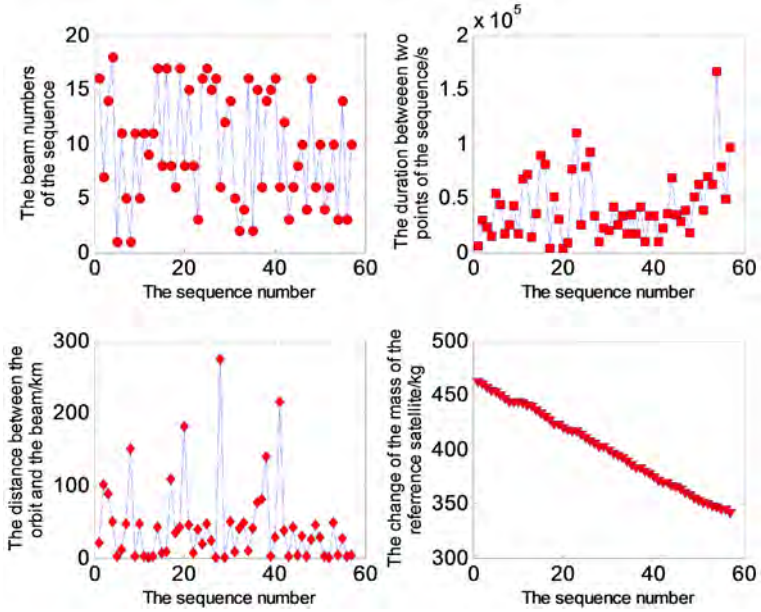

Figure 8. The sequence searching result. The first sub-figure refers to the beam numbers of the best sequence. The second sub-figure refers to the duration between two points of the sequence. The third sub-figure refers to the distance between the reference satellite's orbit and the central line of the corresponding target beam. And the fourth sub-figure refers to the change of the reference satellite's mass.

Table 2. The relations of the 3 satellites.

Formation	Satellite	a	e	i	Ω	ω	M
Formation 1	Leader	a_L	e_L	i_L	Ω_L	ω_L	M_L
	Follower 1	a_L	e_L	i_L	Ω_L	ω_L	$M_L - 2.237$
	Follower 2	a_L	$e_L - 0.02$	i_L	$\Omega_L + 3$	ω_L	M_L
Formation 2	Leader	a_L	e_L	i_L	Ω_L	ω_L	M_L
	Follower 1	a_L	e_L	i_L	Ω_L	ω_L	$M_L + 2.237$
	Follower 2	a_L	e_L	i_L	$\Omega_L + 3$	ω_L	$M_L - 1$

reference satellite's orbits and the central line of the corresponding target beams are no more than 100 km, which means that most of the target beams in addition to the passed beams along the transfer orbit could all be observed by the formation. The consumed fuel by the reference satellite is lower than 160 kg, which means 40 kg left could be used to guarantee the fulfillment of the formation transfer and maintenance along the overall task.

4.3. Formation Transfer and Maintenance

For the formation transfer and maintenance, the MICM described in section 3.4 is employed. The time points, Δvs of all maneuvers are optimized by the DE algorithm and J_2 perturbed Lambert problem solving algorithm. Therefore, the satellites can fly following the reference satellite and the formation can be maintained. The orbit of the reference satellite is shown in Figure 9, in which the red pluses refer to the maneuvers.

The changes of the reference satellite's elements are shown in Figure 10, in which the semi-major and the orbital eccentricity are firstly raised by the initial transfer, and then oscillate in the following transfers. The orbital inclination nearly unchanged to save fuel. And the right ascension node changes from about 225 deg to 100 deg due to the J_2 perturbation.

The consumed fuel for all the maneuvers are shown in Figure 11. For every transfer, the velocity increment and the consumed fuel are minimized by the DE algorithm. There are 3 transfers whose consumed fuels are much more than others. The first one is for the transfer from the initial circular orbit to the elliptical orbit, the second one is for the formation changing, and the third one is for the final flying by to monitor the last beam in order to make the total time to be the least while consuming nearly all the fuel of each satellite.

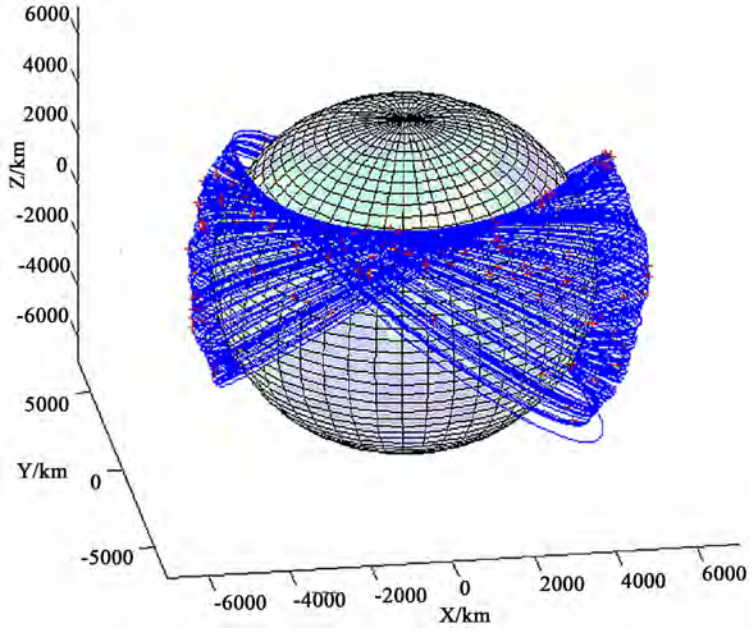

Figure 9. The orbit of the reference satellite (The red pluses refer to the maneuvers).

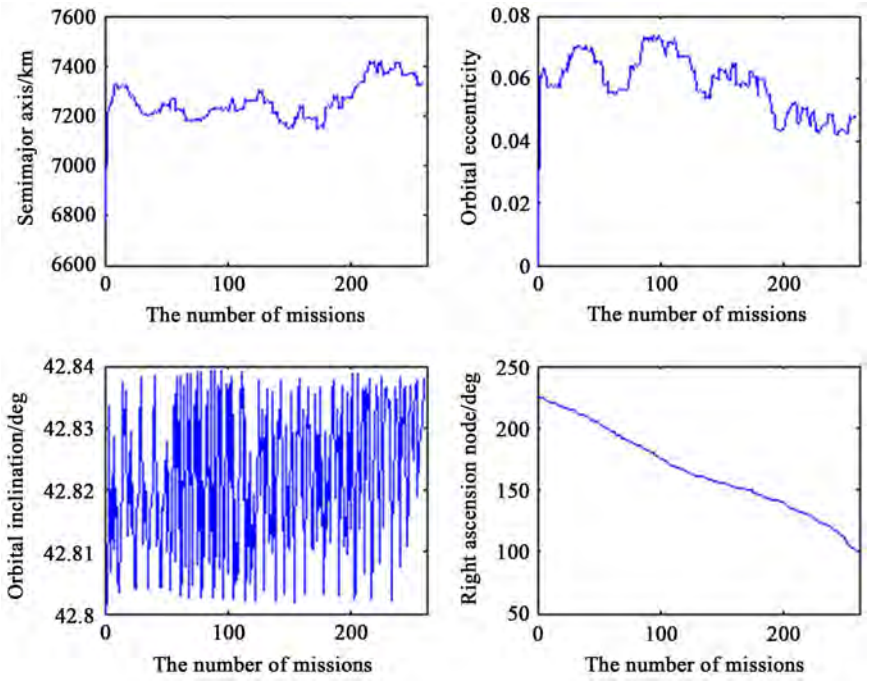

Figure 10. The changing of the reference satellite's elements.

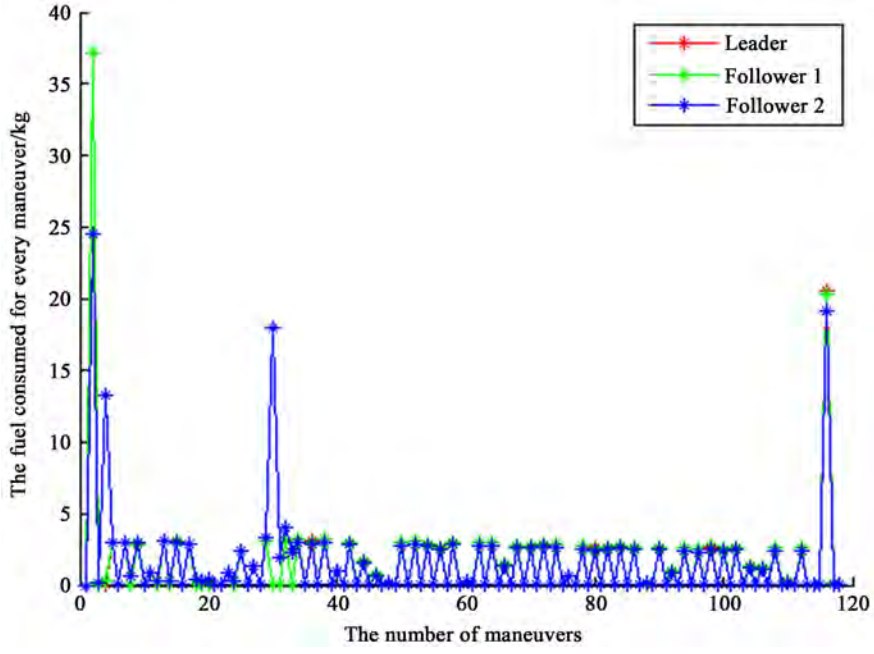

Figure 11. The consumed fuels for the satellites' maneuvers.

4.4. Monitoring Profit Computation

Incorporating all the maneuvers of the 3 satellites, the monitoring profits (observation values) shown in Figure 12 are computed using Equation (9) by propagating the orbits. Figure 12 also shows that all the monitoring profits of the GEO satellites' beams are larger than the threshold of 1×10^7 km, which fulfills the requirement of the overall monitoring task.

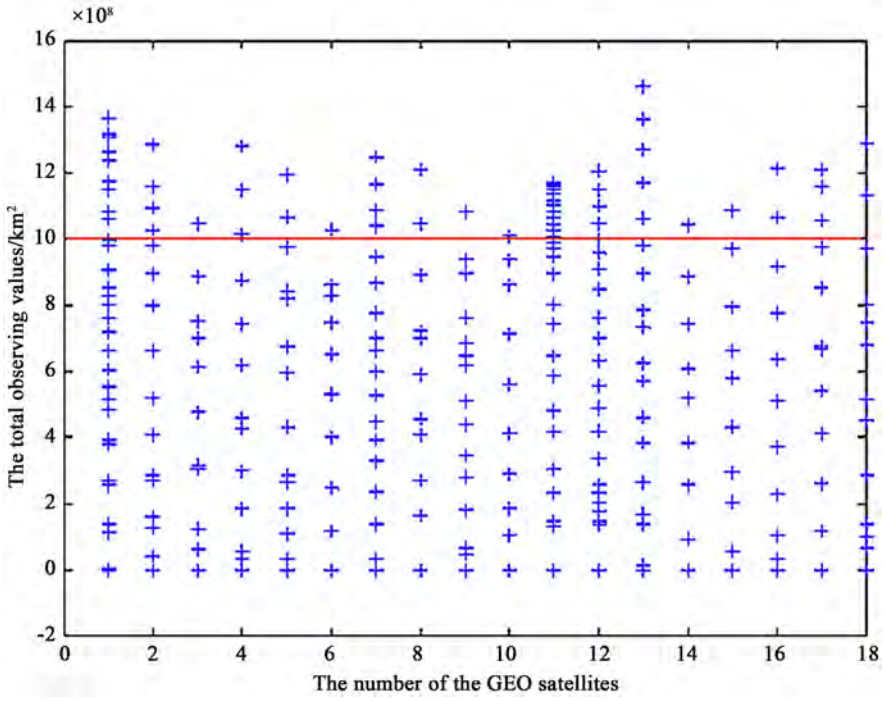

Figure 12. The monitoring profits of all the GEO satellite's beams (The red line refers to the value of 1×10^7 km^2). The distance between every two pluses for every beam refers to the incremented monitoring profit for every monitoring mission.

5. Competition Results

We have obtained the fourth prize of CTOC9. The total flying time is 26.9611 days, and the total consumed fuel is 549.3799 kg, as shown in Table 3. The reasons for the discrepancies of the results obtained in this paper and that obtained by the previous research teams at NUAA, NUDT and Tsinghua University may be the amount of calculation is much larger than them, thus missed the optimal solution in a limited duration of the competition.

The initial parameters, the number of maneuvers, and the final consumed fuels of the 3 satellites are shown in Table 4.

The final observation values are shown in Table 5.

6. Conclusion

This paper presented the methods and results for the problem A of CTOC9, the trajectory design and optimization problem for the low earth orbit (LEO) satellites in formation to observe the geostationary orbit (GEO) satellites' beams. Two methods have been proposed to respectively solve the sequence searching and formation transfer & maintenance problems. The first method is the IEMM and the second one is MICM. Compared with other groups with better results, the methods in this paper may be more powerful in solving similar or more complex multi-objective trajectory design problems, because most of the methods used by other groups employed the regressive orbit to solve the special problem A of CTOC9. If the beams pointing to the surface of the earth to be

Table 3. The results of the objective values. (To make a clear comparison, we also presented the results of the other teams in the table.The contents in bold is our result.)

Rank	Team Name	1st Object/day	2nd Object/kg
1	Nanjing University of Aeronautics and Astronautics (NUAA)	20.42817	528.15235
2	Research Center of Flight Dynamics and Control (RCFDC), NUDT	21.40815	450.64002
3	Tsinghua University (TU)	24.97238	588.02681
4	**Xi'an Satellite Control Center (XSCC)**	**26.96105**	**549.37992**
5	Northwestern Polytechnical University (NPU)	27.22356	566.65516
6	Laboratory of Space System Dynamics and Simulation Technology (LSSDST), NUDT	29.06861	545.47487
7	China Academy of Launch Vehicle Technology(CALVT)	41.53081	423.36019
8	China Academy of Space Technology (CAST)	48.96269	526.07781

Table 4. Initial parameters and the final consumed fuels.

	Leader	Follower 1	Follower 2
a (km)	6778.0676	6778.1642	6778.1172
e	1.1058×10^{-5}	4.0258×10^{-6}	5.5090×10^{-6}
i (deg)	42.8000	42.8000	42.8000
Ω (deg)	224.6348	224.5748	227.6658
ω (deg)	67.5210	274.2653	18.3462
M (deg)	202.4822	358.0967	237.9293
Number of maneuvers	116	116	116
Consumed fuel	175.8506	177.3275	196.2017

Table 5. The final monitoring profits.

GEO beam	Monitoring profit/1×10^7 km^2	GEO beam	Monitoring profit/1×10^7 km^2
1	1.3684	10	1.0117
2	1.2856	11	1.1730
3	1.0462	12	1.2073
4	1.2803	13	1.4633
5	1.1974	14	1.0422
6	1.0284	15	1.0859
7	1.2502	16	1.2151
8	1.2091	17	1.2087
9	1.0815	18	1.2898

monitored are not fixed, the regressive orbit may not be an effective candidate tool to solve the problem. But we have attempted to propose general methods

which need not any special characteristics of the monitor or the target. The proposed methods may have a wider application area to solve more multi-objective trajectory design and optimization problems.

Acknowledgements

We are very grateful to the 9th China trajectory optimization competition organizers for the interesting problem, challenge, and fruitful discussions. This work was supported by the Youth Fund Project of the Space Systems Department (No. 2017SY26B0001), the Funds of Natural Science of China (No. 61673390, and No. 61503414), and the Fund of The State Key Laboratory of Astronautic Dynamics (No. 2016ADL-DW0202).

Conflicts of Interest

The authors declare no conflicts of interest regarding the publication of this paper.

References

[1] Shi, R., Liu, L., Long, T., *et al*. (2017) Surrogate Assisted Multidisciplinary Design Optimization for an All-Electric GEO Satellite. *Acta Astronautica*, **138**, 301-317.

[2] Asgarimehr, M. and Hossainali, M.M. (2014) Optimization of Geosynchronous Satellite Constellation for Independent Regional Navigation and Positioning in Middle East Region. *Acta Astronautica*, **104**, 147-158. https://doi.org/10.1016/j.actaastro.2014.07.025

[3] Pocha, J.J. (1987) An Introduction to Mission Design for Geostationary Satellites. Vol. 6, D. Reidel Publishing Company, Dordrecht, 1-8. https://doi.org/10.1007/978-94-009-3857-1

[4] Clarke, A.C. (1945) Extra-Terrestrial Relays—Can Rocket Stations Give World-Wide Radio Coverage? *Wireless World*, 305-308.

[5] Li, H.N. (2014) Geostationary Satellites Collocation. Springer, Berlin Heidelberg. https://doi.org/10.1007/978-3-642-40799-4

[6] Zhao, S.G., Qi, R., Zhang, J.R., *et al*. (2018) Problem A of 9th Trajectory Optimization Competition: Problem Description and Summary of the Results. *Acta Astronautica*.

[7] Alfriend, K.T. and Schaub, H. (2000) Dynamics and Control of Spacecraft Formations: Challenges and Some Solutions. *Journal of the Astronautical Sciences*, **48**, 249-267.

[8] Zhu, K., Jiang, F., Li, J., *et al*. (2009) Trajectory Optimization of Multi-Asteroids Exploration with Low Thrust. *Transactions of the Japan Society for Aeronautical and Space Sciences*, **175**, 47-54. https://doi.org/10.2322/tjsass.52.47

[9] Bérend, N. and Olive, X. (2016) Bi-Objective Optimization of a Multiple-Target Active Debris Removal Mission. *Acta Astronautica*, **122**, 324-335. https://doi.org/10.1016/j.actaastro.2016.02.005

[10] Yang, B., Huang, X.X., Yang, H.W., *et al*. (2018) Problem A of 9th China Trajectory Optimization Competition: Results Found at NUAA. *Acta Astronautica*.

[11] Wu, D., Song, Y., Chi, Z.M., *et al*. (2018) Problem A of the 9th China Trajectory Optimization Competition: Results Found at Tsinghua University. *Acta Astronau-*

tica.

[12] Liang, J., Yang, Z., Zhang, J., *et al*. (2018) Formation Establishment for GEO Satellite Beams Monitoring Using Controlled Regressive Orbits.

[13] Sabol, C., Burn, R. and McLaughlin, C.A. (2001) Satellite Formation Flying Design and Evolution. *Journal of Satellite and Rockets*, **38**, 270-278. https://doi.org/10.2514/2.3681

[14] Li, J.F., Meng, X., Gao, Y.F., *et al*. (2005) Study on Relative Orbital Configuration in Satellite Formation Flying. *Acta Mechanica Sinica*, **21**, 87-94. https://doi.org/10.1007/s10409-004-0009-3

[15] Curtis, H.D. (2005) Orbital Mechanics for Engineering Students. Elsevier, 163-172.

[16] Lu, Y., Li, J., Li, H.N., *et al*. (2014) Fast Design of Low-Thrust Transfer Orbit for Manned Asteroids Exploration. 65*th International Astronautical Congress*, Toronto, 2-6 October 2014.

[17] Storn, R. and Price, K. (1997) Differential Evolution—A Simple and Efficient Heuristic for Global Optimization over Continuous Spaces. *Journal of Global Optimization*, **11**, 341-359. https://doi.org/10.1023/A:1008202821328

[18] Price, K.V., Storn, R.M. and Lampinen, J.A. (2006) Differential Evolution: A Practical Approach to Global Optimization. 2nd Edition, Springer-Verlag, Berlin, 37-134.

International Journal of Astronomy and Astrophysics, 2018, 8, 386-405
http://www.scirp.org/journal/ijaa
ISSN Online: 2161-4725
ISSN Print: 2161-4717

Measurements of the Cosmological Parameters Ω_m and H_0

B. Hoeneisen

Universidad San Francisco de Quito, Quito, Ecuador
Email: bhoeneisen@usfq.edu.ec

How to cite this paper: Hoeneisen, B. (2018) Measurements of the Cosmological Parameters Ω_m and H_0. *International Journal of Astronomy and Astrophysics*, **8**, 386-405.
https://doi.org/10.4236/ijaa.2018.84027

Received: November 21, 2018
Accepted: December 26, 2018
Published: December 29, 2018

Abstract

From Baryon Acoustic Oscillation measurements with Sloan Digital Sky Survey SDSS DR14 galaxies, and the acoustic horizon angle θ_* measured by the Planck Collaboration, we obtain $\Omega_m = 0.2724 \pm 0.0047$, and $h + 0.020 \cdot \sum m_\nu = 0.7038 \pm 0.0060$, assuming flat space and a cosmological constant. We combine this result with the 2018 Planck "TT, TE, EE + lowE + lensing" analysis, and update a study of $\sum m_\nu$ with new direct measurements of σ_8, and obtain $\sum m_\nu = 0.27 \pm 0.08$ eV assuming three nearly degenerate neutrino eigenstates. Measurements are consistent with $\Omega_k = 0$, and $\Omega_{\text{de}}(a) = \Omega_\Lambda$ constant.

Keywords

Cosmological Parameters, Baryon Acoustic Oscillations, Galaxy Distributions, Cosmic Microwave Background

1. Introduction and Summary

From a study of Baryon Acoustic Oscillations (BAO) with Sloan Digital Sky Survey (SDSS) data release DR13 galaxies and the "sound horizon" angle θ_{MC} measured by the Planck Collaboration we obtained $\Omega_m = 0.281 \pm 0.003$ assuming flat space and a cosmological constant [1]. At the time, the 2016 Review of Particle Physics quoted $\Omega_m = 0.308 \pm 0.012$ [2]. The new 2018 Planck "TT, TE, EE + lowE + lensing" measurement [3] obtains $\Omega_m = 0.3153 \pm 0.0073$, while the "TT, TE, EE + lowE + lensing+BAO" measurement obtains $\Omega_m = 0.3111 \pm 0.0056$ [3]. Due to the growing tension between these measurements, we decided to repeat the BAO analysis in Reference [1], this time with SDSS DR14 galaxies.

The main difficulty with the BAO measurements is to distinguish the BAO signal from the cosmological and statistical fluctuations. The aim of the present analysis is to be very conservative by choosing large bins in redshift z to obtain a larger significance of the BAO signal than in [1]. As a result, the present analysis is based on 6 independent BAO measurements, compared to 18 in [1].

We assume flat space, *i.e.* $\Omega_k = 0$, and constant dark energy density, *i.e.* $\Omega_{\text{de}}(a) = \Omega_\Lambda$, except in **Tables 6-8** that include more general cases. We assume three neutrino flavors with eigenstates with nearly the same mass, so $\sum m_\nu \approx 3m_\nu$. We adopt the notation of the Particle Data Group 2018 [4]. All uncertainties have 68% confidence.

The analysis presented in this article obtains $\Omega_m = 0.2724 \pm 0.0047$ so the tension has increased further. We present full details of all fits to the galaxy-galaxy distance histograms of the present measurement so that the reader may cross-check each step of the analysis. Calibrating the BAO standard ruler we obtain $h + 0.020 \cdot \sum m_\nu = 0.7038 \pm 0.0060$, where $H_0 \equiv 100h \text{ km} \cdot \text{s}^{-1} \cdot \text{Mpc}^{-1}$.

Combining the direct measurement $\Omega_m = 0.2724 \pm 0.0047$ with the 2018 Planck "TT, TE, EE + lowE + lensing" analysis obtains $\Omega_m = 0.2853 \pm 0.0040$ and $h = 0.6990 \pm 0.0030$, at the cost of an increase of the Planck χ^2_{P} from 12956.78 to 12968.64.

Finally, we update the measurement of $\sum m_\nu$ of Reference [5] with the data of this Planck + Ω_m combination, and two new direct measurements of σ_8, and obtain $\sum m_\nu = 0.27 \pm 0.08$ eV. This result is sensitive to the accuracy of the direct measurements of σ_8.

2. Measurement of Ω_m with BAO as an *Uncalibrated* Standard Ruler

We measure the comoving galaxy-galaxy correlation distance d_{drag}, in units of c/H_0, with galaxies in the Sloan Digital Sky Survey SDSS DR14 publicly released catalog [6] [7], with the method described in Reference [1]. Briefly, from the angle α between two galaxies as seen by the observer, and their red-shifts z_1 and z_2, we calculate their distance d, in units of c/H_0, assuming a reference cosmology [1]. At this "uncalibrated" stage in the analysis, the unit of distance c/H_0 is neither known nor needed. The adimensional distance d has a component d_α transverse to the line of sight, and a component d_z along the line of sight, given by Equation (3) of [1]. We fill three histograms of d according to the orientation of the galaxy pairs with respect to the line of sight, *i.e.* $d_z/d_\alpha < 1/3$, $d_\alpha/d_z < 1/3$, and remaining pairs. Fitting these histograms we obtain excesses centered at $\hat{d}_\alpha$, $\hat{d}_z$, and $\hat{d}_/$ respectively. Examples are shown in **Figure 1** and **Figure 2**. From each BAO observable $\hat{d}_\alpha$, $\hat{d}_/$, or $\hat{d}_z$ we recover d_{drag} for any given cosmology with Equations (5), (6), or (7) of Reference [1]. Requiring that d_{drag} be independent of red shift z and orientation we obtain the space curvature Ω_k, the dark energy density $\Omega_{\text{de}}(a)$ as a function of the expansion parameter $a = 1/(1+z)$, and the matter density $\Omega_m = 1 - \Omega_{\text{de}}(1) - \Omega_k - \Omega_r$. Full details can be found in [1].

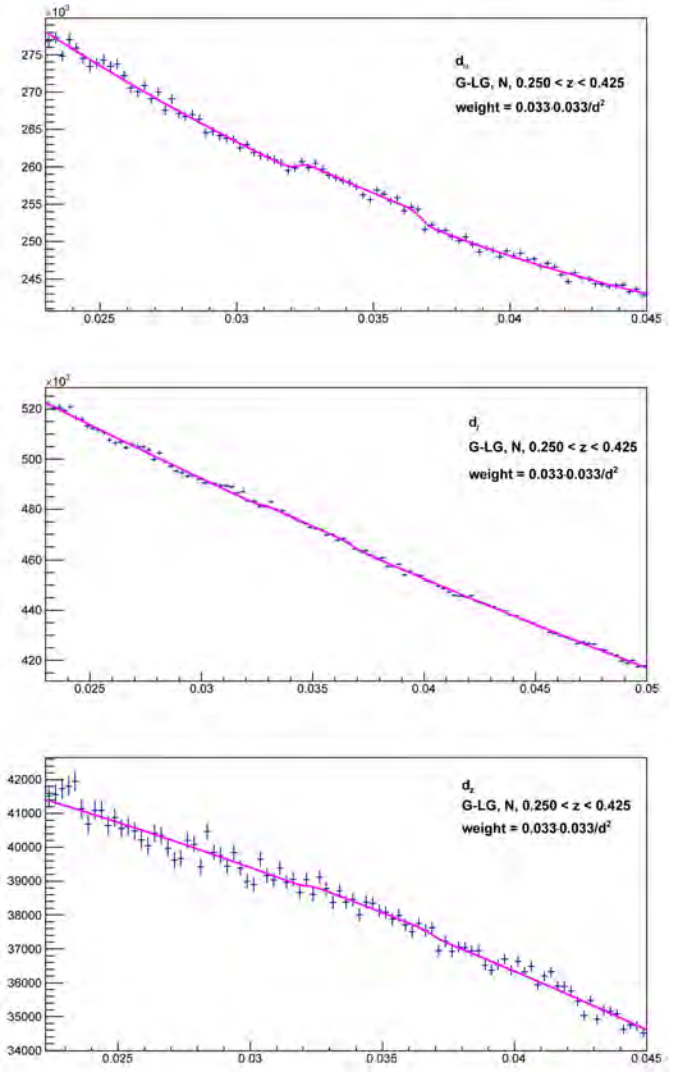

Figure 1. Fits to histograms of G-LG distances d that obtain $\hat{d}_\alpha$, $\hat{d}_/$, or $\hat{d}_z$ at $z = 0.34$. See **Table 1** and **Table 2** for details.

The challenge with these BAO measurements is to distinguish the BAO signal from the cosmological and statistical fluctuations of the background. Our strategy is three-fold: 1) redundancy of measurements with different cosmological fluctuations, 2) pattern recognition of the BAO signal, and 3) requiring all three fits for $\hat{d}_\alpha$, $\hat{d}_/$, and $\hat{d}_z$ to converge, and that the consistency relation $Q = \hat{d}_/ \Big/ \left(\hat{d}_\alpha^{0.57} \hat{d}_z^{0.43}\right) = 1$ [1] be satisfied within $\pm 3\%$.

Regarding redundancy, we repeat the fits for the northern (N) and southern (S) galactic caps; we repeat the measurements for galaxy-galaxy (G-G) distances, galaxy-large galaxy (G-LG) distances, LG-LG distances, and galaxy-cluster (G-C) distances; and we fill histograms of d with weights $0.033^2/d^2$ or $0.033^2 F_i F_j / d^2$, where F_i and F_j are absolute luminosities; see [1] for details. In the present analysis we have off-set the bins of redshift z with respect to Reference [1] to obtain different background fluctuations.

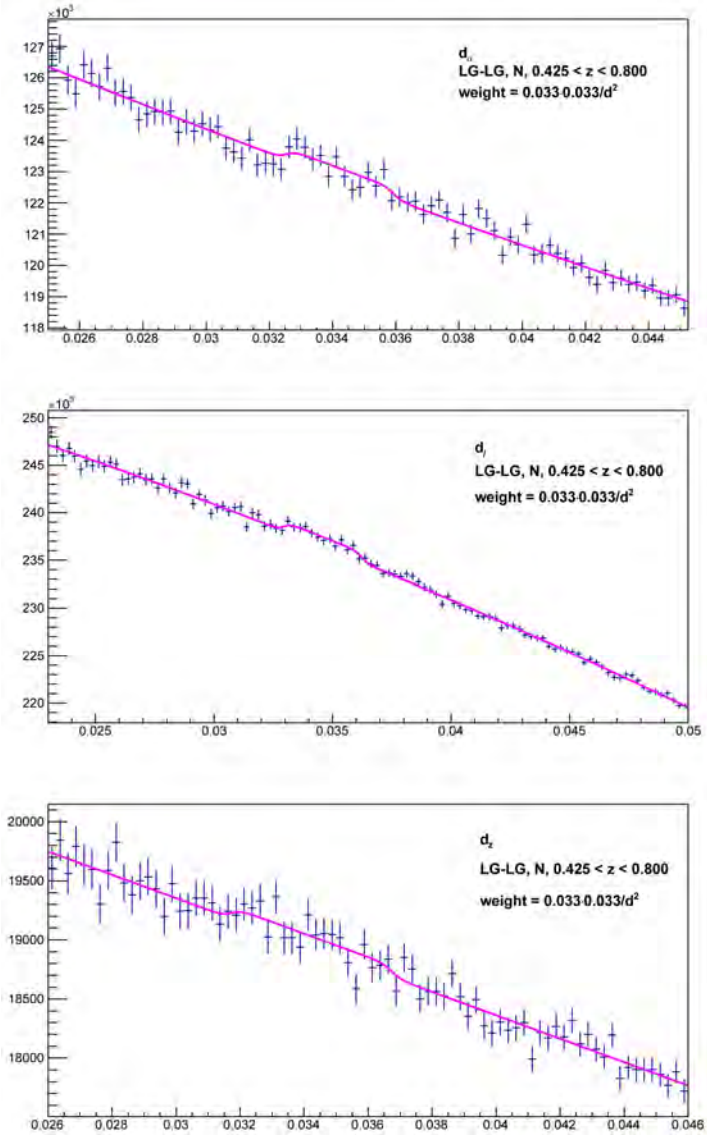

Figure 2. Fits to histograms of LG-LG distances d that obtain $\hat{d}_\alpha$, $\hat{d}_l$, or $\hat{d}_z$ at $z = 0.56$. See **Table 1** and **Table 2** for details.

Now consider pattern recognition. **Figure 1** and **Figure 2** show that the BAO signal is approximately constant from $d \approx 0.032$ to ≈0.037, corresponding to ≈137 Mpc to ≈158 Mpc. This characteristic shape of the BAO signal can be understood qualitatively with reference to **Figure 1** of [8]: the radial mass profile of an initial point like adiabatic excess results, well after recombination, in peaks at radii 17 Mpc and $r_{\text{drag}} \approx 148$ Mpc, so we can expect the BAO signal to extend from approximately 148-17 Mpc to 148+17 Mpc, with r_{drag} at the mid-point. From galaxy simulations described in [5], the smearing of r_{drag} due to galaxy peculiar motions has a standard deviation approximately 7.6 Mpc at $z = 0.5$, and 8.5 Mpc at $z = 0.3$. So the observed BAO signal has an unexpected "step-up-step-down" shape, and is narrower than implied by the simulation in reference [8].

The selections of galaxies are as in [1] with the added requirements for SDSS DR14 galaxies that they be "sciencePrimary" and "bossPrimary", and have a smaller redshift uncertainty zErr < 0.00025.

The fitting function has 6 free parameters, corresponding to a second degree polynomial for the background, and a "smooth step-up-step-down" function (described in [1]) with a center $\hat{d}$, a half-width Δ, and an amplitude A relative to the background. Each fit used for the final measurements is required to have a significance $A/\sigma_A > 2$ (in the analysis of [1] this requirement was $A/\sigma_A > 1$, which allows more bins of z).

Successful triplets of fits are presented in **Table 1**. Note the redundancy of measurements with $0.250 < z < 0.425$ and $0.425 < z < 800$. The independent triplets of fits selected for further analysis, are indicated with a "*", and are shown in **Figure 1** and **Figure 2**, with further details presented in **Table 2**. We note that each measurement of $\hat{d}_\alpha$, $\hat{d}_/$, or $\hat{d}_z$ in **Table 1**, together with the sound horizon angle θ_* obtained by the Planck experiment [3], is a sensitive measurement of Ω_m as shown in **Table 3**.

Table 1. Measured BAO distances $\hat{d}_\alpha$, $\hat{d}_/$, and $\hat{d}_z$, in units of c/H_0, with $z_c = 3.79$ (see [1]) from SDSS DR14 galaxies with right ascension 110° to 270°, and declination −5° to 70°, in the northern (N) and/or southern (S) galactic caps. Uncertainties are statistical from the fits to the BAO signal. No corrections have been applied. The independent measurements with a "*" are selected for further analysis. The corresponding fits are presented in **Figure 1** and **Figure 2**, and details are presented in **Table 2**. For comparison, measurements with a "&" correspond to SDSS DR13 data with the galaxy selections of [1].

z	z_{min}	z_{max}	Galaxies	Centers	Type	$100\hat{d}_\alpha$	$100\hat{d}_/$	$100\hat{d}_z$	Q
0.53	0.425	0.725	614,724	614,724	G-G, N+S	3.488 ± 0.015	3.504 ± 0.019	3.466 ± 0.032	1.007
0.53	0.425	0.725	614,724	13,960	G-C, N+S	3.381 ± 0.030	3.401 ± 0.033	3.395 ± 0.035	1.004
0.53	0.475	0.575	180,696	53,519	G-LG, N	3.424 ± 0.015	3.314 ± 0.018	3.242 ± 0.018	0.991
0.53	0.475	0.575	53,519	53,519	LG-LG, N	3.451 ± 0.030	3.447 ± 0.059	3.351 ± 0.022	1.012
0.53	0.475	0.575	180,696	5045	G-C, N	3.427 ± 0.031	3.331 ± 0.030	3.316 ± 0.033	0.986
0.56	0.425	0.800	230,841	230,841	G-G, S	3.441 ± 0.027	3.422 ± 0.017	3.497 ± 0.040	0.988
0.56	0.425	0.800	355,737	120,499	G-LG, N	3.425 ± 0.015	3.465 ± 0.016	3.351 ± 0.025	1.021
*0.56	0.425	0.800	120,499	120,499	LG-LG, N	3.424 ± 0.021	3.461 ± 0.018	3.424 ± 0.039	1.011
&0.56	0.425	0.800	143,778	143,778	LG-LG, N	3.424 ± 0.014	3.478 ± 0.015	3.451 ± 0.026	1.012
0.56	0.425	0.800	586,578	13,206	G-C, N+S	3.453 ± 0.038	3.365 ± 0.044	3.354 ± 0.028	0.987
0.52	0.425	0.575	236,693	236,693	G-G, N	3.437 ± 0.031	3.423 ± 0.026	3.432 ± 0.025	0.997
0.52	0.425	0.575	236,693	72,297	G-LG, N	3.416 ± 0.017	3.441 ± 0.012	3.385 ± 0.018	1.011
0.52	0.425	0.575	72,297	72,297	LG-LG, N	3.456 ± 0.033	3.447 ± 0.022	3.392 ± 0.060	1.006
0.48	0.425	0.525	151,938	4143	G-C, N	3.424 ± 0.051	3.383 ± 0.026	3.343 ± 0.062	0.998
0.36	0.250	0.450	114,597	114,597	G-G, N	3.456 ± 0.018	3.386 ± 0.015	3.318 ± 0.056	0.997
0.36	0.250	0.450	114,597	65,130	G-LG, N	3.455 ± 0.010	3.358 ± 0.015	3.293 ± 0.032	0.992
0.36	0.250	0.450	65,130	65,130	LG-LG, N	3.462 ± 0.016	3.352 ± 0.025	3.307 ± 0.039	0.988
0.34	0.250	0.425	92,321	92,321	G-G, N	3.439 ± 0.013	3.473 ± 0.015	3.423 ± 0.076	1.012
0.34	0.250	0.425	149,849	149,849	G-G, N+S	3.437 ± 0.014	3.367 ± 0.013	3.444 ± 0.042	0.979
*0.34	0.250	0.425	92,321	55,980	G-LG, N	3.449 ± 0.008	3.471 ± 0.013	3.450 ± 0.034	1.006
&0.34	0.250	0.425	133,729	94,873	G-LG, N	3.431 ± 0.011	3.469 ± 0.014	3.383 ± 0.024	1.017
0.34	0.250	0.425	55,980	55,980	LG-LG, N	3.467 ± 0.019	3.477 ± 0.015	3.459 ± 0.045	1.004

Table 2. Details of the fits selected for the final analysis (indicated by a "*" in **Table 1**). Note that the significance of the fitted signal amplitudes (relative to the background) A range from $A/\sigma_A = 2.1$ to 9.8.

Observable	z	Relative amplitude A	Half-width Δ
$\hat{d}_\alpha$	0.56	0.00290 ± 0.00100	0.00169 ± 0.00022
$\hat{d}_/$	0.56	0.00422 ± 0.00069	0.00164 ± 0.00020
$\hat{d}_z$	0.56	0.00505 ± 0.00226	0.00250 ± 0.00041
$\hat{d}_\alpha$	0.34	0.00632 ± 0.00064	0.00225 ± 0.00008
$\hat{d}_/$	0.34	0.00269 ± 0.00044	0.00197 ± 0.00013
$\hat{d}_z$	0.34	0.00341 ± 0.00162	0.00238 ± 0.00035

Table 3. Calculated d_{drag}, $\hat{d}_\alpha$, $\hat{d}_/$, and $\hat{d}_z$ for $z = 0.56$ and $z = 0.34$, as a function of Ω_m, for $\Omega_k = 0$ and $\Omega_{\text{de}}(a) \equiv \Omega_\Lambda$ constant. d_{drag} is the BAO galaxy comoving standard ruler length in units of c/H_0. It is calculated from $d_{\text{drag}} = 1.0184 d_*$, $d_* \equiv \theta_* \chi(z_*)$, $\theta_* = 0.0104092$, $\chi(z_*) \equiv \int_0^{z_*} \mathrm{d}z/E(z)$, $E(a) = \left(\Omega_m/a^3 + \Omega_r/a^4 + \Omega_\Lambda + \Omega_k/a^2\right)^{1/2}$, and $a = 1/(1+z)$. $\hat{d}_\alpha$, $\hat{d}_/$, and $\hat{d}_z$ are calculated with Equations (5), (6), and (7) of [1] with $z_c = 3.79$. The dependence on $h = 0.7$ or $\sum m_\nu = 0.27$ eV is negligible compared to the uncertainties in **Table 5**.

Ω_m	$100 d_{\text{drag}}$	$100\hat{d}_\alpha$	$100\hat{d}_/$	$100\hat{d}_z$	$100\hat{d}_\alpha$	$100\hat{d}_/$	$100\hat{d}_z$
			$z = 0.56$			$z = 0.34$	
0.25	3.628	3.535	3.510	3.477	3.560	3.538	3.510
0.27	3.519	3.457	3.444	3.427	3.471	3.457	3.440
0.28	3.468	3.421	3.414	3.405	3.429	3.420	3.408
0.29	3.420	3.386	3.385	3.384	3.390	3.385	3.377
0.31	3.330	3.323	3.333	3.346	3.317	3.319	3.321
0.33	3.248	3.265	3.285	3.311	3.251	3.259	3.271

The peculiar motion corrections were studied with the galaxy generator described in [5] [9]. Results of these simulations are shown in **Table 4**, for G-G distances, for two cases: "correct $P(k)$" and "correct $P_{\text{gal}}(k)$". The "correct $P(k)$" simulations have the predicted linear power spectrum of density fluctuations $P(k)$ of the ΛCDM model (Equation (8.1.42) of [10]), while the "correct $P_{\text{gal}}(k)$" simulations have a steeper $P(k)$ input so that the generated galaxy power spectrum $P_{\text{gal}}(k)$ matches observations, see Figure 15 of [5]. (The need for the steeper $P(k)$ is currently not understood.) All of these G-G corrections, and also the corrections for LG-LG and G-C, are in agreement, to within a factor 2, with the corrections applied in [1] that where taken from a study in [11]. In summary, in the present analysis we apply the same peculiar motion corrections as in [1], *i.e.* we multiply the measured BAO distances $\hat{d}_\alpha$, $\hat{d}_/$, and $\hat{d}_z$, by correction factors f_α, $f_/$, and f_z, respectively, where

Table 4. Study of peculiar motion corrections to be added to the G-G measurements of $\hat{d}_\alpha$, $\hat{d}_/$, and $\hat{d}_z$ in Table 1, obtained from simulations.

z	Simulation	$\Delta\hat{d}_\alpha$	$\Delta\hat{d}_/$	$\Delta\hat{d}_z$
0.5	correct $P(k)$	0.000062	0.000080	0.000112
0.5	correct $P_{\text{gal}}(k)$	0.000096	0.000125	0.000175
0.3	correct $P(k)$	0.000063	0.000080	0.000111
0.3	correct $P_{\text{gal}}(k)$	0.000084	0.000107	0.000148

$$\begin{aligned} f_\alpha - 1 &= 0.00320 \cdot a^{1.35}, \\ f_/ - 1 &= 0.00350 \cdot a^{1.35}, \\ f_z - 1 &= 0.00381 \cdot a^{1.35}. \end{aligned} \tag{1}$$

We take half of these corrections as a systematic uncertainty. The effect of these corrections is relatively small as shown in Table 6.

Uncertainties of $\hat{d}_\alpha$, $\hat{d}_/$, and $\hat{d}_z$ are presented in Table 5. These uncertainties are dominated by cosmological and statistical fluctuations, and are estimated from the root-mean-square fluctuations of many measurements, from the width of the distribution of Q, and from the issues discussed in the **Appendix**.

Fits to the two independent selected triplets $\hat{d}_\alpha$, $\hat{d}_/$, and $\hat{d}_z$ indicated by a "*" in Table 1, with the uncertainties in Table 5, are presented in Table 6.

Four Scenarios are considered. In Scenario 1 the dark energy density is constant, *i.e.* $\Omega_{\text{de}}(a) = \Omega_\Lambda$. In Scenario 2 the observed acceleration of the expansion of the universe is due to a gas of negative pressure with an equation of state $w \equiv p/\rho < 0$. We allow the index w to be a function of a [12] [13]: $w(a) = w_0 + w_a(1-a)$. Scenario 3 is the same as Scenario 2, except that w is constant, *i.e.* $w_a = 0$. In Scenario 4 we assume $\Omega_{\text{de}}(a) = \Omega_{\text{de}}\left[1 + w_1(1-a)\right]$.

Note in Table 6 that Ω_k is consistent with zero, and $\Omega_{\text{de}}(a)$ is consistent with being independent of the expansion parameter a. For $\Omega_k = 0$ and $\Omega_{\text{de}}(a) \equiv \Omega_\Lambda$ constant we obtain from Table 6:

$$\Omega_m = 0.288 \pm 0.037, \tag{2}$$

with $\chi^2 = 1.0$ for 4 degrees of freedom.

Final calculations are done with fits and numerical integrations. Never-theless, it is convenient to present approximate analytical expressions obtained from the numerical integrations for the case of flat space and a cosmological constant. At decoupling, $z_* = 1089.92 \pm 0.25$ from the Planck "TT, TE, EE + lowE + lensing" measurement [3]. The "angular distance" at decoupling is $D_A(z_*) \equiv \chi(z_*) a_* c/H_0$, with

$$\chi(z_*) = 3.2675 \left(\frac{h + 0.35\sum m_\nu}{0.7}\right)^{0.01} \left(\frac{0.28}{\Omega_m}\right)^{0.4}, \tag{3}$$

which has negligible dependence on h or $\sum m_\nu$.

Table 5. Uncertainties of $\hat{d}_\alpha$, $\hat{d}_/$, and $\hat{d}_z$ at 68% confidence. For "*et al.*" see the **Appendix**.

	$\hat{d}_\alpha$	$\hat{d}_/$	$\hat{d}_z$
Method	±0.00003	±0.00004	±0.00008
Peculiar motion correction	±0.00004	±0.00004	±0.00005
Cosmological *et al.* + statistical fluctuations	±0.00029	±0.00055	±0.00070
Total	±0.00030	±0.00055	±0.00071

Table 6. Cosmological parameters obtained from the 6 independent galaxy BAO measurements indicated with a "*" in **Table 1** in several scenarios. Corrections for peculiar motions are given by Equation (1) except, for comparison, the fit "1*" which has no correction. Scenario 1 has $\Omega_{de}(a)$ constant. Scenario 3 has $w = w_0$. Scenario 4 has $\Omega_{de}(a) = \Omega_{de}\left[1 + w_1(1-a)\right]$.

	Scenario 1*	Scenario 1	Scenario 1	Scenario 3	Scenario 4	Scenario 4
Ω_k	0 fixed	0 fixed	0.267 ± 0.362	0 fixed	0 fixed	0.262 ± 0.383
$\Omega_{de} + 0.6\Omega_k$	0.712 ± 0.037	0.712 ± 0.037	0.738 ± 0.050	0.800 ± 0.364	0.760 ± 0.151	0.745 ± 0.148
w_0	n.a.	n.a.	n.a.	-0.76 ± 0.65	n.a.	n.a.
w_1	n.a.	n.a.	n.a.	n.a.	0.71 ± 2.00	0.13 ± 2.77
$100 d_{drag}$	3.48 ± 0.06	3.487 ± 0.052	3.48 ± 0.06	3.43 ± 0.16	3.42 ± 0.19	3.48 ± 0.21
χ^2/d.f.	0.9/4	1.0/4	0.4/3	0.9/3	0.9/3	0.4/2

From the Planck "TT, TE, EE + lowE + lensing" measurement [3], $\theta_* = 0.0104092 \pm 0.0000031$. Then the comoving sound horizon at decoupling is $r_* \equiv d_* c / H_0$, with

$$d_* = \theta_* \chi(z_*) = 0.03401 \left(\frac{0.28}{\Omega_m} \right)^{0.4}. \quad (4)$$

The BAO standard ruler for galaxies r_{drag} is larger than r_* because last scattering of electrons occurs after last scattering of photons due to their different number densities. In the present analysis, we take $r_{drag} \equiv d_{drag} c / H_0$ with

$$\frac{d_{drag}}{d_*} = 1.0184 \pm 0.0004, \quad (5)$$

from the Planck "TT, TE, EE + lowE + lensing" analysis, with the uncertainty from Equation (10) of Reference [3]. Note from (4) and Equation (10) of Reference [3] that (5) is insensitive to cosmological parameters, so the uncalibrated analysis decouples from h or $\sum m_\nu$.

We can test (5) experimentally. From **Table 6** we obtain $d_{drag} = 0.03487 \pm 0.00052$. From (4) and (2) we obtain $d_* = 0.03363 \pm 0.00174$, so the measured $d_{drag}/d_* = 1.037 \pm 0.056$.

To the 6 independent galaxy BAO measurements, we add the sound horizon angle θ_*, and obtain the results presented in **Table 7**. Note that measurements

Table 7. Cosmological parameters obtained from the 6 independent galaxy BAO measurements indicated with a "*" in **Table 1**, plus θ_* from the Planck experiment, in several scenarios. Corrections for peculiar motions are given by Equation (1). $d_{\text{drag}}/d_* = 1.0184 \pm 0.0004$. Scenario 1 has $\Omega_{\text{de}}(a)$ constant. Scenario 2 has $w(a) = w_0 + w_a(1-a)$. Scenario 3 has $w = w_0$. Scenario 4 has $\Omega_{\text{de}}(a) = \Omega_{\text{de}}\left[1 + w_1(1-a)\right]$.

	Scenario 1	Scenario 1	Scenario 2	Scenario 3	Scenario 4	Scenario 4
Ω_k	0 fixed	0.008 ± 0.018	0 fixed	0 fixed	0 fixed	-0.007 ± 0.101
$\Omega_{\text{de}} + 2.1\Omega_k$	0.7276 ± 0.0047	0.724 ± 0.009	0.708 ± 0.080	0.724 ± 0.008	0.723 ± 0.011	0.723 ± 0.011
w_0	n.a.	n.a.	-0.77 ± 1.47	-0.95 ± 0.10	n.a.	n.a.
w_a or w_1	n.a.	n.a.	-0.91 ± 4.53	n.a.	0.19 ± 0.41	0.35 ± 2.20
$100 d_*$	3.443 ± 0.024	3.42 ± 0.06	3.35 ± 0.04	3.41 ± 0.07	3.41 ± 0.09	3.39 ± 0.20
χ^2/d.f.	1.2/5	1.0/4	0.9/3	1.0/4	1.0/4	1.0/3

are consistent with flat space and a cosmological constant. Note also that the constraint on Ω_k becomes tighter if $\Omega_{\text{de}}(a)$ is assumed constant, and that the constraint on $\Omega_{\text{de}}(a)$ becomes tighter if Ω_k is assumed zero. In the scenario of flat space and a cosmological constant we obtain

$$\Omega_m = 0.2724 \pm 0.0047, \tag{6}$$

with $\chi^2 = 1.2$ for 5 degrees of freedom. This is the final result of the present analysis.

Adding two measurements in the quasar Lyman-alpha forest [1] [14] [15] we obtain the results presented in **Table 8**. In particular, for flat space and a cosmological constant we obtain

$$\Omega_m = 0.2714 \pm 0.0047, \tag{7}$$

with $\chi^2 = 10.0$ for 7 degrees of freedom. Note that the Lyman-alpha measurements tighten the constraints on Ω_k, w_0, w_1, and w_a.

As a cross-check of the z dependence, from the 4 independent fits to $\hat{d}_\alpha$ at different redshifts z presented in **Figure 3**, plus θ_*, we obtain

$$\Omega_m = 0.2745 \pm 0.0040, \tag{8}$$

with $\chi^2 = 3.0$ for 3 degrees of freedom, for flat space and a cosmological constant.

As a cross-check of isotropy, from the 3 independent fits to $\hat{d}_\alpha$ at $z = 0.36$ shown in **Figure 4** corresponding to different regions of the sky, we obtain

$$\Omega_m = 0.2737 \pm 0.0043, \tag{9}$$

with $\chi^2 = 1.1$ for 2 degrees of freedom, for flat space and a cosmological constant.

To check the stability of $\hat{d}_\alpha$, $\hat{d}_/$, and $\hat{d}_z$ with the data set and galaxy selections, we compare fits highlighted with "*" and "&" in **Table 1**, and also fits in **Figure 5**.

Additional studies are presented in the **Appendix**.

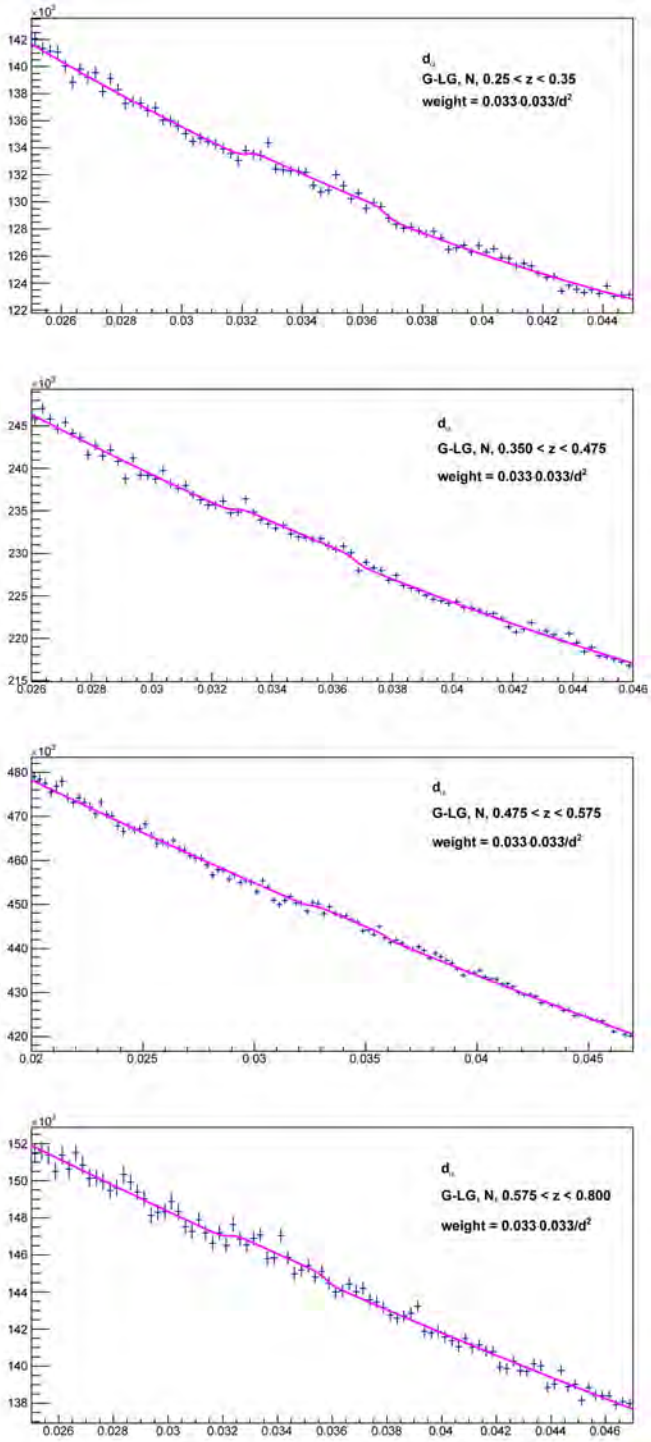

Figure 3. Fits to histograms of G-LG distances d that obtain $\hat{d}_\alpha$ at $z = 0.32, 0.42, 0.53$, and 0.65. The bins of z are $(0.25, 0.35)$, $(0.35, 0.475)$, $(0.475, 0.575)$, and $(0.575, 0.800)$, respectively. The fits obtain $\hat{d}_\alpha = 0.03447 \pm 0.00012$, 0.03478 ± 0.00012, 0.03424 ± 0.00015, and 0.03399 ± 0.00020 respectively, where uncertainties are statistical from the fits. A fit with these four measurements (with the total uncertainties of **Table 5**), plus θ_* from the Planck experiment, obtains $\Omega_m = 0.2745 \pm 0.0040$ and $d_* = 0.03433 \pm 0.00020$ with $\chi^2 = 3.0$ for 3 degrees of freedom.

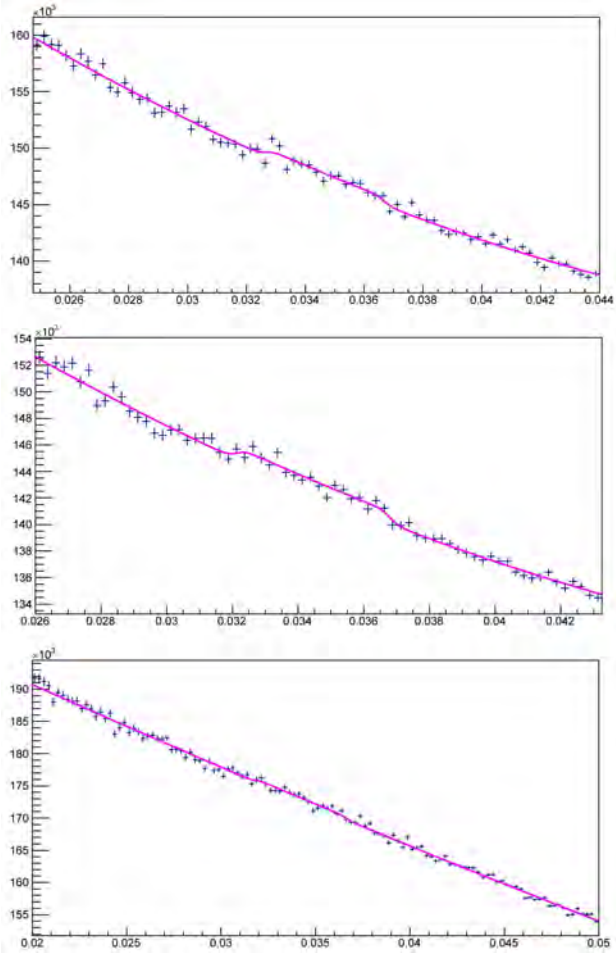

Figure 4. Fits to histograms of G-LG distances d, with z in the range 0.25 - 0.45, that obtain $\hat{d}_\alpha$ at $z = 0.36$. From top to bottom, they correspond to the northern galactic cap with right ascension < 180˚ (NW), to the northern galactic cap with right ascension > 180˚ (NE), and to the southern galactic cap (S). The fits obtain $\hat{d}_\alpha = 0.03468 \pm 0.00012$, 0.03447 ± 0.00012, and 0.03424 ± 0.00019 respectively, where uncertainties are statistical from the fits. A fit with these three measurements (with the total uncertainties of **Table 5**), plus θ_* from the Planck experiment, obtains $\Omega_m = 0.2737 \pm 0.0043$ and $d_* = 0.03437 \pm 0.00022$ with $\chi^2 = 1.1$ for 2 degrees of freedom.

Table 8. Cosmological parameters obtained from the 6 galaxy BAO measurements indicated with a "*" in **Table 1**, plus θ_* from the Planck experiment, plus two Lyman-alpha measurements [1] [14] [15] in several scenarios. Corrections for peculiar motions are given by Equation (1). $d_{\text{drag}}/d_* = 1.0184 \pm 0.0004$. Scenario 1 has $\Omega_{\text{de}}(a)$ constant. Scenario 2 has $w(a) = w_0 + w_a(1-a)$. Scenario 3 has $w = w_0$. Scenario 4 has $\Omega_{\text{de}}(a) = \Omega_{\text{de}}\left[1 + w_1(1-a)\right]$.

	Scenario 1	Scenario 1	Scenario 2	Scenario 3	Scenario 4	Scenario 4
Ω_k	0 fixed	-0.011 ± 0.008	0 fixed	0 fixed	0 fixed	-0.022 ± 0.010
$\Omega_{\text{de}} + 2.1\Omega_k$	0.7286 ± 0.0047	0.734 ± 0.006	0.703 ± 0.028	0.726 ± 0.008	0.723 ± 0.011	0.720 ± 0.011
w_0	n.a.	n.a.	-0.70 ± 0.33	-0.96 ± 0.09	n.a.	n.a.
w_a or w_1	n.a.	n.a.	-1.18 ± 1.37	n.a.	0.24 ± 0.40	0.80 ± 0.49
$100 d_*$	3.449 ± 0.024	3.48 ± 0.04	3.32 ± 0.13	3.42 ± 0.07	3.40 ± 0.08	3.34 ± 0.09
χ^2/d.f.	10.0/7	7.7/6	8.0/5	9.2/6	9.0/6	4.6/5

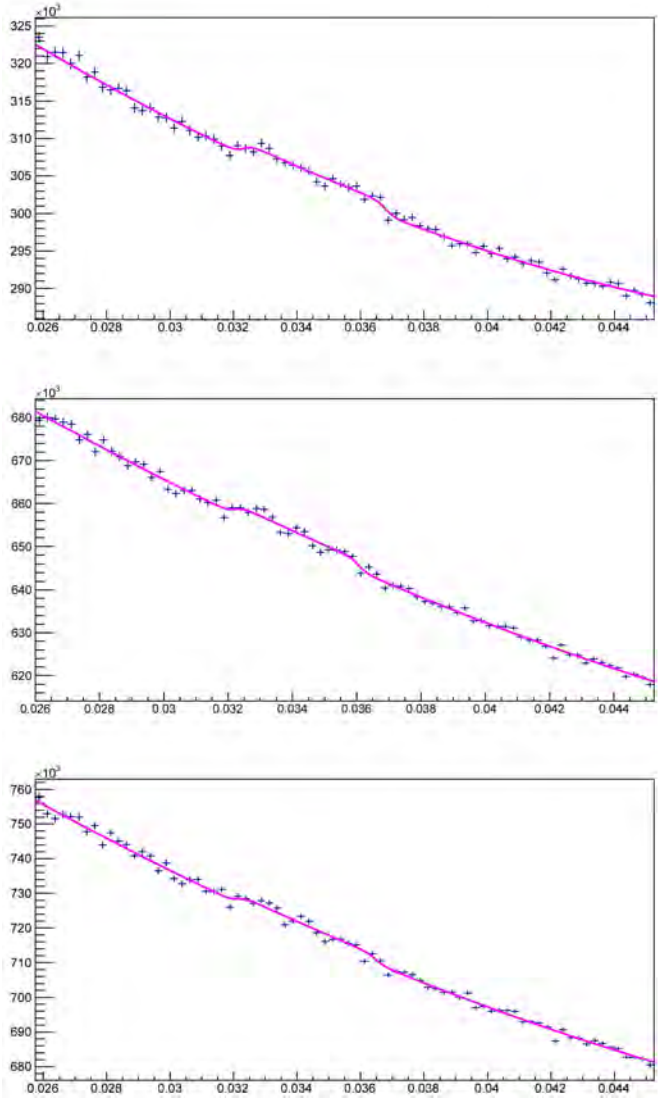

Figure 5. Fits to histograms of G-LG distances d, with z in the range 0.25 - 0.45 for the northern galactic cap (N), that obtain $\hat{d}_\alpha$ at $z = 0.36$. From top to bottom, they correspond to SDSS DR14 (this analysis), DR14 with galaxy selections of [1], and DR13 with galaxy selections of [1]. The fits obtain $\hat{d}_\alpha = 0.03455 \pm 0.00010$, 0.03416 ± 0.00010, and 0.03431 ± 0.00012 respectively, where uncertainties are statistical from the fits. Note that our assigned total uncertainty for $\hat{d}_\alpha$ is ±0.00030. This single fit for the current analysis, together with θ_* obtains $\Omega_m = 0.272 \pm 0.007$ and $d_* = 0.0345 \pm 0.0004$, with zero degrees of freedom. The relative amplitudes A of the fitted signals are 0.00552 ± 0.00060, 0.00369 ± 0.00042, and 0.00341 ± 0.00039 respectively. The number of galaxies (G) and large galaxies (LG) are $(114597, 65130)$, $(153783, 101504)$, and $(160943, 107971)$, respectively. Note that the relative amplitude is larger for the current galaxy selections.

3. Measurement of H_0 with BAO as a *Calibrated* Standard Ruler

We consider the scenario of flat space and a cosmological constant. It is useful to

present approximate analytic expressions, tho all final calculations are done directly with fits to the measurements marked with a "*" in Table 1 and numerical integrations to obtain correct uncertainties for correlated parameters. To calibrate the BAO measurements, we integrate the comoving photon-electron-baryon plasma sound speed from $t = 0$ up to decoupling and obtain the "comoving acoustic horizon distance" $r_* \equiv d_* c / H_0$, with

$$d_* = 0.03407 \left(\frac{h + 0.026 \sum m_\nu}{0.7} \right)^{0.513} \left(\frac{0.28}{\Omega_m} \right)^{0.244} \left(\frac{0.0225}{\Omega_b h^2} \right)^{0.097} . \quad (10)$$

The acoustic angular scale is

$$\theta_* \equiv \frac{d_*}{\chi(z_*)} = 0.010427 \left(\frac{h + 0.020 \sum m_\nu}{0.70} \right)^{0.503} \left(\frac{\Omega_m}{0.28} \right)^{0.156} \left(\frac{0.0225}{\Omega_b h^2} \right)^{0.097} , \quad (11)$$

in agreement with Equation (11) of [3].

Let us now consider the measurement of *h*. From the galaxy BAO measurements in Table 6 we obtain $\Omega_m = 0.288 \pm 0.037$ and $d_{\text{drag}} = 0.03487 \pm 0.00052$. From Big Bang Nucleosynthesis, $\Omega_b h^2 = 0.0225 \pm 0.0008$ at 68% confidence [4]. From this data and Equations (5) and (10), or the corresponding fit, we obtain

$$h + 0.026 \sum m_\nu = 0.716 \pm 0.027, \quad (12)$$

with $\chi^2 = 1.0$ for 4 degrees of freedom.

The Planck measurement of θ_* allows a more precise measurement of *h*. From Table 7, we obtain $\Omega_m = 0.2724 \pm 0.0047$. Then from Big Bang Nucleosynthesis and (11), or the corresponding fit, we obtain

$$h + 0.020 \sum m_\nu = 0.7038 \pm 0.0060, \quad (13)$$

with $\chi^2 = 1.2$ for 5 degrees of freedom. Note that the uncertainties of *h* and Ω_m are correlated through Equation (11).

4. Studies of CMB Fluctuations

In Table 9, we present a qualitative study of the sensitivity of the CMB power spectrum $l(l+1)C_{TT,l}^S / (2\pi)$ to constrain Ω_m and $\sum m_\nu$. We use the approximate analytic expression (7.2.41) of [10], modified to include $\sum m_\nu$, to compare the spectra with Planck 2018 "TT, TE, EE + lowE + lensing" parameters with the best fit spectra with fixed values $\Omega_m = 0.2854$ and $\sum m_\nu = 0.06, 0.1, 0.2, 0.3, 0.4, 0.5$ eV. We find that the differences in spectra range from 0.11% to 0.3% of the first acoustic peak, see Figure 6. So the CMB power spectrum, while being very sensitive to constrain θ_*, has low sensitivity to constrain Ω_m or $\sum m_\nu$.

In view of the low sensitivity of the CMB power spectra to constrain Ω_m, the Planck analysis can benefit from a combination with the direct measurement of Ω_m given by Equation (6). The combination, obtained with the "base_mnu_plikHM_TTTEEE_lowTEB_lensing_*.txt MC chains" made public by the Planck Collaboration [3], is presented in Table 10. This combination is preliminary due to the sparseness of the MC chains at low values of Ω_m.

Table 9. Cosmologies with fixed Ω_m and $\sum m_\nu$ fitted to the CMB power spectrum $l(l+1)C_{TT,l}^S/(2\pi)$ with the Planck 2018 "TT, TE, EE + lowE + lensing" parameters $\Omega_m = 0.3153$, $\sum m_\nu = 0.06$ eV, $h = 0.6736$, $\Omega_b h^2 = 0.02237$, $n_s = 0.9649$, $N^2 = 1.670 \times 10^{-10}$, and $\tau = 0.0544$ [3]. The approximate analytic Equation (7.2.41) of [10] (modified to include $\sum m_\nu$) was used. Notation: $N^2 \equiv A_s/(4\pi) \equiv \Delta_R^2/(4\pi)$.

Ω_m	0.2854	0.2854	0.2854	0.2854	0.2854	0.2854
$\sum m_\nu$ [eV]	0.06	0.1	0.2	0.3	0.4	0.5
h	0.6980	0.6976	0.6965	0.6954	0.6942	0.6931
$100\Omega_b h^2$	2.282	2.288	2.306	2.324	2.343	2.362
n_s	0.9692	0.9699	0.9716	0.9735	0.9754	0.9774
$10^{10} N^2$	1.730	1.729	1.725	1.722	1.716	1.713
τ	0.0774	0.0778	0.0787	0.0797	0.0799	0.0809
r.m.s. [μK²]	6.07	6.98	9.29	11.66	14.06	16.49

Table 10. Combination of the Planck 2018 "TT, TE, EE + lowE + lensing" analysis [3] with the directly measured $\Omega_m = 0.2724 \pm 0.0047$. Uncertainties are at 68% confidence. The Planck $\chi_P^2 \equiv -2 \cdot \ln \mathcal{L}$ increases from 12,956.78 to 12,968.64 with this combination. The galaxy $\chi_G^2 \equiv (\Omega_m - 0.2724)^2/0.0047^2$. Preliminary.

	Planck	Planck + Ω_m
$\Omega_b h^2$	0.02237 ± 0.00015	0.02265 ± 0.00012
$\Omega_c h^2$	0.1200 ± 0.0012	0.1155 ± 0.0005
$100\theta_*$	1.04092 ± 0.00031	1.04125 ± 0.00022
τ	0.0544 ± 0.0073	0.078 ± 0.006
$\ln 10^{10} A_s$	3.044 ± 0.014	3.102 ± 0.020
n_s	0.9649 ± 0.0042	0.9726 ± 0.0017
Ω_Λ	0.6847 ± 0.0073	0.7147 ± 0.0040
Ω_m	0.3153 ± 0.0073	0.2853 ± 0.0040
h	0.6736 ± 0.0054	0.6990 ± 0.0030
σ_8	0.8111 ± 0.0060	0.8346 ± 0.0054
χ_P^2	12,956.78	12,968.64
χ_G^2	83.31	7.53
χ_{tot}^2	13,040.09	12,976.17

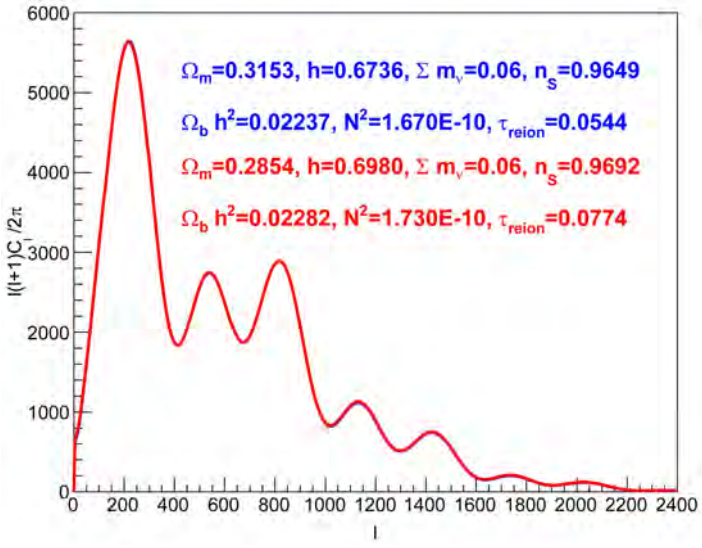

Figure 6. Comparison of the power spectra $l(l+1)C_{TT,l}^{S}/(2\pi)$ [μK²] for the Planck 2018 "TT, TE, EE + lowE + lensing" parameters, with the best fit spectra with $\Omega_m = 0.2854$ and $\sum m_\nu = 0.06$ eV fixed, calculated with the approximate Equation (7.2.41) of [10] (modified to include $\sum m_\nu$). The r.m.s. difference is 6.07 μK², corresponding to 0.11% of the first acoustic peak, so the two spectra can not be distinguished by eye.

5. Tensions

We consider four direct measurements: 1) $h = 0.7348 \pm 0.0166$ by the Sh_0es Team [16], 2) $\sigma_8 \approx \left[0.746 \pm 0.012(stat) \pm 0.022(syst)\right](0.3/\Omega_m)^{0.47}$ from the abundance of rich galaxy clusters [4] [17], 3) $\sigma_8 \approx \left[0.745 \pm 0.039\right](0.3/\Omega_m)^{0.5}$ from weak gravitational lensing [4] [18], and 4) $\Omega_m = 0.2724 \pm 0.0047$ from galaxy BAO and θ_* from Planck, Equation (6) of this analysis. Comparing these measurements with Planck (left hand column of **Table 10**) we obtain differences of 3.5σ, 2.5σ, 1.8σ, and 4.9σ, respectively. Comparing these measurements with the Planck + Ω_m combination (right hand column of **Table 10**) we obtain differences of 2.1σ, 2.3σ, 1.5σ, and 2.1σ, respectively. In conclusion, the Planck + Ω_m combination reduces the tensions with the direct measurements. Note that the Planck + Ω_m combination has σ_8 greater than the direct measurements. This 2.7σ tension may be due to neutrino masses.

6. Update on Neutrino Masses

We consider the scenario of three neutrino flavors with eigenstates of nearly the same mass, so $\sum m_\nu \approx 3m_\nu$. Massive neutrinos suppress the power spectrum of linear density fluctuations $P(k)$ by a factor $1 - 8\Omega_\nu/\Omega_m$ for $k \gg 0.018 \cdot \Omega_m^{1/2} \left(\sum m_\nu / 1\,\text{eV}\right)^{1/2} h$ Mpc^{-1} [19]. This suppression affects σ_8 and the galaxy power spectrum $P_{\text{gal}}(k)$, *but does not* affect the Sachs-Wolfe effect at low k. So, by comparing fluctuations at large and small k it is possible to constrain or measure $\sum m_\nu$ [5].

To obtain $\sum m_\nu$ we minimize a χ^2 with four terms corresponding to N^2,

σ_8, and two parameters obtained from the Planck + Ω_m combination: $h = 0.6990 \pm 0.0030$, and $n_s = 0.9726 \pm 0.0017$. In the fit, Ω_m is obtained from Equation (11), and $\Omega_b h^2 = 0.02265 \pm 0.00012$. σ_8 is obtained from the combination of the two direct measurements presented in Section 5.

For $N^2 = (2.08 \pm 0.33) \times 10^{-10}$ [5] obtained from the Sachs-Wolfe effect measured by the COBE satellite (see list of references in [10]) we obtain

$$\sum m_\nu = 0.45 \pm 0.20 \text{ eV}, \tag{14}$$

with zero degrees of freedom, in agreement with [5] where the method is explained in detail.

Since $\sum m_\nu < 1.7$ eV, neutrinos are still ultra-relativistic at decoupling. Then there is no power suppression of the CMB fluctuations, and we can use the entire spectrum to fix the amplitude N^2. From the Planck + Ω_m combination of **Table 10** we obtain $N^2 \equiv A_s/(4\pi) = (1.7700 \pm 0.0354) \times 10^{-10}$, and

$$\sum m_\nu = 0.26 \pm 0.08 \text{ eV}, \tag{15}$$

with zero degrees of freedom.

To strengthen the constraints from the two direct measurements of σ_8, we add to the fit measurements of fluctuations of number counts of galaxies in spheres of radii 16/*h*, 32/*h*, 64/*h*, and 128/*h* Mpc, as explained in [5]. We obtain

$$\sum m_\nu = 0.27 \pm 0.08 \text{ eV}, \tag{16}$$

with $\chi^2 = 1.6$ for 2 degrees of freedom, and find no significant pulls on N^2, *h*, or n_s. These results are sensitive to the accuracy of the direct measurements of σ_8.

Acknowledgements

We have used data in the publicly released Sloan Digital Sky Survey SDSS DR14 catalog.

Funding for the Sloan Digital Sky Survey (SDSS) has been provided by the Alfred P. Sloan Foundation, the Participating Institutions, the National Aeronautics and Space Administration, the National Science Foundation, the US Department of Energy, the Japanese Monbukagakusho, and the Max Planck Society. The SDSS Web site is http://www.sdss.org/.

The SDSS is managed by the Astrophysical Research Consortium (ARC) for the Participating Institutions. The Participating Institutions are The University of Chicago, Fermilab, the Institute for Advanced Study, the Japan Participation Group, The Johns Hopkins University, Los Alamos National Laboratory, the Max-Planck-Institute for Astronomy (MPIA), the Max-Planck-Institute for Astrophysics (MPA), New Mexico State University, University of Pittsburgh, Princeton University, the United States Naval Observatory, and the University of Washington.

We have also used data publicly released by the Planck Collaboration [3] in the form of "MC chains", and the corresponding analysis tool "GetDist GUI".

Conflicts of Interest

The author declares no conflicts of interest regarding the publication of this paper.

References

[1] Hoeneisen, B. (2017) Study of Baryon Acoustic Oscillations with SDSS DR13 Data and Measurements of Ω_k and $\Omega_{de}(a)$. *International Journal of Astronomy and Astrophysics*, **7**, 11-27. https://doi.org/10.4236/ijaa.2017.71002

[2] Patrignani, C., *et al.* (Particle Data Group) (2016) Review of Particle Physics. *Chinese Physics C*, **40**, 100001. https://doi.org/10.1088/1674-1137/40/10/100001

[3] Aghanim, N., *et al.* (2018) Planck 2018 Results. VI. Cosmological Parameters, arXiv:1807.06209.

[4] Tanabashi, M., *et al.* (Particle Data Group) (2018) The Review of Particle Physics. *Physical Review D*, **98**, 030001.

[5] Hoeneisen, B. (2018) Study of Galaxy Distributions with SDSS DR14 Data and Measurement of Neutrino Masses. *International Journal of Astronomy and Astrophysics*, **8**, 230-257. https://doi.org/10.4236/ijaa.2018.83017

[6] Blanton, M.R., *et al.* (2017) Sloan Digital Sky Survey IV: Mapping the Milky Way, Nearby Galaxies, and the Distant Universe. *The Astronomical Journal*, **154**, 28, 35.

[7] Dawson, K.S., *et al.* (2013) The Baryon Oscillation Spectroscopic Survey of SDSS-III. *The Astronomical Journal*, **145**, 10, 41.

[8] Eisenstein, D.J., Seo, H.-J. and White, M. (2007) On the Robustness of the Acoustic Scale in the Low-Redshift Clustering of Matter. *ApJ*, **664**, 660-674. https://doi.org/10.1086/518755

[9] Hoeneisen, B. (2000) A Simple Model of the Hierarchical Formation of Galaxies. arXiv:astro-ph/0009071.

[10] (2008) Steven Weinberg, Cosmology. Oxford University Press, Oxford.

[11] Seo, H.-J., *et al.* (2010) High-Precision Predictions for the Acoustic Scale in the Non-Linear Regime. *ApJ*, **720**, 1650. https://doi.org/10.1088/0004-637X/720/2/1650

[12] Chevallier, M. and Polarski, D. (2001) Accelerating Universes with Scaling Dark Matter. *International Journal of Modern Physics*, **D10**, 213. https://doi.org/10.1142/S0218271801000822

[13] Linder, E.V. (2003) Exploring the Expansion History of the Universe. *Physical Review Letters*, **90**, 091301. https://doi.org/10.1103/PhysRevLett.90.091301

[14] Font-Ribera, A., *et al.* (2014) Quasar-Lyman Forest Cross-Correlation from BOSS DR11: Baryon Acoustic Oscillations. *Journal of Cosmology and Astroparticle Physics*, **5**, arXiv:1311.1767. https://doi.org/10.1088/1475-7516/2014/05/027

[15] Delubac, T., *et al.* (2014) Baryon Acoustic Oscillations in the Lyα forest of BOSS DR11 Quasars. arXiv:1404.1801v2.

[16] Riess, A.G., Casertano, S., Yuan, W., *et al.* (2018) New Parallaxes of Galactic Cepheids from Spatially Scanning the Hubble Space Telescope: Implications for the Hubble Constant. *The Astrophysical Journal*, **861**, 126.

[17] Vikhlinin, A., *et al.* (2009) Chandra Cluster Cosmology Project III: Cosmological Parameter Constraints. *The Astrophysical Journal*, **692**, 1060-1074. https://doi.org/10.1088/0004-637X/692/2/1060

[18] Hildebrandt, H., *et al.* (2017) KiDS-450: Cosmological Parameter Constraints from

Tomographic Weak Gravitational Lensing. *Monthly Notices of the Royal Astronomical Society*, **465**, 1454-1498. https://doi.org/10.1093/mnras/stw2805

[19] Lesgourgues, J. and Pastor, S. (2006) Massive Neutrinos and Cosmology. *Physics Reports*, **429**, 307-379. https://doi.org/10.1016/j.physrep.2006.04.001

[20] Eisenstein, D.J. and Hu, W. (1997) Baryonic Features in the Matter Transfer Function.

Appendix

1) Comparison with Reference [1]

Table 4 and Table 5 of Reference [1] can be compared with Table 6 and Table 7 of the present analysis. We find agreement between all measurements when d in Reference [1] is identified with d_* in the present analysis. We find that d in Table 4 of Reference [1] is biased low with respect to d_{drag} in Table 6 of the present analysis. For the scenario of flat space and a cosmological constant, Table 4 of Reference [1] obtains $\Omega_m = 0.284 \pm 0.014$ and $d = 0.0339 \pm 0.0002$. From this Ω_m and Equation (4) we obtain $d_* = 0.0338 \pm 0.0007$, in good agreement with d, so in Reference [1] no correction for d_{drag}/d_* was needed or applied.

2) Bias of BAO measurements of small galaxy samples

We have investigated the difference of d_{drag} between Reference [1] and the present analysis. This difference is not due to the change of data set from SDSS DR13 to SDSS DR14: we have compared the coordinates of selected galaxies and have found no changes in calibrations. The fluctuation is not caused by the tighter galaxy selection requirements of the present analysis: compare the entries with "&" and "*" in Table 1, and see Figure 5.

As an extreme test, we divide the bin $0.425 < z < 0.725$ into 6 sub-samples: $0.425 < z < 0.525$ N, $0.525 < z < 0.625$ N, $0.625 < z < 0.725$ N, $0.425 < z < 0.525$ S, $0.525 < z < 0.625$ S, and $0.625 < z < 0.725$ S. We try to fit each one, and average the successful fits (only about half are successful), and obtain $\hat{d}_\alpha = 0.03358 \pm 0.00015$, $\hat{d}_/ = 0.03415 \pm 0.00027$, and $\hat{d}_z = 0.03335 \pm 0.00033$. We also fit the sum of these six bins, and obtain $\hat{d}_\alpha = 0.03496 \pm 0.00015$, $\hat{d}_/ = 0.03459 \pm 0.00010$, and $\hat{d}_z = 0.03464 \pm 0.00034$. So there is evidence that fits become biased low as the number of galaxies is reduced and the significance of the fitted relative amplitude A of the BAO signal becomes marginal. The reason is that the observed BAO signal has a sharper and larger lower edge at $d \approx 0.032$ compared to the upper edge at ≈0.037, so the upper edge tends to get lost in the background fluctuations as the number of galaxies is reduced.

To reduce this bias, in the present analysis we require the significance of the fitted relative amplitudes $A/\sigma_A > 2$, instead of >1 for Reference [1]. The price to pay is that we obtain only 2 independent bins of z, instead of 6.

3) A study of the BAO signal

The BAO signal has a "step-up-step-down" shape with center at $\hat{d}$ and half-width Δ. The widths of fits vary typically from $\Delta = 0.0017$ to 0.0025, see Table 2. We have used the center $\hat{d}$ as the BAO standard ruler, but could have used the lower edge of the signal at $\hat{d} - \Delta$, or the upper edge at $\hat{d} + \Delta$, or somewhere in between, *i.e.* $\hat{d} + \epsilon\Delta$. We have investigated the value of ϵ that minimizes the root-mean-square fluctuations of a representative selection of measurements. The result is $\epsilon = -0.17$, and the difference in the r.m.s. values is negligible (0.00037 vs. 0.00039) so we keep the center of the signal as our

standard ruler, *i.e.* $\epsilon = 0$. The r.m.s. fluctuation of the lower edge with $\epsilon = -1$ is 0.00068, and the fluctuation of the upper edge with $\epsilon = 1$ is 0.00091, which again illustrates the bias described in Appendix 7.2, *i.e.* the lower edge fluctuates less than the upper edge.

A separate open question is whether this center $\hat{d}$ coincides with the d_{drag} of Equation (5)?

Yet another question is this: what value of ϵ would reproduce the Planck Ω_m? We obtain ϵ ranging from −0.81 for $\hat{d}_\alpha$ at $z = 0.34$, to $\epsilon = -0.43$ for $\hat{d}_z$ at $z = 0.56$. These large values of $|\epsilon|$, and their strong dependence on z and galaxy-galaxy orientation, do not seem plausible.

Finally, how well do we understand d_{drag}/d_*? The present study takes $z_{\text{drag}} = 1059.94 \pm 0.30$ and $d_{\text{drag}}/d_* = 1.0184 \pm 0.0004$ from the Planck analysis [3]. Note the extremely small uncertainty obtained by the Planck Collaboration. In comparison, from Equation (4) of Reference [20] we obtain $z_{\text{drag}} = 1020.82$ and $d_{\text{drag}}/d_* = 1.044$.

An estimate of the uncertainties due to the issues discussed in this Appendix is included in **Table 5**.

International Journal of Astronomy and Astrophysics, 2018, 8, 406-424
http://www.scirp.org/journal/ijaa
ISSN Online: 2161-4725
ISSN Print: 2161-4717

Artificial Equilibrium Points in the Low-Thrust Restricted Three-Body Problem When Both the Primaries Are Oblate Spheroids

Amit Mittal[1], Krishan Pal[2]

[1]Department of Mathematics, A.R.S.D College, University of Delhi, New Delhi, India
[2]Department of Mathematics, Maharaja Agrasen College, University of Delhi, New Delhi, India
Email: to.amitmittal@gmail.com, kpal1987@gmail.com

How to cite this paper: Mittal, A. and Pal, K. (2018) Artificial Equilibrium Points in the Low-Thrust Restricted Three-Body Problem When Both the Primaries Are Oblate Spheroids. *International Journal of Astronomy and Astrophysics*, **8**, 406-424.
https://doi.org/10.4236/ijaa.2018.84028

Received: November 2, 2018
Accepted: December 26, 2018
Published: December 29, 2018

Abstract

This paper studies the existence and stability of the artificial equilibrium points (AEPs) in the low-thrust restricted three-body problem when both the primaries are oblate spheroids. The artificial equilibrium points (AEPs) are generated by canceling the gravitational and centrifugal forces with continuous low-thrust at a non-equilibrium point. Some graphical investigations are shown for the effects of the relative parameters which characterized the locations of the AEPs. Also, the numerical values of AEPs have been calculated. The positions of these AEPs will depend not only also on magnitude and directions of low-thrust acceleration. The linear stability of the AEPs has been investigated. We have determined the stability regions in the *xy*, *xz* and *yz*-planes and studied the effect of oblateness parameters $A_1\left(0<A_1<1\right)$ and $A_2\left(0<A_2<1\right)$ on the motion of the spacecraft. We have found that the stability regions reduce around both the primaries for the increasing values of oblateness of the primaries. Finally, we have plotted the zero velocity curves to determine the possible regions of motion of the spacecraft.

Keywords

Restricted Three-Body Problem, Artificial Equilibrium Points, Low-Thrust, Stability, Oblate Spheroid, Zero Velocity Curves

1. Introduction

Generally, the restricted three-body problem is one of the most important problem in the field of celestial mechanics. In the Restricted Three-Body Problem (R3BP), the mass of the third body (*i.e.*, the spacecraft) is assumed to be

negligible in comparison to the two more massive bodies, defined as the primary and the secondary. It is assumed that the two primaries revolving in circular orbits about their common center of mass, known as the barycenter. It is then possible to model the motion of the spacecraft in a frame of reference that rotates about the barycenter at the same rotation rate as the two primaries. The motion of the spacecraft is affected by the motion of the primaries but not affect them. To study the motion of the third body is known as restricted three-body problem. There are five equilibrium points in the classical restricted three-body problem (R3BP), three of them are on the straight line joining the primaries, called collinear equilibrium points, and two of them setup equilateral triangle with the primaries. The collinear equilibrium points $L_{1,2,3}$ are always unstable in the linear sense for any value of mass parameter μ whereas the triangular points $L_{4,5}$ are stable if $\mu < \mu_c = 0.03852\cdots$. Szebehely [1]. Many perturbing forces, like oblateness, radiation forces of the primaries, Coriolis and centrifugal forces etc., have been included in the study of the R3BP. Many results have been published to the study in the restricted three-body problem with effect of oblateness; see Subbarao and Sharma [2], Bhatnagar and Chawla [3], Tsirogiannis *et al.* [4], Mittal *et al.* [5], Singh [6], Beevi and Sharma [7], Abouelmagd [8], Jain and Aggarwal [9]. Zotos [10] has determined the basins of attraction associated with the equilibrium points in the planar CR3BP where one of the primary bodies is an oblate spheroid or an emitter of radiation. Also, he has noticed that the structure of the basins of convergence is more affected by the mass ratio and radiation pressure parameters than the oblateness parameter. Srivastava *et al.* [11] have introduced Kustaanheimo-Stiefel (KS)-transformation to reduce the order of singularities arising due to the motion of an infinitesimal body in the vicinity of smaller primary in the R3BP when the bigger primary is a source of radiation and smaller one as an oblate spheroid. They have found that KS-regularization reduces the order of the pole from five to three at the point of singularity of the governing equations of motion.

The new equilibrium points can be generated if the continuous constant acceleration uses by a spacecraft to balance the gravitational and centrifugal forces. These points are usually referred to Artificial Equilibrium Points (AEPs). Recently, low-thrust propulsion systems as solar-sail and the electric propulsion are being developed not only for controlling satellite orbit, but also as main engines for interplanetary transfer orbits. These low-thrust propulsion systems are able to provide continuous control acceleration to the spacecraft and thus, increase mission design flexibility. Farquhar [12] has studied the concept of telecommunication systems using equilibrium points and investigated ballistic periodic orbits about these points in the Earth-Moon system. Dusek [13], McInnes *et al.* [14], Broschart and Scheeres [15] have studied the stability of equilibrium points with continuous control acceleration. Morimoto *et al.* [16] have studied the existence and stability of the AEPs in the low-thrust R3BP and found the stable regions. They have used the discriminant of cubic equation and the Descartes sign rule to study the stability of these AEPs. Baig and McInnes [17]

have investigated the artificial three-body equilibria for hybrid low-thrust propulsion. In their study, they have introduced a new concept of creating AEPs in the R3BP when the third body uses a hybrid of solar-sail and electric propulsion. Further, there are many precise work related to the low-thrust restricted three-body problem; see Bombardelli and Pelaez [18], Aliasi *et al.* [19] [20], Ranjana and Kumar [21], Yang *et al.* [22], Lei and Xu [23]. Bu *et al.* [24] have investigated the positions and dynamical characteristic of AEPs in a binary asteroid system with continuous low-thrust. They have found the stable regions of AEPs by a parametric analysis and studied the effect of the mass ratio and ellipsoid parameters on the stable region. Further, they have analyzed the effect of the continuous low-thrust on the feasible region of motion by ZVCs.

In the present work, we have focussed on the study of the motion of the spacecraft in the low-thrust restricted three-body problem when both the primaries are oblate spheroids. Here, we have extended the work of Morimoto *et al.* [16]. We have arranged the present work as follows: In Secttion 2, we have derived the equations of motion of the spacecraft. In Secttion 3, we have found the locations of the AEPs. In Secttion 4, we have determined the linear stability. In Secttion 5, we have computed the zero velocity curves. Finally, in Secttion 6, we have concluded the results obtained.

2. Equations of Motion

In this section, we shall determine the equations of motion of the spacecraft in the low-thrust restricted three-body problem when both the primaries are oblate spheroids. Suppose two bodies of masses m_1 and m_2 $\left(m_1 > m_2\right)$ are the primaries moving with angular velocity ω in circular orbits about their center of mass O taken as origin, and let the infinitesimal body (spacecraft) of mass m_3 be also moving in the plane of motion of m_1 and m_2. The motion of the spacecraft is affected by the motion of m_1 and m_2 but not affect them. The line joining the primaries m_1 and m_2 is taken as X-axis and the line passes through the origin O and perpendicular to the X-axis and lying in the plane of motion of m_1 and m_2 is considered as Y-axis, the line which passes through the origin and perpendicular to the plane of motion of the primaries is taken as Z-axis. In a synodic frame, the system of synodic coordinates $O\left(xyz\right)$, initially coincident with the system of inertial coordinates $O\left(XYZ\right)$, rotating with the angular velocity ω about Z-axis; (the z axis is coincident with Z-axis). Let the primaries of masses m_1 and m_2 be located at $\left(-\mu,0,0\right)$ and $\left(1-\mu,0,0\right)$ respectively and the spacecraft be located at the point $\left(x,y,z\right)$ (see **Figure 1**). The angular velocity of the primaries is given by the relation $\omega=\sqrt{\frac{G\left(m_1+m_2\right)}{l^3}}$, where l is distance between the primaries, and G is Gravitational constant. We scale the units by taking the sum of the masses and the distance between the primaries both equal to unity. Therefore $m_1=1-\mu$, $m_2=\mu$ and $\mu=\frac{m_2}{m_1+m_2}$ with

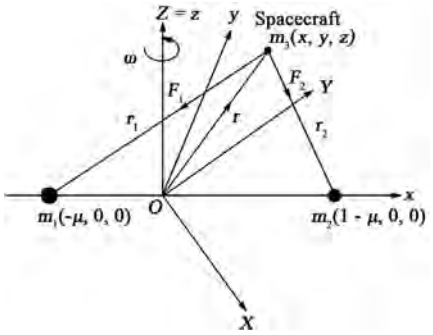

Figure 1. Configuration of the problem.

$m_1 + m_2 = 1$. Also, the scale of the time is chosen so that the gravitational constant is unity. Let a_1, b_1, c_1 and a_2, b_2, c_2 are the semi axes of rigid bodies of masses m_1 and m_2 respectively. The equation of motion of the spacecraft in vector form is expressed as

$$\frac{\mathrm{d}^2\boldsymbol{r}}{\mathrm{d}t^2} + 2\boldsymbol{w} \times \frac{\mathrm{d}\boldsymbol{r}}{\mathrm{d}t} = \boldsymbol{a} - \nabla\Omega = \boldsymbol{F}, \tag{1}$$

where Ω is the potential (McCuskey [25]) of the system that combines the gravitational potential and the potential from the centripetal acceleration which is defined as

$$\Omega = -\frac{n^2}{2}\left(x^2 + y^2\right) - \frac{1-\mu}{r_1} - \frac{\mu}{r_2} - \frac{(1-\mu)A_1}{2r_1^3} - \frac{\mu A_2}{2r_2^3},$$

and

$\boldsymbol{F}$ = total force acting on m_3 = $\boldsymbol{F}_1 + \boldsymbol{F}_2$,

$\boldsymbol{F}_1$ = Gravitational force exerted on m_3 due to m_1 along m_3m_1,

$\boldsymbol{F}_2$ = Gravitational force exerted on m_3 due to m_2 along m_3m_2.

The vector $\boldsymbol{a} = \left(a_x, a_y, a_z\right)$ is low-thrust acceleration and $\boldsymbol{r} = \left(x, y, z\right)^{\mathrm{T}}$ is the position vector of the spacecraft from the origin. Thus, the equations of motion of the spacecraft with continuous low-thrust in dimensionless co-ordinate system can be written as Morimoto *et al.* [16]

$$\left.\begin{aligned} \ddot{x} - 2n\dot{y} &= -\Omega_x + a_x = -\Omega_x^*, \\ \ddot{y} + 2n\dot{x} &= -\Omega_y + a_y = -\Omega_y^*, \\ \ddot{z} &= -\Omega_z + a_z = -\Omega_z^*, \end{aligned}\right\} \tag{2}$$

where Ω^* is the effective potential of the system with continuous low-thrust can be written as

$$\begin{aligned} \Omega^* &= \Omega - a_x x - a_y y - a_z z \\ &= -\frac{n^2}{2}\left(x^2 + y^2\right) - \frac{1-\mu}{r_1} - \frac{\mu}{r_2} - \frac{(1-\mu)A_1}{2r_1^3} - \frac{\mu A_2}{2r_2^3} - a_x x - a_y y - a_z z, \end{aligned}$$

where

$$r_1 = \sqrt{\left(x+\mu\right)^2 + y^2 + z^2},$$

$$r_2 = \sqrt{\left(x+\mu-1\right)^2 + y^2 + z^2},$$

$$a = \sqrt{a_x^2 + a_y^2 + a_z^2}.$$

The required mean motion of the primaries denoted by n, which is given by the relation:

$$n^2 = 1 + \frac{3}{2}(A_1 + A_2),$$

where A_1 is the oblateness parameter of m_1 which is defined as $A_1 = \frac{a_1^2 - c_1^2}{5l^2}, 0 < A_1 < 1, a_1 = b_1 (a_1 > c_1)$, and A_2 is the oblateness parameter of m_2 which is also defined as $A_2 = \frac{a_2^2 - c_2^2}{5l^2}, 0 < A_2 < 1, a_2 = b_2 (a_2 > c_2)$, where l be the distance between the primaries.

3. Locations of the Artificial Equilibrium Points

In order to find the AEPs of the system, taking velocity and acceleration of the system equal to zero. For obtaining the artificial equilibrium points (AEPs) of the system, we have adopted the similar procedures of McInnes *et al.* [14], Morimoto *et al.* [16], Baig and McInnes [17], and Bu *et al.* [24] in the low-thrust R3BP when both the primaries are oblate spheroid. The AEPs denoted by (x_0, y_0, z_0) are the solution of the equations given by:

$$\left.\begin{aligned} &-n^2 x_0 + \frac{1-\mu}{r_1^3}(x_0 + \mu)\left(1 + \frac{3A_1}{2r_1^2}\right) + \frac{\mu}{r_2^3}(x_0 + \mu - 1)\left(1 + \frac{3A_2}{2r_2^2}\right) - a_x = 0, \\ &-n^2 y_0 + \frac{1-\mu}{r_1^3} y_0 \left(1 + \frac{3A_1}{2r_1^2}\right) + \frac{\mu}{r_2^3} y_0 \left(1 + \frac{3A_2}{2r_2^2}\right) - a_y = 0, \\ &\frac{1-\mu}{r_1^3} z_0 \left(1 + \frac{3A_1}{2r_1^2}\right) + \frac{\mu}{r_2^3} z_0 \left(1 + \frac{3A_2}{2r_2^2}\right) - a_z = 0. \end{aligned}\right\} \quad (3)$$

The control acceleration components (a_x, a_y, a_z) of an AEP (x_0, y_0, z_0) are

$$a_x = -n^2 x_0 + \frac{1-\mu}{r_1^3}(x_0 + \mu)\left(1 + \frac{3A_1}{2r_1^2}\right) + \frac{\mu}{r_2^3}(x_0 + \mu - 1)\left(1 + \frac{3A_1}{2r_2^2}\right),$$

$$a_y = -n^2 y_0 + \frac{1-\mu}{r_1^3} y_0 \left(1 + \frac{3A_1}{2r_1^2}\right) + \frac{\mu}{r_2^3} y_0 \left(1 + \frac{3A_2}{2r_2^2}\right),$$

$$a_z = \frac{1-\mu}{r_1^3} z_0 \left(1 + \frac{3A_1}{2r_1^2}\right) + \frac{\mu}{r_2^3} z_0 \left(1 + \frac{3A_2}{2r_2^2}\right).$$

When $A_1 = 0, A_2 = 0, \boldsymbol{a} = (0,0,0)$, the above Equations (3) reduce to the classical equations obtained by Szebhely [1]. When $A_1 = A_2 = 0$ and $\boldsymbol{a} \neq (0,0,0)$, the above Equations (3) reduce to the equations obtained by Morimoto *et al.* [16]. Solving Equations (3) for $z = 0$, then the AEPs are lie in the *xy*-plane and obtained by solving $\Omega_x^* = 0, \Omega_y^* = 0$. We have obtained the five AEPs for given thrust and oblateness parameters denoted by L_1, L_2, L_3, L_4 and L_5 as shown in **Figure 2**.

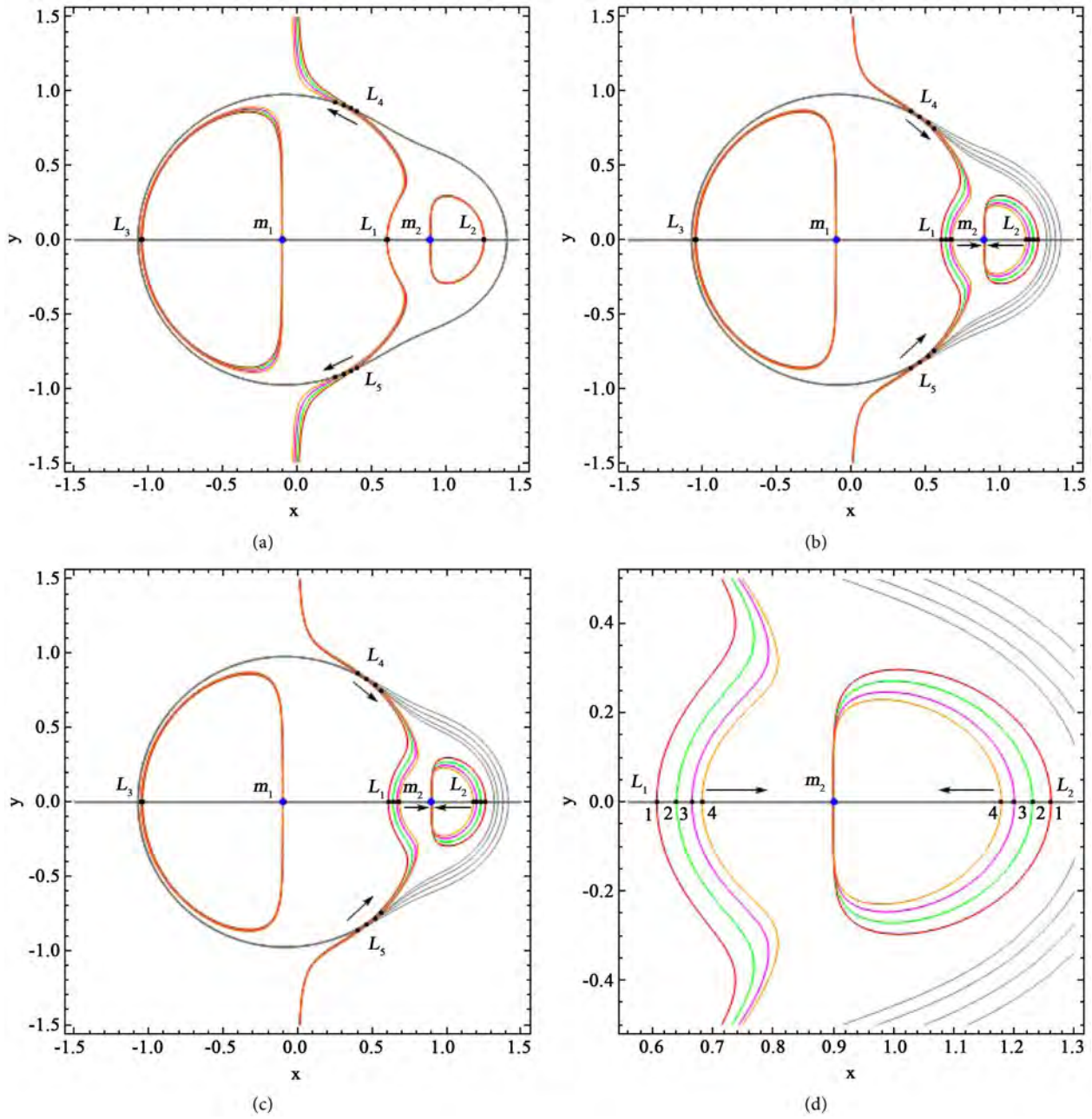

Figure 2. The locations of the five AEPs in the low-thrust R3BP with the effect of constant control acceleration and oblateness parameters. Panel-(a) for $\mu = 0.1$, $A_1 = 0.0015$, $A_2 = 0.0015$ and for different values of $\boldsymbol{a} = (0.0001, 0, 0)$(gray, red), $(0.01, 0, 0)$(gray, green), $(0.02, 0, 0)$(gray, magenta), $(0.03, 0, 0)$(gray, orange), and panel-(b) for $\mu = 0.1$, $A_1 = 0.0015$, $\boldsymbol{a} = (0.0001, 0, 0)$ and for different values of $A_2 = 0.0015$(gray, red), 0.15(gray, green), 0.35(gray, magenta), 0.55(gray, orange), panel-(c) for $\mu = 0.1$, $A_2 = 0.0015$, $\boldsymbol{a} = (0.0001, 0, 0)$ and for different values of $A_1 = 0.0015$(gray, red), 0.15(gray, green), 0.35(gray, magenta), 0.55(gray, orange), panel-(d) shows the zoomed part of panel-(c) near the primary m_2.

From Figure 2(a), we have observed that when $\boldsymbol{a} = (a_x, 0, 0)$ is increasing, the movement of AEPs L_1, L_2 and L_3 is almost negligible and the AEPs L_4 and L_5 move towards the y-axis. From Figure 2(b), we have observed that when A_2 is increasing, the AEP L_1 is shifted from right to left towards the bigger primary m_1,

the AEP L_2 is shifted from left to right away from the primary m_2, the AEP L_3 is shifted from left to right towards the bigger primary m_1, and the AEPs L_4 and L_5 move towards the x-axis.

From Figure 2, panel-c, we have observed that when A_1 is increasing, the AEP L_1 is shifted from left to right towards the primary m_2, the AEP L_2 is shifted from right to left towards the primary m_2, the AEP L_3 has almost negligible movement, and the AEPs L_4 and L_5 move towards the x-axis. In addition, we have calculated the numerical values of the AEPs and shown in Tables 1-3. We have observed that there exist three collinear and two non-collinear AEPs. Further, we have observed that the AEPs L_4 and L_5 are symmetric about the x-axis. Also, it is observed that the AEPs are the new positions of equilibrium points with the effect of continuous low-thrust and oblateness parameters which are different from the natural equilibrium points.

Table 1. The AEPs in the xy-plane when $\boldsymbol{a}$ is varying.

$\mu = 0.1, A_1 = 0.0015, A_2 = 0.0015$				
$\boldsymbol{a}$	L_1	L_2	L_3	$L_{4,5}$
$\boldsymbol{a} = (0.0001, 0, 0)$	(0.607238, 0)	(1.26105, 0)	(−1.04099, 0)	(0.399632, ±0.865334)
$\boldsymbol{a} = (0.01, 0, 0)$	(0.606555, 0)	(1.25943, 0)	(−1.04409, 0)	(0.360261, ±0.882827)
$\boldsymbol{a} = (0.02, 0, 0)$	(0.605864, 0)	(1.25783, 0)	(−1.04724, 0)	(0.313254, ±0.901830)
$\boldsymbol{a} = (0.03, 0, 0)$	(0.605170, 0)	(1.25623, 0)	(−1.05042, 0)	(0.256260, ±0.922021)

Table 2. The AEPs in the xy-plane when A_2 is varying.

$\mu = 0.1, A_1 = 0.0015, \boldsymbol{a} = (0.0001, 0, 0)$				
A_2	L_1	L_2	L_3	$L_{4,5}$
$A_2 = 0.0015$	(0.607238, 0)	(1.26105, 0)	(−1.040990, 0)	(0.399632, ±0.865334)
$A_2 = 0.15$	(0.517691, 0)	(1.33070, 0)	(−0.978206, 0)	(0.337489, ±0.826131)
$A_2 = 0.35$	(0.469823, 0)	(1.35936, 0)	(−0.914454, 0)	(0.278167, ±0.782639)
$A_2 = 0.55$	(0.439717, 0)	(1.37309, 0)	(−0.865643, 0)	(0.235596, ±0.746951)

Table 3. The AEPs in the xy-plane when A_1 is varying.

$\mu = 0.1, A_2 = 0.0015, \boldsymbol{a} = (0.0001, 0, 0)$				
A_1	L_1	L_2	L_3	$L_{4,5}$
$A_1 = 0.0015$	(0.607238, 0)	(1.26105, 0)	(−1.04099, 0)	(0.399632, ±0.865334)
$A_1 = 0.15$	(0.640227, 0)	(1.23015, 0)	(−1.04628, 0)	(0.462511, ±0.826131)
$A_1 = 0.35$	(0.665587, 0)	(1.20039, 0)	(−1.05001, 0)	(0.521833, ±0.782639)
$A_1 = 0.55$	(0.682196, 0)	(1.17863, 0)	(−1.05213, 0)	(0.564404, ±0.746951)

4. Stability of the Artificial Equilibrium Points

To determine the linear stability of the system of AEPs in the low-thrust R3BP when both the primaries are oblate spheroid. We have followed the linear stability procedure of Morimoto *et al.* [16]. Firstly, we have linearized the equations of motion of the spacecraft and then linear stability is studied. To establish the spacecraft at a non-equilibrium point, a continuous low-thrust is provided to the spacecraft. Now, giving the small displacement to (x_0, y_0, z_0) as $x = x_0 + \delta_x, y = y_0 + \delta_y, z = z_0 + \delta_z, (\delta_x, \delta_y, \delta_z \ll 1)$. After using above displacements, the linearized equations corresponding to Equations (2) are given by

$$\left.\begin{aligned} \ddot{\delta}_x - 2n\dot{\delta}_y &= \Omega^0_{xx}\delta_x + \Omega^0_{xy}\delta_y + \Omega^0_{xz}\delta_z, \\ \ddot{\delta}_y + 2n\dot{\delta}_x &= \Omega^0_{yx}\delta_x + \Omega^0_{yy}\delta_y + \Omega^0_{yz}\delta_z, \\ \ddot{\delta}_z &= \Omega^0_{zx}\delta_x + \Omega^0_{zy}\delta_y + \Omega^0_{zz}\delta_z, \end{aligned}\right\} \tag{4}$$

where the superscript "0" in Equations (4) indicates that the values are to be calculated at the AEP (x_0, y_0, z_0) under consideration. The characteristic root λ satisfies the given characteristic equation

$$\begin{aligned} f(\lambda) = \lambda^6 &+ \left(\Omega^0_{xx} + \Omega^0_{yy} + \Omega^0_{zz} + 4n^2\right)\lambda^4 + \left(\Omega^0_{xx}\Omega^0_{yy} + \Omega^0_{xx}\Omega^0_{zz} + \Omega^0_{yy}\Omega^0_{zz}\right. \\ &\left. - \left(\Omega^0_{xy}\right)^2 - \left(\Omega^0_{xz}\right)^2 - \left(\Omega^0_{yz}\right)^2 + 4n^2\Omega^0_{zz}\right)\lambda^2 + \Omega^0_{xx}\Omega^0_{yy}\Omega^0_{zz} \\ &+ 2\Omega^0_{xy}\Omega^0_{xz}\Omega^0_{yz} - \left(\Omega^0_{xy}\right)^2\Omega^0_{zz} - \left(\Omega^0_{xz}\right)^2\Omega^0_{yy} - \left(\Omega^0_{yz}\right)^2\Omega^0_{xx} \\ &= 0. \end{aligned} \tag{5}$$

If a characteristic root λ satisfies the Equation (5), then Equation (5) can be rewritten as

$$\begin{aligned} &\lambda^6 + \left(\Omega^0_{xx} + \Omega^0_{yy} + \Omega^0_{zz} + 4n^2\right)\lambda^4 + \left(\Omega^0_{xx}\Omega^0_{yy} + \Omega^0_{xx}\Omega^0_{zz} + \Omega^0_{yy}\Omega^0_{zz}\right. \\ &\left. - \left(\Omega^0_{xy}\right)^2 - \left(\Omega^0_{xz}\right)^2 - \left(\Omega^0_{yz}\right)^2 + 4n^2\Omega^0_{zz}\right)\lambda^2 + \Omega^0_{xx}\Omega^0_{yy}\Omega^0_{zz} \\ &+ 2\Omega^0_{xy}\Omega^0_{xz}\Omega^0_{yz} - \left(\Omega^0_{xy}\right)^2\Omega^0_{zz} - \left(\Omega^0_{xz}\right)^2\Omega^0_{yy} - \left(\Omega^0_{yz}\right)^2\Omega^0_{xx} = 0. \end{aligned} \tag{6}$$

We see that all the powers of λ in Equation (6) are even numbers and Equation (6) be a six degree equation in λ. If $k = \lambda^2$, then we get

$$\begin{aligned} &k^3 + \left(\Omega^0_{xx} + \Omega^0_{yy} + \Omega^0_{zz} + 4n^2\right)k^2 + \left(\Omega^0_{xx}\Omega^0_{yy} + \Omega^0_{xx}\Omega^0_{zz} + \Omega^0_{yy}\Omega^0_{zz}\right. \\ &\left. - \left(\Omega^0_{xy}\right)^2 - \left(\Omega^0_{xz}\right)^2 - \left(\Omega^0_{yz}\right)^2 + 4n^2\Omega^0_{zz}\right)k + \Omega^0_{xx}\Omega^0_{yy}\Omega^0_{zz} \\ &+ 2\Omega^0_{xy}\Omega^0_{xz}\Omega^0_{yz} - \left(\Omega^0_{xy}\right)^2\Omega^0_{zz} - \left(\Omega^0_{xz}\right)^2\Omega^0_{yy} - \left(\Omega^0_{yz}\right)^2\Omega^0_{xx} = 0. \end{aligned} \tag{7}$$

Equation (7) is a cubic equation in k and can be rewritten as

$$k^3 + d_1k^2 + d_2k + d_3 = 0, \tag{8}$$

where

$$d_1 = \Omega^0_{xx} + \Omega^0_{yy} + \Omega^0_{zz} + 4n^2,$$

$$d_2 = \Omega^0_{xx}\Omega^0_{yy} + \Omega^0_{xx}\Omega^0_{zz} + \Omega^0_{yy}\Omega^0_{zz} - \left(\Omega^0_{xy}\right)^2 - \left(\Omega^0_{xz}\right)^2 - \left(\Omega^0_{yz}\right)^2 + 4n^2\Omega^0_{zz},$$

$$d_3 = \Omega_{xx}^0 \Omega_{yy}^0 \Omega_{zz}^0 + 2\Omega_{xy}^0 \Omega_{xz}^0 \Omega_{yz}^0 - \left(\Omega_{xy}^0\right)^2 \Omega_{zz}^0 - \left(\Omega_{xz}^0\right)^2 \Omega_{yy}^0 - \left(\Omega_{yz}^0\right)^2 \Omega_{xx}^0,$$

and d_1, d_2, and d_3 are the real coefficients of k that depend on the second ordered derivatives of Ω with respect to x and y. Now, we determine the linear stability of the AEPs by finding the characteristic roots of Equation (8). We know that all the characteristic roots of a cubic equation are either real numbers or one of them is a real number and other characteristic roots are imaginary numbers. According to stability theory, a necessary and sufficient condition for an AEP to be linearly stable is that all the characteristic roots of Equation (5) lie in the left-hand side of the λ-plane (*i.e.*, $\lambda \le 0$). If one or more characteristic roots of Equation (5) lie in the right-hand side of the λ-plane, then the system of AEPs is always unstable. If all the characteristic roots of Equation (5) lie to the left-hand side of λ-plane, then Equation (8) must have three real and negative roots. The resulting linear stability conditions according to Morimoto *et al.* [16] and Descartes sign rule, the system of AEPs is linearly stable if and only if $D \ge 0, d_1 > 0, d_2 > 0$ and $d_3 > 0$, where D is the discriminant of the cubic Equation (8) and is given by:

$$D = \frac{1}{4}\left(d_3 + \frac{2d_1^3 - 9d_1 d_2}{27}\right)^2 + \frac{1}{27}\left(d_2 - \frac{d_1^2}{3}\right)^3. \tag{9}$$

It is concluded that the system of AEPs is linearly stable when $D \ge 0, d_1 > 0, d_2 > 0$ and $d_3 > 0$. Now, we have found the stability regions in the *xy*, *xz* and *yz*-planes as shown in **Figures 3-8**. In **Figure 3**, **Figure 5**, **Figure 7**, we have drawn the stability regions for the fixed values of $\mu = 0.1$, $A_1 = 0.0015$ and for different values of oblateness parameter $A_2 = 0.0015, 0.15, 0.35, 0.55, 0.75, 0.95$. In **Figure 4**, we have plotted the stability regions for the fixed values of $\mu = 0.1$, $A_2 = 0.0015$ and for different values of oblateness parameter $A_1 = 0.0015, 0.015, 0.035, 0.055, 0.075, 0.095$. In **Figure 6** and **Figure 8**, we have plotted the stability regions for the fixed values of $\mu = 0.1$, $A_2 = 0.0015$ and for different values of oblateness parameter $A_1 = 0.0015, 0.15, 0.35, 0.55, 0.75, 0.95$. From, **Figures 3-8**, we have observed that the stability regions decrease around both primaries for the increasing values of oblateness parameters $A_1, A_2 \in (0,1)$ and for fixed value of mass parameter $\mu = 0.1$. Also, it is observed that the AEPs located in the stable regions are linearly stable otherwise unstable.

5. Zero Velocity Curves

In this section, we shall determine the possible regions of motion of the spacecraft in the low-thrust restricted thee-body problem when both the primaries are oblateness spheroid. The Jacobian Integral of the equations of motion (2) is defined as

$$C = 2\Omega + \left(\dot{x}^2 + \dot{y}^2 + \dot{z}^2\right). \tag{10}$$

The Jacobian Integral of the equations of motion (2) with continuous low-thrust is defined as

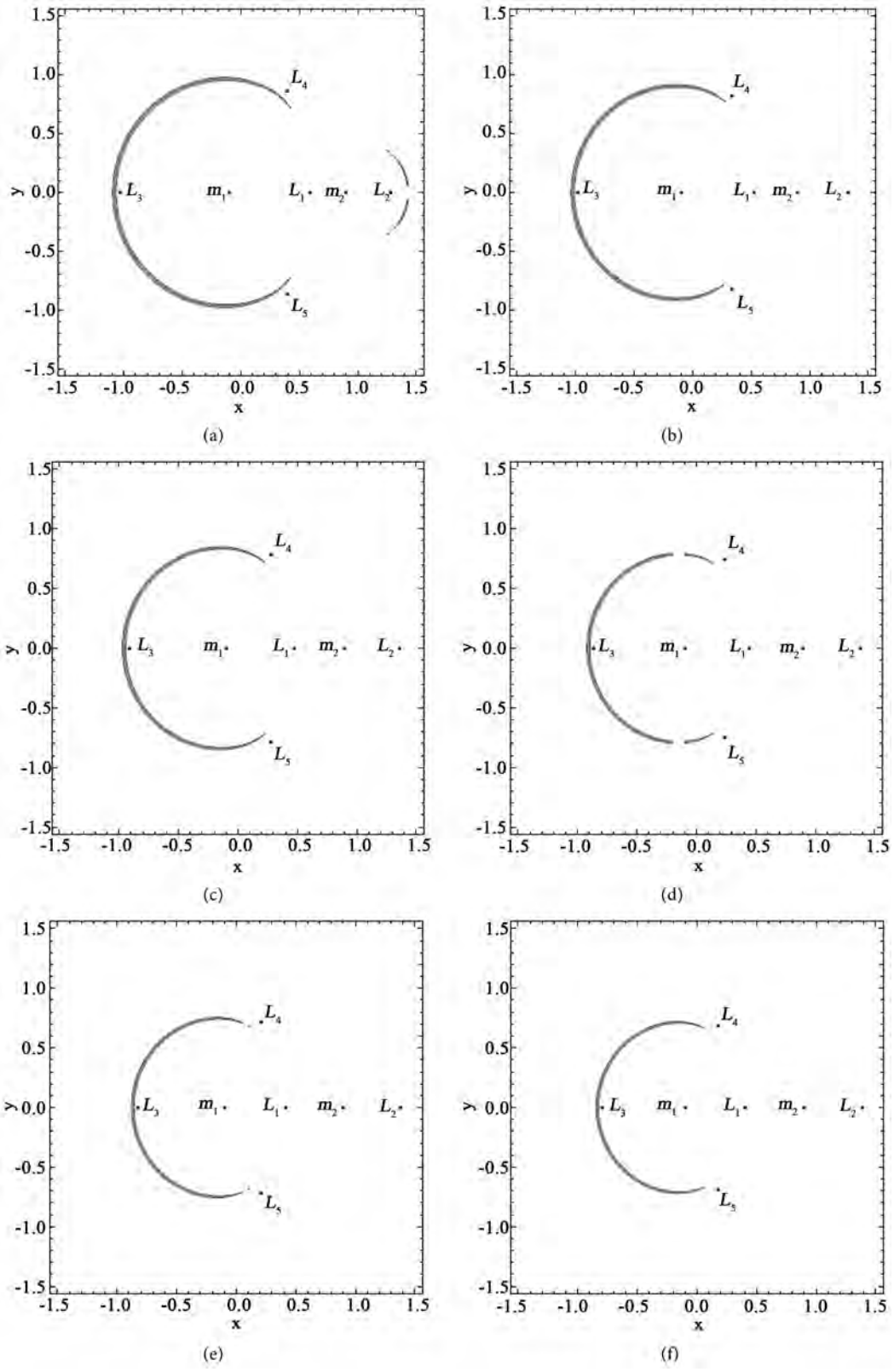

Figure 3. Stable regions (gray area) in the *xy*-plane for fixed values of $\mu = 0.1$, $A_1 = 0.0015$ and for different values of oblateness parameter $A_2 (0 < A_2 < 1)$ (a) for $A_2 = 0.0015$; (b) $A_2 = 0.15$; (c) $A_2 = 0.35$; (d) $A_2 = 0.55$; (e) $A_2 = 0.75$; (f) $A_2 = 0.95$.

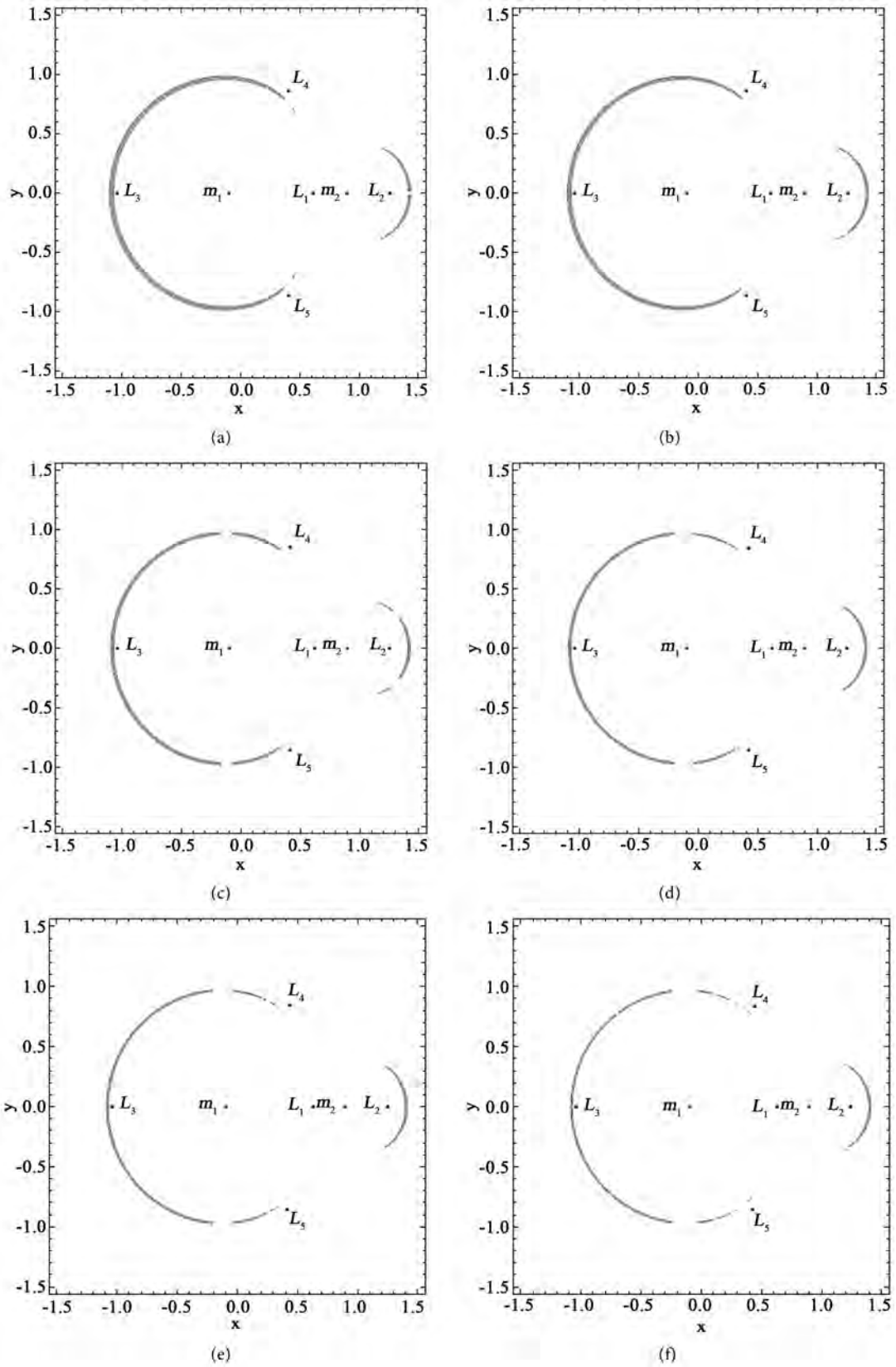

Figure 4. Stable regions(gray area) in the *xy*-plane for $\mu = 0.1$, $A_2 = 0.0015$ and for different values of oblateness parameter $A_1 (0 < A_1 < 1)$ (a) for $A_1 = 0.0015$; (b) $A_1 = 0.015$; (c) $A_1 = 0.035$; (d) $A_1 = 0.055$; (e) $A_1 = 0.075$; (f) $A_1 = 0.095$.

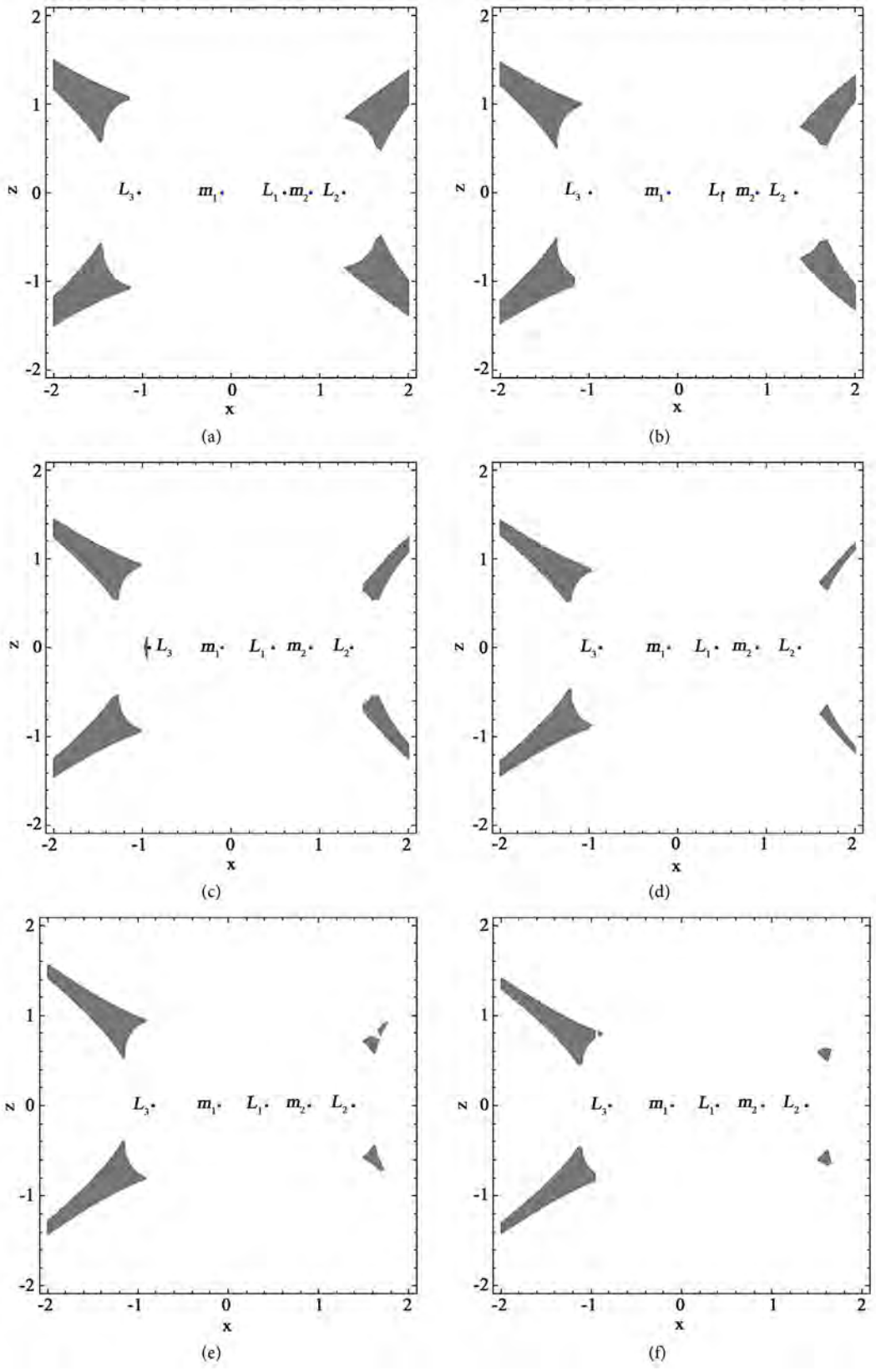

Figure 5. Stable regions (gray area) in the *xz*-plane for $\mu = 0.1$, $A_1 = 0.0015$ and for different values of oblateness parameter $A_2 (0 < A_2 < 1)$ (a) for $A_2 = 0.0015$; (b) $A_2 = 0.15$; (c) $A_2 = 0.35$; (d) $A_2 = 0.55$; (e) $A_2 = 0.75$; (f) $A_2 = 0.95$.

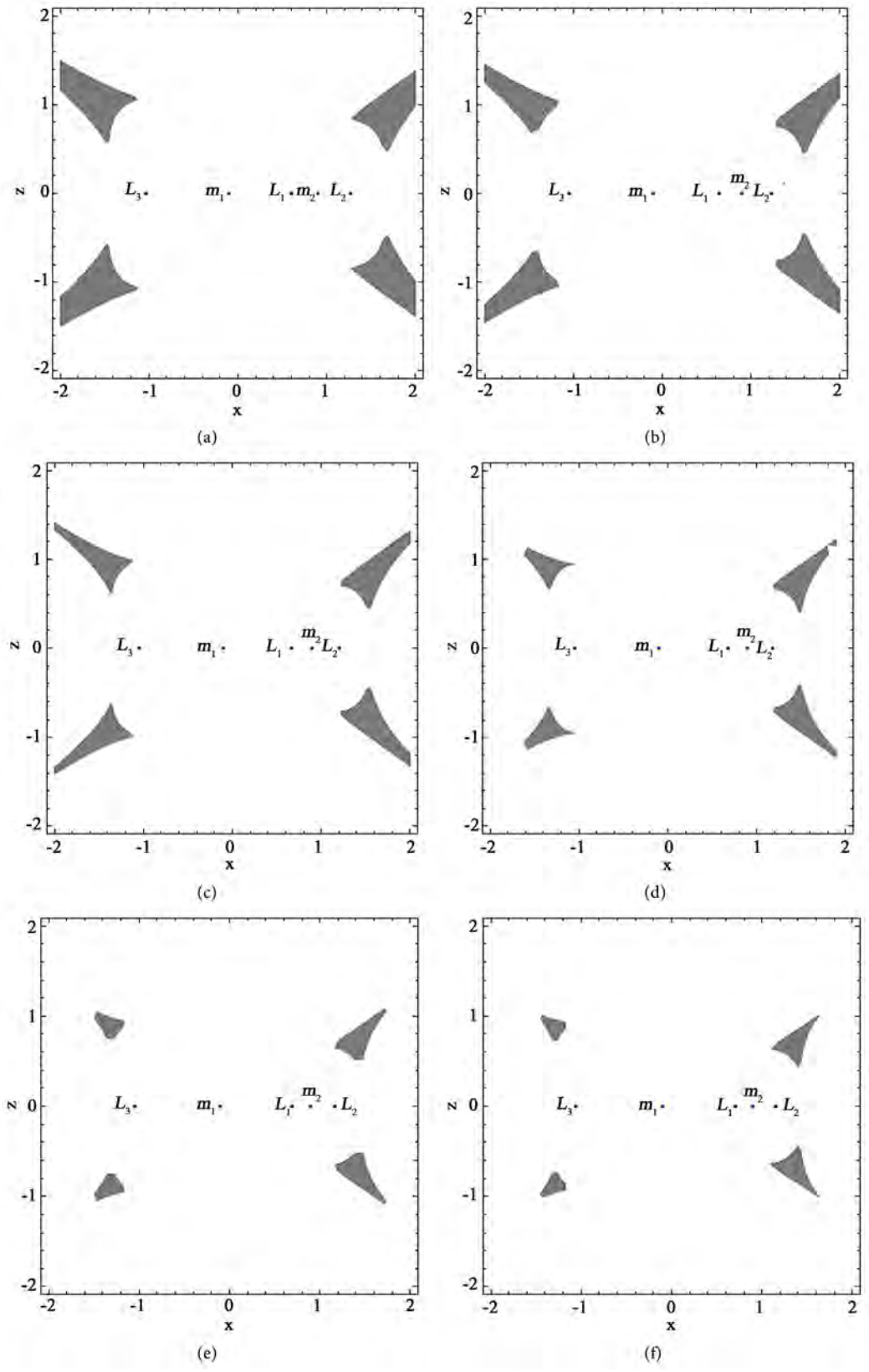

Figure 6. Stable regions (gray area) in the *xz*-plane for $\mu = 0.1$, $A_2 = 0.0015$ and for different values of oblateness parameter $A_1 (0 < A_1 < 1)$ (a) for $A_1 = 0.0015$; (b) $A_1 = 0.15$; (c) $A_1 = 0.35$; (d) $A_1 = 0.55$; (e) $A_1 = 0.75$; (f) $A_1 = 0.95$.

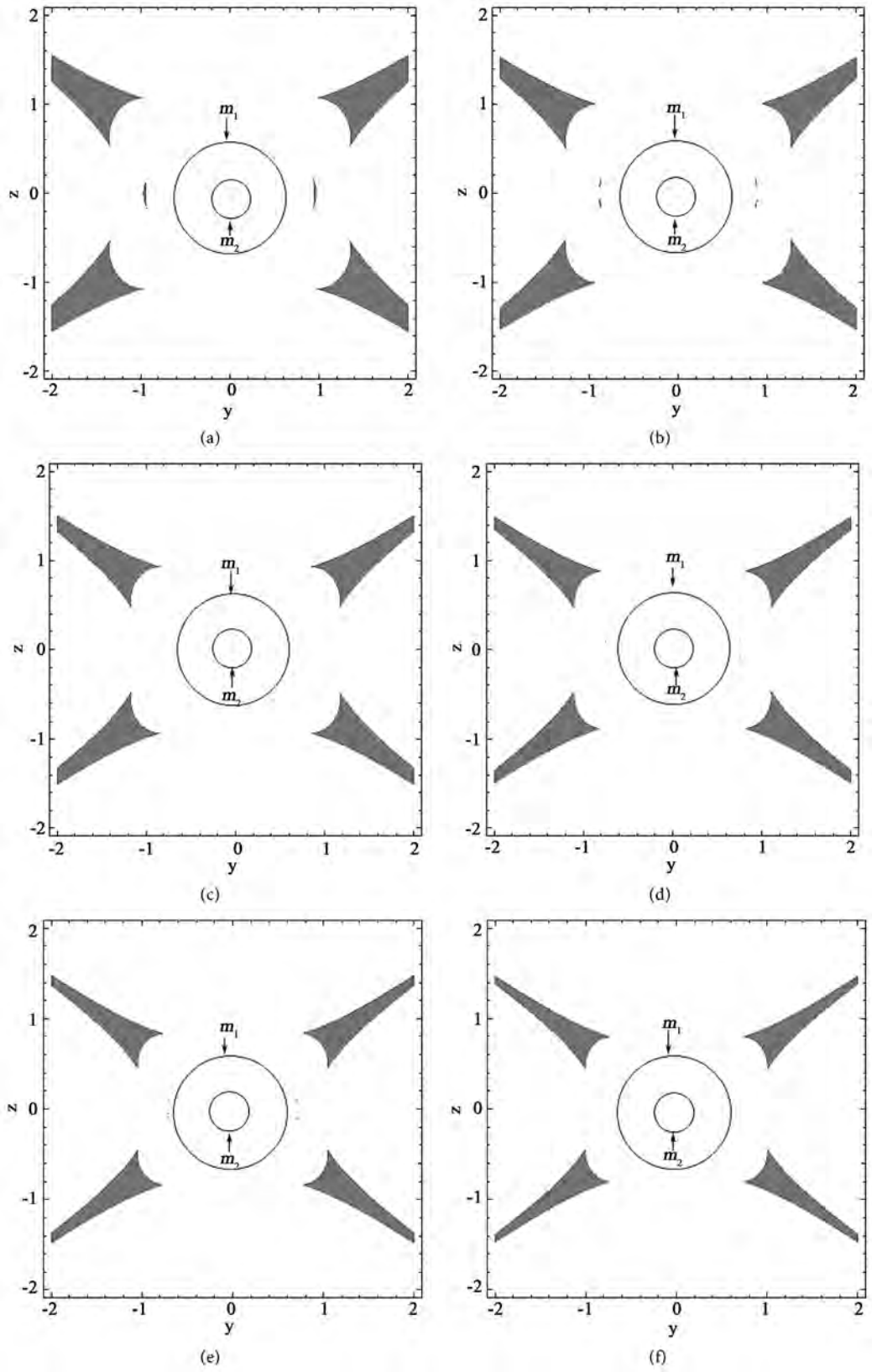

Figure 7. Stable regions (gray area) in the *yz*-plane for $\mu = 0.1$, $A_1 = 0.0015$ and for different values of oblateness parameter $A_2 (0 < A_2 < 1)$ (a) for $A_2 = 0.0015$; (b) $A_2 = 0.15$; (c) $A_2 = 0.35$; (d) $A_2 = 0.55$; (e) $A_2 = 0.75$; (f) $A_2 = 0.95$.

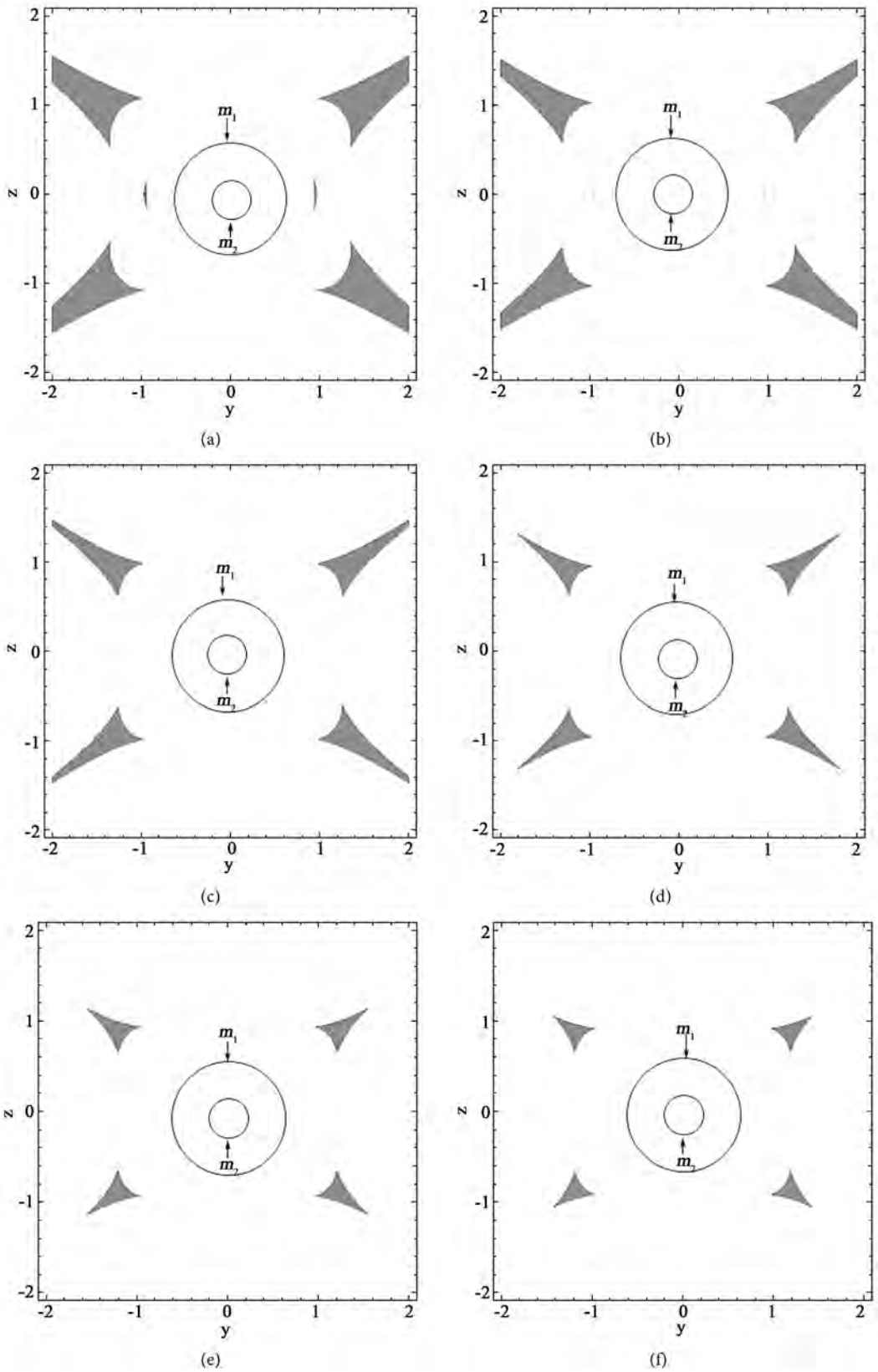

Figure 8. Stable regions (gray area) in the *yz*-plane for $\mu = 0.1$, $A_2 = 0.0015$ and for different values of oblateness parameter $A_1 (0 < A_1 < 1)$ (a) for $A_1 = 0.0015$; (b) $A_1 = 0.15$; (c) $A_1 = 0.35$; (d) $A_1 = 0.55$; (e) $A_1 = 0.75$; (f) $A_1 = 0.95$.

$$C' = 2\Omega^* + \left(\dot{x}^2 + \dot{y}^2 + \dot{z}^2\right). \tag{11}$$

The zero velocity curves have been determined from Equation (11) by taking $\dot{x} = \dot{y} = \dot{z} = 0$. The black dots show the positions of the five AEPs, while the blue dots indicate the positions of two primaries m_1 and m_2. In Figures 9(a)-(d), we have plotted the ZVCs for fixed values of mass $\mu = 0.1$ at the energy value of

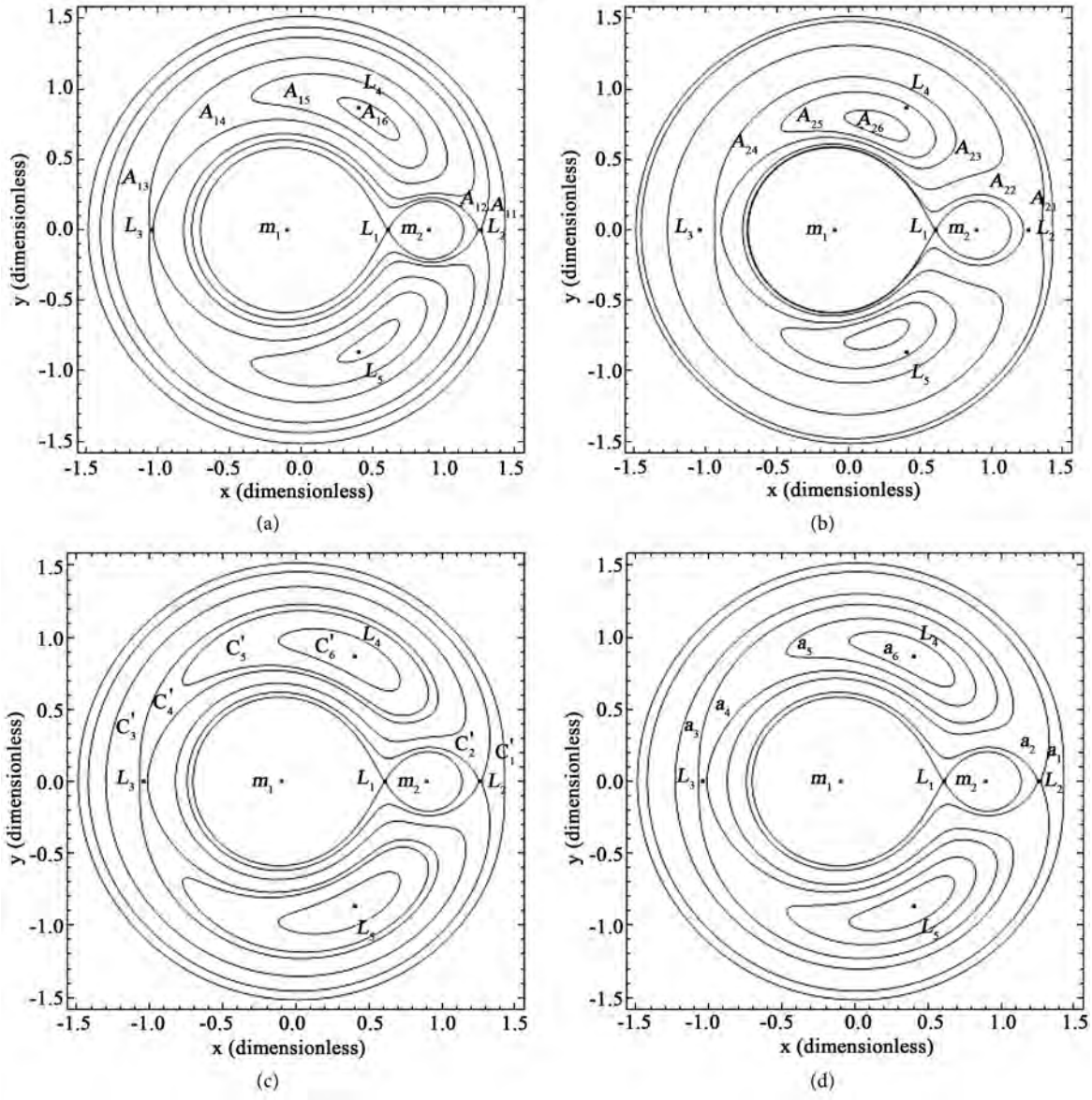

Figure 9. The ZVCs in the low-thrust restricted three-body problem when both the primaries are oblate spheroid for fixed value of mass parameter $\mu = 0.1$ (a) for fixed values of $C' = -3.608652$, $A_2 = 0.0015$, $\boldsymbol{a} = (0.0001, 0, 0)$ and for different values of $A_1 = 0.0015, 0.049, 0.095, 0.187, 0.25, 0.3$ at the energy values of L_1; (b) for fixed values of $C' = -3.608652$, $A_1 = 0.0015$, $\boldsymbol{a} = (0.0001, 0, 0)$ and for different values of $A_2 = 0.0015, 0.025, 0.15, 0.35, 0.45, 0.55$; Panel-(c) for fixed values of $A_1 = 0.0015$, $A_2 = 0.0015$, $\boldsymbol{a} = (0.0001, 0, 0)$ and for different values of Jacobian constant $C' = -3.608652, -3.478652, -3.288652, -3.108652, -3.058652, -2.958652$, and (d) for fixed values of $C' = -3.608652$, $A_1 = 0.0015$, $A_2 = 0.0015$, and for different values of low-thrust acceleration $\boldsymbol{a} = (0.0001, 0, 0)$, $(0.065, 0, 0)$, $(0.2, 0, 0)$, $(0.25, 0, 0)$, $(0.3, 0, 0)$, $(0.33, 0, 0)$.

L_1. The bounded curves in the panels-(a, b, c, d) indicate the forbidden regions. The forbidden regions are those regions where the motion of the spacecraft is not possible. The motion of the spacecraft is possible outside the bounded curves. We have observed that the spacecraft is free to move only in the regions outside the bounded curves. From **Figure 9(a)**, we have observed that when A_1 is increasing the regions of motion increase in which the spacecraft can freely move. From **Figure 9(b)**, it is observed that the regions of motion increase for the increasing values of oblateness parameter A_2 in which the spacecraft can move. On the other hand, from **Figure 9(c)**, we have observed that when Jacobian constant C' is increasing the regions of motion increase in which the spacecraft can freely move. Further, from **Figure 9(d)**, we have observed that when $\boldsymbol{a}$ is increasing, the possible regions of motion increase in which the spacecraft can freely move. Furthermore, from **Figures 9(a)-(d)**, we observe that the spacecraft can freely move from one primary to other for the increasing values of A_1, A_2, C' and $\boldsymbol{a}$ respectively. Thus, the nature of the ZVCs in the low-thrust R3BP depend on the Jacobian constant C', oblateness parameters A_1, A_2 and continuous control acceleration $\boldsymbol{a}$ of the low-thrust propulsion system of the spacecraft.

6. Conclusions

In this paper, we have studied the combined effect of oblateness of the primaries on the motion of the spacecraft in the low-thrust R3BP. The AEPs are obtained by introducing the continuous control acceleration at the non-equilibrium points. The numerical values of few AEPs have been calculated and displayed in **Tables 1-3**. It has been observed that there exist three collinear and two non-collinear AEPs for given parameters. We have observed that the non-collinear AEPs L_4 and L_5 are symmetric with respect to *x*-axis. The movements of AEPs have been studied graphically and shown in **Figure 2**. We find that the oblatness parameter of the bigger primary has less impact on the position of L_3 than oblateness of the smaller primary. Also, we have observed that the oblateness parameter of the primaries has more impact on the locations of the AEPs.

Further, we have plotted the stability regions in the *xy*, *xz* and *yz*-planes as shown in **Figures 3-8**. From, these figures, we have observed that the stability regions reduce around both the primaries m_1 and m_2 for the increasing values of oblateness parameters $A_1, A_2 \in (0,1)$ and for fixed value of mass parameter $\mu = 0.1$. Also, we find that the oblateness of the primaries has more impact on the stable regions. Our results are different from Morimoto *et al.* [16] in some aspects like, 1) they have generated the AEPs in the low-thrust R3BP, whereas we have generated the AEPs in the low-thrust R3BP with the effect of oblateness of the primaries. In our case, the AEPs are new positions of natural equilibrium points different from McInnes *et al.* [14], Morimoto *et al.* [16], Baig and McInnes [17], and Bu *et al.* [24] due to the presence of oblateness parameters $A_1\,(0 < A_1 < 1)$ and $A_2\,(0 < A_2 < 1)$. When both the oblateness parameters A_1

and A_2 are zero and $\boldsymbol{a} \neq (0,0,0)$, the results obtained in this work are similar with the work of McInnes *et al.* [14], Morimoto *et al.* [16], Baig and McInnes [17], and Bu *et al.* [24]. When $A_1 = 0$, $A_2 = 0$ and $\boldsymbol{a} = (0,0,0)$, the obtained results are similar with the work of Szebehely [1]. 2) they have obtained the stable regions in the Sun-Earth system, whereas we have obtained the stable regions for $\mu = 0.1$ and for different values of oblateness parameters $A_1 (0 < A_1 < 1)$ and $A_2 (0 < A_2 < 1)$.

Finally, we have determined the ZVCs to study the possible regions of motion in which the spacecraft is free to move. We have observed that the regions of motion increase in which the spacecraft can freely move from one place to other place. Further, it has been observed that the unreachable regions can become reachable in the presence of continuous low-thrust. This paper is applicable in the Earth-Moon system for communications for the spacecraft missions.

Conflicts of Interest

The authors declare no conflicts of interest regarding the publication of this paper.

References

[1] Szebehely, V. (1967) Theory of Orbits. The Restricted Problem of Three-Bodies. Academic Press, New York.

[2] Subbarao, P.V. and Sharma, R.K. (1975) A Note on the Stability of the Triangular Points of Equilibrium in the Restricted Three-Body Problem. *Astronomy & Astrophysics*, **43**, 381-383.

[3] Bhatnagar, K.B. and Chawla, J.M. (1977) The Effect of Oblateness of the Bigger Primary on Collinear Equilibrium Points in the Restricted Problem of Three Bodies. *Celestial Mechanics and Dynamical Astronomy*, **16**, 129-136. https://doi.org/10.1007/BF01228595

[4] Tsirogiannis, G.A., Douskos, C.N. and Perdios, E.A. (2006) Computation of the Lyapunov Orbits in the Photogravitational Restricted Three-Body Problem with Oblateness. *Research in Astronomy and Astrophysics*, **305**, 389-398.

[5] Mittal, A., Ahmad, I. and Bhatnagar, K.B. (2009) Periodic Orbits in the Photogravitational Restricted Problem with the Smaller Primary an Oblate Body. *Astrophysics and Space Science*, **323**, 65-73. https://doi.org/10.1007/s10509-009-0038-2

[6] Singh, J. (2011) Combined Effects of Perturbations, Radiation, and Oblateness on the Nonlinear Stability of Triangular Points in the Restricted Three-Body Problem. *Astrophysics and Space Science*, **332**, 331-339. https://doi.org/10.1007/s10509-010-0546-0

[7] Beevi, A.S. and Sharma, R.K. (2012) Oblateness Effect of Saturn on Periodic Orbits in the Saturn-Titan Restricted Three-Body Problem. *Astrophysics and Space Science*, **340**, 245-261.

[8] Abouelmagd, E.I. (2013) The Effect of Photogravitational Force and Oblateness in the Perturbed Restricted Three-Body Problem. *Astrophysics and Space Science*, **346**, 51-69. https://doi.org/10.1007/s10509-013-1439-9

[9] Jain, M. and Aggarwal, R. (2015) A Study of Non-Collinear Equilibrium Points in Restricted Three-Body Problem with Stokes Drag Effect When Smaller Primary Is

an Oblate Spheroid. *Astrophysics and Space Science*, **358**.

[10] Zotos, E.E. (2016) Fractal Basins of Attraction in the Planar Circular Restricted Three-Body Problem with Oblateness and Radiation Pressure. *Astrophysics and Space Science*, **361**. https://doi.org/10.1007/s10509-016-2769-1

[11] Srivastava, V.K., Kumar, J. and Kushvah, B.S. (2017) Regularization of Circular Restricted Three-Body Problem Accounting Radiation Pressure and Oblateness. *Astrophysics and Space Science*, **362**. https://doi.org/10.1007/s10509-017-3021-3

[12] Farquhar, R.W. (1967) Lunar Communications with Libration-Point Satellites. *Spacecraft and Rockets*, **4**, 1383-1384. https://doi.org/10.2514/3.29095

[13] Dusek, H.M. (1966) Motion in the Vicinity of Equilibrium Points of a Generalized Restricted Three-Body Model. *Prog. Astronaut. Rocket*, **17**, 37-54. https://doi.org/10.1016/B978-1-4832-2729-0.50009-0

[14] McInnes, C.R., McDonald, A.J.C., Simmons, J.F.L. and MacDonald, E.W. (2004) Solar-Sail Parking in Restricted Three-Body Systems. *Journal of Guidance, Control, and Dynamics*, **17**, 399-406. https://doi.org/10.2514/3.21211

[15] Broschart, S.B. and Scheeres, D.J. (2005) Control of Hovering Spacecraft near Small Bodies: Application to Asteroid 25143 Itokwa. *Journal of Guidance, Control, and Dynamics*, **28**, 343-354. https://doi.org/10.2514/1.3890

[16] Morimoto, M.Y., Yamakawa, H. and Uesugi, K. (2007) Artificial Equilibrium Points in the Low-Thrust Restricted Three-Body Problem. *Journal of Guidance, Control, and Dynamics*, **30**, 1563-1567. https://doi.org/10.2514/1.26771

[17] Baig, S. and McInnes, C.R. (2008) Artificial Three-Body Equilibria for Hybrid Low-Thrust Propulsion. *Journal of Guidance, Control and Dynamics*, **31**, 1644-1655. https://doi.org/10.2514/1.36125

[18] Bombardelli, C. and Pelaez, J. (2011) On the Stability of Artificial Equilibrium Points in the Circular Restricted Three-Body Problem. *Celestial Mechanics and Dynamical Astronomy*, **109**, 13-26. https://doi.org/10.1007/s10569-010-9317-z

[19] Aliasi, G., Mengali, G. and Quarta, A. (2011) Artificial Equilibrium Points for a Generalized Sail in the Circular Restricted Three-Body Problem. *Celestial Mechanics and Dynamical Astronomy*, **110**, 343-368. https://doi.org/10.1007/s10569-011-9366-y

[20] Aliasi, G., Mengali, G. and Quarta, A. (2012) Artificial Equilibrium Points for a Generalized Sail in the Elliptic Restricted Three-Body Problem. *Celestial Mechanics and Dynamical Astronomy*, **114**, 181-200. https://doi.org/10.1007/s10569-012-9425-z

[21] Ranjana, K. and Kumar, V. (2013) On the Artificial Equilibrium Points in a Generalized Restricted Problem of Three-Bodies. *International Journal of Astronomy and Astrophysics*, **3**, 508-516. https://doi.org/10.4236/ijaa.2013.34059

[22] Yang, H.W., Zeng, X.Y. and Baoyin, H. (2015) Feasible Region and Stability Analysis for Hovering around Elongated Asteroids with Low-Thrust. *Research in Astronomy and Astrophysics*, **15**, 1571-1585. https://doi.org/10.1088/1674-4527/15/9/013

[23] Lei, H.L. and Xu, B. (2017) Invariant Manifolds around Artificial Equilibrium Points for Low-Thrust Propulsion Spacecraft. *Astrophysics and Space Science*, **362**, 75. https://doi.org/10.1007/s10509-017-3053-8

[24] Bu, S., Li, S. and Yang, H. (2017) Artificial Equilibrium Points in Binary Asteroid Systems with Continuous Low-Thrust. *Astrophysics and Space Science*, **362**, 8.

[25] McCusky, S.W. (1963) Introduction to Celestial Mechanics. Addision-Wesley Publishing Company, New York.

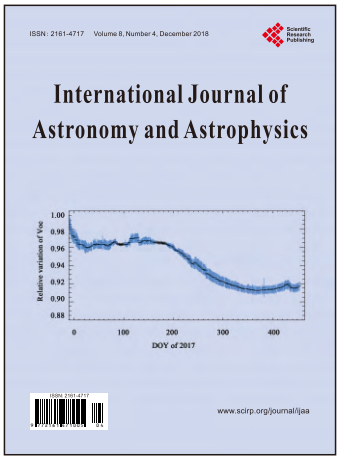

Call for Papers

International Journal of Astronomy and Astrophysics (IJAA)

ISSN 2161-4717 (Print) ISSN 2161-4725 (Online)
http://www.scirp.org/journal/ijaa

International Journal of Astronomy and Astrophysics **(IJAA)** is an international scientific journal dedicated to the publication and public discussion of high quality original research in all the fields of astrophysics and space sciences and related technology. All the manuscripts must be prepared in English, and are subject to a rigorous and fair peer-review process. Accepted papers will immediately appear online followed by printed hard copies.

Editor-in-Chief

Prof. Michael D. Smith University of Kent, UK

Editorial Board

Subject Coverage

The journal publishes original papers including but not limited to the following fields:

- Astrogeodynamics
- Astrophysics
- Cosmic Rays and Gamma Astronomy
- Dynamics of Celestial Bodies in the Solar System and Artificial Bodies
- Extrasolar Planets
- Formation and Evolution of Galaxies and Their Clusters
- Formation and Evolution of Stars
- Heliospheric Physics
- High-Energy and Cataclysmic Processes in Astrophysics
- Interstellar Matter
- Interstellar Medium: Star Formation Regions
- Kinematics and Structure of the Galaxy
- Large-Scale Structure of Universe Formation and Evolution of Galaxies
- Last Stages of Stellar Evolution and Chemical Evolution of the Galaxy
- Magnetospheric Physics
- Microquasars and High-Energy Astrophysics
- Neutron Astronomy
- New Astronomical Techniques and Methods
- Planets, Comets, Asteroids and Dust
- Pulsar Magnetospheres
- Solar and Stellar Physics
- Solar Magnetic Activity and Heliogeospace Environments
- Solar/Interstellar Terrestrial Relations
- Solar-Terrestrial Physics and Space Weather
- Space Observation and Exploration
- Supernovae and Evolution of the Universe

We are also interested in short papers (letters) that clearly address a specific problem, and short survey or position papers that sketch the results or problems on a specific topic. Authors of selected short papers would be invited to write a regular paper on the same topic for future issues of the IJAA.

Notes for Intending Authors

Submitted papers should not have been previously published nor be currently under consideration for publication elsewhere. Paper submission will be handled electronically through the website. All papers are refereed through a peer review process. For more details about the submissions, please access the website.

http://www.scirp.org/journal/ijaa E-mail: ijaa@scirp.org

What is SCIRP?

Scientific Research Publishing (SCIRP) is one of the largest Open Access journal publishers. It is currently publishing more than 200 open access, online, peer-reviewed journals covering a wide range of academic disciplines. SCIRP serves the worldwide academic communities and contributes to the progress and application of science with its publication.

What is Open Access?

All original research papers published by SCIRP are made freely and permanently accessible online immediately upon publication. To be able to provide open access journals, SCIRP defrays operation costs from authors and subscription charges only for its printed version. Open access publishing allows an immediate, worldwide, barrier-free, open access to the full text of research papers, which is in the best interests of the scientific community.

- High visibility for maximum global exposure with open access publishing model
- Rigorous peer review of research papers
- Prompt faster publication with less cost
- Guaranteed targeted, multidisciplinary audience

Scientific Research Publishing

Website: http://www.scirp.org

Subscription: sub@scirp.org

Advertisement: service@scirp.org